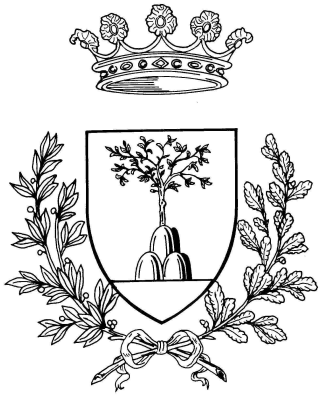

Università degli Studi di Ferrara

Facoltà di Scienze Matematiche, Fisiche e Naturali
Corso di Dottorato in Fisica

Radiative Transfer Problem in the Presence of Strong Magnetic Fields.

Analytical and Numerical Treatment.

Tutor
Prof. Lev Titarchuk

Dottorando
Chiara Ceccobello

Co-tutor
Dott. Ruben Farinelli

Ciclo XXIV

Università degli Studi di Ferrara

Facoltà di Scienze Matematiche, Fisiche e Naturali
Corso di Dottorato in Fisica

Radiative Transfer Problem in the Presence of Strong Magnetic Fields.

Analytical and Numerical Treatment.

Tutor
Prof. Lev Titarchuk

Dottorando
Chiara Ceccobello

Co-tutor
Dott. Ruben Farinelli

Ciclo XXIV

To Caterina

Contents

List of Figures

List of Tables

Abstract

In this thesis we investigate analytical and numerical methods to find a solution of the radiative transfer equation in the presence of strong magnetic fields.
My Ph.D research theme is focused on those astrophysical objects which presumably show an evidence of a strong magnetic field ($B \gtrsim 10^{12}$ G), with a particular emphasis on the physics of X-ray spectral formation in these objects.
The radiative transfer equation which describes spectral formation is, in general, rather complicated because of its integro-differential nature.
If we are interested in finding a solution, even numerically, we need to simplify the problem.
For instance, we assume that stellar atmospheres can be represented, in first approximation, by a plane-parallel slab of fully ionized plasma of non-relativistic thermal electrons with an external uniform magnetic field. Since we are interested in modelling the high energy photon emission coming from the interaction with such medium, we assume also that the dominant radiative process which modifies the X-ray photon spectrum is multiple inverse Compton scattering. We propose two approaches to the study of this problem and we discuss the related solutions.
In the first part of this thesis, we present an analytical and numerical study of the radiative transfer problem in the presence of a strong uniform magnetic field ($B \gtrsim 4.4 \times 10^{13}$G) taking place in a medium filled by non-relativistic thermal electrons in plane-parallel geometry.
Even after making some initial assumptions, the equation governing such system is still an integro-differential equation. Additional conditions are required to handle the radiative transfer equation the with separation of variable method. Then the radiative transfer problem can be reduced to the solution of the equation which has a diffusion operator for the energy variable and an integral operator for the space variable.
Such an integro-differential equation was firstly derived and its solution was estimated in 1988 by Lyubarskii in [8],[9]. We have solved numerically the equation proposed by Lyubarskii and we have confirmed this solution using the analytical methods.
The second part of the thesis is devoted to the description of a numerical algorithm that we implemented for the resolution of radiative transfer equation,

when it reduces to a pure differential form. This is usually the case when the Fokker-Planck (diffusion) approximation is applicable.
The algorithm is essentially based on relaxation methods and, generally, it solves all inhomogeneous second order elliptic partial differential equations with vanishing mixed derivatives. The numerical code gives a stable solution of the equation when the system has reached its steady-state equilibrium.
We test the code solving the radiative transfer problem in the case of cylindrical accretion onto a magnetised neutron star, when a combined effect of bulk and thermal Comptonization takes place.
Finally, we implemented the algorithm in the X-ray spectral fitting package XSPEC and we successfully fitted the X-ray spectra of the two Supergiant Fast X-ray Transients (SFXTs) XTE J1739-302 and IGR J17544-2619, observed with the *Swift* Gamma-ray Burst Telescope. Our model is then compared with other XSPEC models we used during the X-ray spectral fitting procedure and we briefly discuss possible implications on the geometry of these systems. I critically discuss and compare the results presented in the thesis in the conclusion section.

Abstract

Con la presente tesi di Dottorato vorrei presentare il lavoro partito durante la mia tesi specialistica e sviluppatosi nel corso dei tre anni successivi. Il campo su cui la mia ricerca è stata incentrata è lo studio analitico e numerico del problema del trasporto radiativo in presenza di campi magnetici esterni forti ($B \gtrsim 10^{12}$G) nell'ambito dell'Astrofisica delle Alte Energie.
In particolare, campi magnetici così forti sono stati associati ad alcune sottoclassi di stelle di neutroni, dalle pulsar X ($B \sim 10^{12}$ G) alle cosiddette magnetar ($B \gtrsim 10^{14}$ G).
In generale, l'equazione del trasporto radiativo che descrive le atmosfere stellari è molto complicata da risolvere. La causa di questa complicazione intriseca è che tale equazione si presenta in forma integro-differenziale. Trovare una soluzione, seppure numerica, risulta essere nella maggioranza dei casi impossibile senza introdurre delle semplificazioni.
Nel nostro caso specifico, assumiamo di poter approssimare l'atmosfera di una stella di neutroni magnetizzata come uno strato di plasma completamente ionizzato, composto di elettroni termici non relativistici, immerso in un forte campo magnetico uniforme. Inoltre assumiamo che l'unico processo dominante sia lo scattering Compton inverso multiplo (Comptonizzazione).
In questa tesi discuterò due tipi di approccio che abbiamo scelto per risolvere il suddetto problema e mostreremo i risultati ottenuti in dettaglio.
La prima tipologia di approccio consiste in uno studio prima analitico e successivamente numerico dell'equazione del trasporto radiativo per uno strato di elettroni termici e non relativistici in campi magnetici forti ($B \gtrsim 4.4 \times 10^{13}$G). Pur avendo già introdotto delle semplificazioni per quanto riguarda la definizione del sistema fisico che andremo a trattare, l'equazione rimane ancora integro-differenziale. Tuttavia, tramite ulteriori ragionevoli assunzioni che spiegheremo in dettaglio nel corso della tesi, riusciamo a risolvere tale equazione tramite il metodo della separazione delle variabili. A questo punto, infatti, otteniamo un sistema composto da un'equazione puramente differenziale per la variabile indipendente energia e un'equazione puramente integrale per la variabile spaziale. Questo approccio si deve intendere come un approfondimento ed una estensione di quello proposto nel 1988 da Lyubarskii in [8],[9].
La seconda parte di questa tesi è stata dedicata alla descrizione dell'algoritmo nu-

merico che abbiamo implementato allo scopo di ottenere soluzioni di equazioni del trasporto radiativo, quando queste possono essere ridotte a equazioni puramente differenziali. Questo è tipicamente il caso in cui l'approssimazione di diffusione, più propriamente detta approssimazione di Fokker-Planck, é applicabile.
L'algoritmo è basato sui cosiddetti "relaxation methods", ovvero trattando alle differenze finite le derivate, si lascia dunque evolvere una configurazione iniziale data nella soluzione finale reale dell'equazione iniziale. Il codice, in generale, può risolvere equazioni alle derivate parziali ellittiche del secondo ordine non omogenee con derivate miste nulle.
Abbiamo testato il nostro codice sull'equazione del trasporto in caso accrescimento cilindrico su una stella di neutroni magnetizzata ($B \sim 10^{12}$ G), quando siano presenti sia Comptonizzazione termica che dinamica dovuta ad un moto di bulk non trascurabile degli elettroni del plasma. Il modello è stato implementato nella piattaforma per l'analisi spettrale XSPEC e presto sarà reso pubblico per la comunità scientifica. Gli spettri che otteniamo dal nostro modello teorico li abbiamo quindi utilizzati per fittare i dati del telescopio *Swift* dei prototipi di Supergiant Fast X-ray Transients (SFXTs) XTE J1739-302 e IGR J17544-2619 e lo abbiamo confrontato con altri modelli utilizzati per questo tipo di analisi.
In conclusione verranno discussi i due approcci e i risultati relativi ad entrambi.

1

Introduction

The phenomena of energy transfer by radiation in media, which can absorb, emit and scatter radiation, is considered a very important subject since, at least, a hundred years. This interest started with the first study of the solar radiation absorption by the cloudless terrestrial atmosphere, but suddenly it became fundamental in many complicated phenomena involving a wide range of physical fields, from the astrophysical problems to nuclear explosion, from rocket engines to plasma generators designed for nuclear fusion. In particular, for astrophysicists the radiative transfer theory is strongly related to the studies of the internal structures of the stars and their atmospheres [1].

Most of the information we have about astrophysical objects are those coming from the radiation emitted into space. Understanding the radiation characteristics of the stellar atmosphere seems to be a crucial issue to be solved in order to comprehend the actual nature of the stars.

Defining uniquely the theory of stellar atmosphere is already a problem, because we have not a clear definition of crucial concepts like, for instance, stellar radius and surface temperature. In fact, typically, we can identify two research topics: stars' interior and stellar atmosphere, with practically no clue about the transition region [5].

I concentrate my efforts on the radiative transfer problem in the context of stellar atmosphere. Indeed, we will discuss in details two different and simplified approaches to the equation of radiative transfer (RTE) for radiation travelling through a magnetised medium.

In this Chapter, we introduce the basics of radiative transfer and we define some fundamental quantities that will be useful for the rest of the thesis. In Chap. 2 and 3, we deal with radiative transfer problem for a plane-parallel slab of non-relativistic thermal electrons in a strong magnetic field. We solve analytically and numerically the integro-differential equation describing the system. In Chap. 4, 5 and 6, we describe a numerical algorithm (COMPMAG) that solves the differential ('diffusion-like') equation for Compton scattering in a magnetised accretion

column, obtained through the inclusion of an escape term, that takes into account the photon diffusion through the walls of the column. In Chap. 7 we report the spectral fitting of the SFXTs XTE J1739-302 and IGR J17544-2619 with several models including COMPMAG . Concluding, we discuss our results and compare the two approaches.

1.1 Introduction to the Radiative Transfer

Generally speaking, solving the complete radiative transfer problem is strongly troublesome. Indeed, several physical simplifications are needed in order to study 'realistic' systems, which are

- ♢ The use of geometric optics approximation. It is assumed that the scale of variation of the macroscopic system's parameter greatly exceed the electromagnetic radiation wavelength. Under this assumption the radiation travels along straight lines in the medium.
- ♢ The medium is assumed to be rarefied, which means that the particles do not shade each other and there is no mutual interference between them. Hence the total effect of electromagnetic interactions with a group of particles is the summation over all the interactions on each particle.
- ♢ All the diffraction effects at the electromagnetic field interaction with an individual particle should be taken into account.
- ♢ The processes which can take place within a volume of medium are absorption, emission and scattering.

Before presenting the proper RTE derived under the assumptions we made above, we should define some general quantities. In particular, we need to specify what is our unknown dependent function.
Let us start considering that we are looking at radiation as made of straight lines. Thus, we can define the concept of *energy flux*: the amount of energy that passes through an element of area dA for a time dt should be $F\,dA\,dt$, where F is the energy flux and, in general, it depend on the orientation of the element dA. Thus the flux is measured in erg s^{-1} cm^{-2}.
In order to give a more detailed description of the phenomenon, instead of considering the amount of energy carried by all the rays, let us focus our attention on the fraction of energy carried by a "single" ray. Of course, a single ray should be defined as the ensemble of rays that are infinitesimally closer (within a solid angle $d\Omega$) to the given ray, because individually they carry no energy. Therefore we can write the energy crossing the element of area dA in time dt and in frequency $d\nu$ as

$$dE = I_\nu\, dA\, dt\, d\Omega\, d\nu, \tag{1.1}$$

where I_ν is the *specific intensity*, that is given in erg s^{-1} cm^{-2} $ster^{-1}$ Hz^{-1}[3]. The specific intensity is the unknown function in RTE and it depends upon

space, direction, frequency and time (seven independent variables). If the specific intensity is independent of direction at a certain point, it is said to be *isotropic* at that point. If I_ν is independent both of space and direction, the radiation field is *homogeneous* and *isotropic*. In this case the radiation and the matter are in complete thermodynamic equilibrium at temperature T and the specific intensity is given by the Planck function $b \equiv B(\nu, T)$

$$I = B = \frac{2h\nu^3}{c^2} \frac{1}{e^{h\nu/kT} - 1}, \tag{1.2}$$

where h is the Planck constant, c is the speed of light and k is the Boltzmann constant [72]. The specific intensity can be related to the photon occupation number. Let $f_\alpha(\mathbf{x}, \mathbf{p}, t)$ be the photon distribution function and $f_\alpha(\mathbf{x}, \mathbf{p}, t) d^3x\, d^3p$ be the number of photons of spin state α at time t, located in the phase space volume $d^3x\, d^3p$. The amount of energy possessed by these photons is

$$dE = \sum_{\alpha=1}^{2} h\nu\, f_\alpha(\mathbf{x}, \mathbf{p}, t)\, d^3x\, d^3p. \tag{1.3}$$

Recalling that the vector momentum of a photon satisfies $\mathbf{p} = (h\nu/c)\,\hat{\mathbf{k}}$ with $\hat{\mathbf{k}}$ being the unit vector in the direction of propagation of photons and considering that the space volume occupied by photons travelling along $\hat{\mathbf{k}}$ through the area dA with normal $\hat{\mathbf{n}}$ is $d^3x = c(\hat{\mathbf{k}} \cdot \hat{\mathbf{n}})\, dt\, dA$ and the corresponding element of momentum volume is $d^3p = (h^3\nu^2/c^3)\, d\Omega\, d\nu$, comparing (1.1) and (1.3), we have

$$I_\nu(\mathbf{\Omega}, \mathbf{r}, t) = \sum_{\alpha=1}^{2} \left(\frac{h^4\nu^3}{c^2} \right) f_\alpha(\mathbf{x}, \mathbf{p}, t). \tag{1.4}$$

Since h^3 is the fundamental unit of phase space volume, we define the occupation number $n_\alpha \equiv h^3 f_\alpha$ for each spin state $\alpha = 1, 2$. Thus, the specific intensity can be written as a function of the photon occupation number as follows

$$I_\nu(\mathbf{\Omega}, \mathbf{r}, t) = \sum_{\alpha=1}^{2} \left(\frac{h\nu^3}{c^2} \right) n_\alpha(\mathbf{x}, \mathbf{p}, t). \tag{1.5}$$

In the following Chapters of this thesis, we will treat the specific intensity as a classical quantity, hence we drop the spin index α [69].

1.2 Equation of Radiative Transfer in a Nutshell

The radiation may, in principle, propagate both in free space and through matter and RTE represents the energy conservation law for the radiation field. For instance, if the ray of light is travelling through free space (no interactions), we expect that the variation of specific intensity along the ray is zero.
However, if the ray passes across a medium, it can interact with it and the

energy may change due to emission, absorption or scattering processes, leading to a non-zero variation of the specific intensity. A complete derivation of the RTE in Cartesian, polar and spherical coordinates can be found in a plethora of fundamental books, such as Pomraning [4], Rybicki & Lightman [3], Shapiro & Teukolsky [71], Mihalas [6], Peraiah [73]. Here, we would give the basic ideas behind the formal derivation.
When the radiation travels across a medium we can write a qualitatively equation of transport of the kind

$$\frac{\partial I_\nu}{\partial t} + c\,\hat{\mathbf{k}}\cdot\nabla I_\nu = sources - sinks, \tag{1.6}$$

which tells us that the variation in time and space of the specific intensity along the direction of propagation $\hat{\mathbf{k}}$ is equal to the difference between the amount of intensity gained by processes acting like *sources* (emission and scattering into the direction $\hat{\mathbf{k}}$) and the intensity lost due to processes playing like *sinks* (absorption and scattering off the direction $\hat{\mathbf{k}}$) [69]. The right hand side of equation (1.6) should be characterised by several terms accounting for all the processes that may happen throughout the medium. The classical general form of the RTE is written per unit length and reads as

$$\frac{1}{c}\frac{\partial I_\nu}{\partial t} + \hat{k}\cdot\nabla I_\nu = \frac{1}{4\pi}\varrho j_\nu - \varrho k_\nu^{\rm abs} I_\nu - \varrho k_\nu^{\rm sc} I_\nu + \varrho k_\nu^{\rm sc}\mathbf{\Phi}_\nu(\hat{\mathbf{k}},\mathbf{x}), \tag{1.7}$$

where we have defined

$$\mathbf{\Phi}_\nu(\hat{\mathbf{k}},\mathbf{x}) \equiv \oint \Phi_\nu(\hat{\mathbf{k}},\hat{\mathbf{k}}')I_\nu(\hat{\mathbf{k}}')d\Omega', \tag{1.8}$$

which is the intensity weighted by the scattering probability density.
Note that, for instance, for isotropic scattering $\Phi_\nu = 1/4\pi$ and, thus, $\mathbf{\Phi}_\nu = J_\nu$ which is the *mean specific intensity*.
The other quantities we have introduced are: ϱ is the mass density per unit volume of the gas, j_ν is its emissivity per unit mass, $k_\nu^{\rm abs}$ is its total absorption opacity (i.e. the total absorption cross-section per unit mass), $k_\nu^{\rm sc}$ is its total scattering opacity and $\Phi_\nu(\hat{k},\hat{k}')$ is the scattering probability density (from $\hat{\mathbf{k}}'$ to $\hat{\mathbf{k}}$).
Looking at the right hand side of equation (1.7), we can identify the physical processes involved in the problem:

(i) *emission*: ϱj_ν represents the source term for radiation that comes from true emission, where the $1/4\pi$-factor accounts for the solid angle;

(ii) *absorption*: $\varrho k_\nu^{\rm abs} I_\nu$ accounts for the amount of light removed from the beam per unit length of photon travel due to true absorption;

(iii) *scattering out* $\hat{\mathbf{k}}$*-direction*: $\varrho k_\nu^{\rm sc} I_\nu$ is the quantity of radiation scattered out the direction of the beam along $\hat{\mathbf{k}}'$;

(iv) *scattering toward* $\hat{\mathbf{k}}$*-direction*: $\varrho k_\nu^{\rm sc}\mathbf{\Phi}_\nu(\hat{\mathbf{k}},\mathbf{x})$ is the integral contribution given by all the radiation scattered into the beam from any other line of sight.

It is worth noticing that the emission coefficient has two components, namely $j_\nu = j_\nu^{spont} + j_\nu^{stim}$. While the spontaneous emission is, in almost all the cases, isotropic in the local rest frame of the medium, the stimulated emission are coherent with the absorbed radiation. Indeed, if the system is close to thermodynamic equilibrium the coefficient for stimulated emission can be written as $j_\nu^{stim} = k_\nu^{\mathrm{abs}} I_\nu e^{-h\nu/kT}$, so it plays the role of a negative absorption term. Therefore it is convenient to replace j_ν and k_ν^{abs} with

$$j'_\nu = j_\nu - j_\nu^{stim}, \tag{1.9}$$

$$k'_\nu = k_\nu^{\mathrm{abs}} \left[1 - e^{-h\nu/kT}\right], \tag{1.10}$$

where both these coefficients are isotropic [7]. Thus equation (1.7) reads as

$$\frac{1}{c}\frac{\partial I_\nu}{\partial t} + \hat{k} \cdot \nabla I_\nu = \frac{1}{4\pi} \varrho j'_\nu - \varrho k'_\nu I_\nu - \varrho k_\nu^{\mathrm{sc}} I_\nu + \varrho k_\nu^{\mathrm{sc}} \mathbf{\Phi}_\nu(\hat{\mathbf{k}}, \mathbf{x}). \tag{1.11}$$

Nevertheless in writing (1.11) we still neglect important physical aspects. In particular, we should consider the quantum statistics obeyed by photons. Photons follow Bose-Einstein statistics, therefore the processes of emission and scattering are increased depending on the number of photons which are in the final state of the interaction. This sort of processes are called *induced processes*. Hence, if P is the probability of an emission or a scattering process, then, including also induced processes, the actual probability P' is $P' = P(1 + n)$, where n is the number of photons in the final state of the transition. Considering equation (1.5), such probability becomes

$$P' = P\left(1 + \frac{I_\nu c^2}{2h\nu^3}\right). \tag{1.12}$$

The probability P' can be included in equation (1.11) as multiplicative factor for the emission and scattering terms. Accounting for induced processes into RTE provides a great hindrance for the resolution of the problem, since it involves handling non-linear terms (quadratic in the specific intensity). The neglect of this terms leads to the Wien, rather than the Planck function as the equilibrium distribution for the specific intensity. For almost all the astrophysical application, the induced processes are negligible in the RTE.

A further central assumption that holds in the majority of the studied cases in RTE of stellar atmospheres is the so-called condition of *Local Thermodynamic Equilibrium* (LTE). Such condition states that the properties of the medium are dominated by atomic collisions which maintain thermodynamical equilibrium locally, while the radiation field even if it deviates significantly from the equilibrium Planck distribution, does not affect this equilibrium. Therefore, we assume that the particles of the medium have the equilibrium Maxwell-Boltzmann distribution and photons, having a shorter mean free-path, can escape experiencing a departure from their equilibrium distribution which is the Planck distribution without implying the breaking of LTE.

Both the above assumptions make easier the estimates of the absorption, emission and scattering coefficients of RTE.

However, since the specific intensity depends upon seven independent variables $(\mathbf{r}, \nu, \mathbf{\Omega}, t)$, solving it analytically, even in the most simple geometric configuration (plane geometry) in which the number of independent variables reduces to two (z and μ), can be possible only in a few number of limiting cases. The characteristic that makes the RTE so complicated is that is an integro-differential equation. The most popular approach is to analytically approximate the frequency and angle dependences of the specific intensity which are responsible for giving rise to the integral terms.
In the first part of this thesis, we will discuss the easier formulation of RTE in slab geometry in the presence of strong magnetic fields. In this case analytical results may be obtained [8],[9]. We present a semi-numerical treatment of RTE compared with the analytical approach. The second part is dedicated to a fully numerical approach to a differential RTE in Fokker-Plank approximation for an accretion column geometry in strong magnetic fields.

2

Radiative Transfer Problem in Strong Magnetic Fields

Although there are several radiative processes that are involved in the study of the phenomenon of radiation travelling through a medium, nonetheless we are interested in modelling the physical situations where Compton scattering is the dominant process.
In particular, we tackle the problem of Comptonization in strong magnetic fields. The study of the scattering process of photons by electrons in strong magnetic fields has begun a very hot topic since radio pulsars were discovered by Hewish and Bell (1967) and cyclotron lines in X-ray pulsars [26] were detected. In fact, from their observations we have the first evidences of magnetic fields of order of 10^{12} G. Moreover indirect estimates seem to confirm in the last years that there exist astrophysical objects with a magnetic field even larger ($B \gtrsim 10^{14-15}$ G). This class of objects, called "magnetars", is divided into two sub-classes, namely Anomalous X–ray Pulsars (AXPs) and Soft Gamma Repeaters (SGRs) [27]. The physics of radiative transfer in presence of a strong magnetic field is rather complicated [71], and analytical or numerical solutions of the problem can be found only under unavoidable simplified assumptions. Here, we consider the case of a plane-parallel slab of thermal electrons having Thomson optical depth τ_0 and uniform temperature kT_e, dipped into an strong magnetic field, oriented along the normal of the plane. Our work can be considered an extension and essential improvement of the analytical solutions found by Lyubarskii ([8] and [9], hereafter L88) for this particular geometrical configuration.
In this Chapter we provide the fundamentals of standard Compton scattering (zero external field), then we describe our approach to the strong magnetic field case.

2.1 Standard Compton Scattering

Compton scattering is an *incoherent* or *inelastic* scattering between an hot photon of energy $E = h\nu$ and an electron, which is considered at rest. The collision causes the electron to recoil and a new photon with energy $E_1 = h\nu_1$ is created at angle θ respect to the incoming direction of the initial photon. The relation between the initial and final energy is provided by the kinematics of the process and it is

$$E_1 = \frac{E}{1 + \frac{E}{m_e c^2}(1 - \cos\theta)}, \tag{2.1}$$

or, equivalently

$$\lambda_1 - \lambda = \lambda_c(1 - \cos\theta), \tag{2.2}$$

where we have defined $\lambda_c \equiv h/(m_e c) = 0.02426\mathring{A}$ as the *Compton wavelength* for the electron.
For photon energy $h\nu \ll m_e c^2$, basically there is no photon energy exchange in the rest frame of the electron (ERF) and the scattering can be considered still elastic. In this range of energies, the differential cross section of the interaction is the *Thomson* differential cross section for unpolarised photons

$$\frac{d\sigma_{\rm T}}{d\Omega} = \frac{1}{2} r_0^2 (1 + \cos^2\theta), \tag{2.3}$$

where $r_0 = e^2/(m_e c^2) \cong 2.8 \times 10^{-13}$ cm is the classical electron radius.
At energies $h\nu \gtrsim m_e c^2$, quantum corrections become important and (2.3) is replaced by the *Klein-Nishina* differential cross section [22]

$$\frac{d\sigma}{d\Omega} = \frac{r_0^2}{2}\frac{E_1^2}{E^2}\left[\frac{E}{E_1} + \frac{E_1}{E} - \sin\theta^2\right]. \tag{2.4}$$

In the limit of small photon energy exchange $E_1 \sim E$, it can be easily seen that the formula (2.4) reduces to (2.3). Besides it is worth noticing that for increasing photon energies, the cross section (2.4) considerably decreases.
However, we will concentrate for the rest of this thesis on the non-relativistic regime ($h\nu \ll m_e c^2$) and also on the situation in which the electron has a sufficiently large amount of energy respect to the photon. Thus, the energy is transferred from electrons to photons. This process is called *inverse Compton*.
In particular, not to digress to much from the aim of the thesis, we are interested in the case of multiple inverse Compton scatterings in slab of medium filled by thermal electrons. In this physical framework, we should define a parameter that describes how significantly will be changed the photon energy after passing through the medium. This quantity is the so-called *Compton y parameter*. In the non-relativistic regime, one can demonstrate that the Compton parameter is

$$y_{NR} = 4\frac{kT}{m_e c^2} N_{\rm sc}, \tag{2.5}$$

where $4kT/(m_e c^2)$ is the average fractional energy exchange per scattering and $N_{\rm sc}$ is the mean number of scatterings. If $y \gtrsim 1$ both the total photon energy

and the spectrum will appears significantly different from the initial configuration, instead for $y \ll 1$ they will remain closer to their initial value and shape.
The equation which describes the emerging spectrum evolution of the radiation due to multiple inverse Compton scatterings is the *Boltzmann* equation for the photon phase space density $n(\nu)$

$$\frac{1}{c}\frac{\partial n}{\partial t}(\nu) = \int d^3p \int \frac{d\sigma}{d\Omega} \left[f_e(\mathbf{p_1}) n(\nu_1)(1+n(\nu)) - f_e(\mathbf{p}) n(\nu)(1+n(\nu_1)) \right] d\Omega, \tag{2.6}$$

where f_e is the electron phase space, that for a thermal plasma of non-relativistic electrons is $f_e(E) = n_e (2\pi m_e kT)^{-3/2} e^{-E/kT}$. The terms $1+n$ take into account stimulated processes. Here $n(\nu)$ is assumed to be isotropic.
The Boltzmann equation is rather complicated to be solved without making some assumptions and, for instance, in the relativistic regime, since the amount of energy exchanged $\Delta \equiv (h\nu_1 - h\nu)/kT$ per scattering is large, the integro-differential form of equation (2.6) cannot be simplified. This unfortunately happens in most of the cases. However, in the non-relativistic regime and for small exchanged energy, equation (2.6) can be expanded up to the second order in the small quantity Δ, leading to a pure differential equation, called *Kompaneets* equation [51], which is

$$\frac{\partial n}{\partial t_c} = \frac{kT}{m_e c^2} \frac{1}{x^2} \frac{\partial}{\partial x} \left[x^2 (n' + n + n^2) \right], \tag{2.7}$$

where $x \equiv h\nu/kT$ is the dimensionless energy and $t_c = n_e \sigma_{\mathrm{T}} c\, t$ is the dimensionless time measured in units of mean time between each collision of photons off electrons.
The aim of this thesis is that to propose two different approaches to the multiple inverse Compton problem in a thermal strongly magnetised medium. The introduction of an external strong magnetic field has several effects and, of course, it constitutes a further complication of the problem. Not least, the fact that it introduces a strong anisotropy which makes impossible to use the Fokker-Planck (diffusion) approximation without making any assumption. We propose two alternative treatments to the problem of Comptonization in strong magnetic fields. In particular, in this Chapter and Chap. 3, we present a solution of a simplified version of (2.6) for a plane-parallel medium in the presence of strong magnetic field, which maintains its integro-differential nature.

2.2 Compton Scattering in Strong Magnetic Fields

The radiative processes that occurs in a magnetised plasma are several and the kind of approach that we need to deal with them it is different depending on the magnetic field strength. For instance, at relatively low magnetic fields $B \lesssim B_c$ processes like cyclotron absorption and emission or Compton scattering are dominant. When the magnetic field is largely overcritical other processes will occur, such as one-photon pair production and annihilation, photon splitting and bound pair creation [23].

A complete treatment of all the radiative processes that happens in a strong magnetised plasma would require a whole book, or, better, many books, itself. Therefore, since we are interested in modelling the spectrum in the non-relativistic regime and for photon energy well below E_c, the multiple inverse Compton scattering is the dominant process [21].
The presence of a strong magnetic field entails significant deviation from the canonical Thomson scattering theory [14], [15]. Moreover, relativistic effects become important when the external magnetic field reaches the critical value $B_{\rm c} = 4.413 \times 10^{13}$ G so that $h\nu_g \approx m_e c^2$, where ν_g is the cyclotron frequency which is given by the relation

$$h\nu_c = \hbar \frac{eB}{m_e c} = 11.57\, B_{12}\, \mathrm{keV}, \tag{2.8}$$

where we have defined $B_{12} = B/(10^{12}\mathrm{G})$. Of course, a complete treatment of Compton scattering in the proximity of a strongly magnetised stellar surface necessarily involves quantum mechanical relativistic calculation of the cross section. The scattering cross sections in the non-relativistic regime ($B \ll B_{\rm c}$) were firstly derived in the Thomson limit, neglecting electron recoil, by Ventura [15] in 1979. These calculations have proved to be fundamental for the understanding of the approximated effects of the angle, frequency and polarisation dependence of the cross sections in strong magnetic fields. Then, Herold [16] and, later, in 1983, Melrose & Parle [17] provided relativistic expressions of the magnetic Compton cross section, considering the possibility of the excitation of electrons, at least, to the first Landau state (see Appendix D). The complete quantum electrodynamics (QED) Compton cross sections were derived by Daugherty & Harding [18] in 1986 and Harding & Daugherty [19] in 1991, in which are included excitations of the electrons to an arbitrary Landau state and they depend also on the incident photon polarisation. Besides, in this case, is needed a proper treatment also of the electron spin transition and it is worth taking into account the possibility that electrons remain in an arbitrary excited state after the scattering (Raman scattering).
However, we are not interested here in a full treatment of the problem, thus we will consider much simpler approximations of the cross sections which are still valid in the regimes of our interest. The initial, but crucial, simplification we introduce is that the electrons are non-relativistic. In the non-relativistic regime and for energies $h\nu \lesssim h\nu_g$, we can assume that photons have two polarisation modes both nearly linear.
The photons having the electric field $\vec{E} \parallel \vec{k} \wedge \vec{B}$ (where $\vec{k}$ and $\vec{B}$ are the photon momentum and the external magnetic field, respectively) are called *ordinary* photons (O-photons), while those which have $\vec{E} \perp \vec{k} \wedge \vec{B}$ are named as the *extraordinary* ones (E-photons).
The normal modes have significantly different opacity, thus the mode switching remarkably affects the radiative transfer. The magnetic Thomson scattering differential cross-sections for the interaction with the plasma, under such approx-

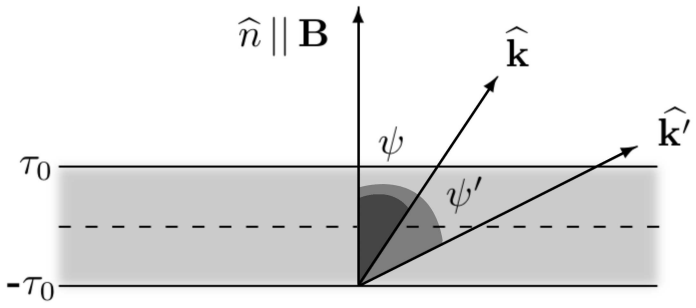

Figure 2.1: *Schematic picture of a plane-parallel slab of thermal electron plasma. The magnetic field* $\mathbf{B}$ *is oriented along the slab normal.* ψ *and* ψ' *are the angles between the magnetic field and the ingoing and outgoing photon directions, respectively.*

imations, are:

$$d\sigma_{\mathrm{O}\to\mathrm{O}}(\mu,\mu') = \frac{3}{4}\sigma_{\mathrm{T}}\big[(1-\mu^2)(1-\mu'^2) + \frac{1}{2}\left(\frac{\nu}{\nu_{\mathrm{g}}}\right)^2 \mu^2\mu'^2\big]d\mu \tag{2.9}$$

$$d\sigma_{\mathrm{E}\to\mathrm{E}}(\mu,\mu') = \frac{3}{8}\sigma_{\mathrm{T}}\left(\frac{\nu}{\nu_{\mathrm{g}}}\right)^2 d\mu' \tag{2.10}$$

$$d\sigma_{\mathrm{O}\to\mathrm{E}}(\mu,\mu') = \frac{3}{8}\sigma_{T}\left(\frac{\nu}{\nu_{\mathrm{g}}}\right)^2 \mu^2\ d\mu' \tag{2.11}$$

$$d\sigma_{\mathrm{E}\to\mathrm{O}}(\mu,\mu') = \frac{3}{8}\sigma_{T}\left(\frac{\nu}{\nu_{\mathrm{g}}}\right)^2 \mu'^2\ d\mu' \tag{2.12}$$

where $\mu = \cos\psi$ and $\mu' = \cos\psi'$ are the cosines of angles between the direction of the magnetic field and the direction of the motion of photons before and after the scattering, respectively, while $\sigma_T = 6.6524 \times 10^{-25}\mathrm{cm}^2$ is the Thomson cross-section.

Since we are interested in studying the spectral shape of the radiation induced by Comptonization in strong magnetic fields, we assume that all the initial seed photons have ordinary polarisation. Taking into account a starting non-zero amount of extraordinary seed photons would lead to a complete dominance of them in the emerging spectrum, because they escape almost freely from the medium, having a much smaller cross section, while the ordinary photons diffuse across the slab.

Therefore, we will consider hereafter as E-photons exclusively those originated from the fraction of O-photons that have changed their polarisation.

If we consider a strong magnetic field of order of $B \approx 10^{14}$G, the second term in (2.9) becomes negligible for energies up to MeV, so that the study of the spectral

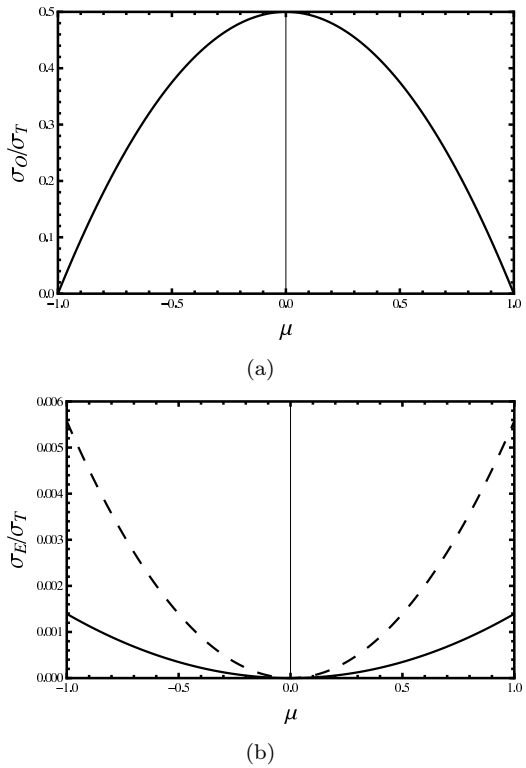

Figure 2.2: *Panel* (a)*: The solid line is the cross-section of O-photons (2.9) in units of Thomson cross section as a function of μ. Panel* (b)*: The solid and dashed lines are the cross-section of the mode-switching from O-photons to E-photons (2.11) in units of Thomson cross section as a function of μ for $h\nu = 50, 100$ keV.*

formation in the range below the electron-positron annihilation line (511 keV) is no longer affected by it. However, we will only present spectra up to ~ 100 keV in order to show clearly our results, even if would be safer not to exceed a few tens of keV to be surely in the non-relativistic regime.
In this range, the energy exchange with plasma for photons of the ordinary mode is not sensitive to the intensity of the magnetic field. On the other hand, the dependence on magnetic field strength is strong for the propagation of E-photons and for mode switching. In Fig. 2.2, we present a plot of cross-sections (2.9) and (2.11). In Panel (a), the solid line refers to the first order approximation of the O-photons cross-section, in which we are neglecting the second term in (2.9). In Panel (b) the solid and dashed lines represent the cross-section of the mode-switching $O \to E$ (2.11) for energies, $h\nu = 50, 100$ keV, respectively. Although the cross-section of the mode-switching is evidently suppressed by magnetic field, it increases rapidly as energy increases, and for energies $\gtrsim 100$ keV, we cannot

consider still valid the approximation we have made on cross-section (2.9) and we need a proper relativistic approach to the problem, but this is outside of the purpose of this thesis.

2.3 Solution of RTE in a Magnetised Medium

We study the case of a plan-parallel configuration of thermal plasma with uniform temperature distribution. The homogeneous integro-differential form of the radiative transfer equation for the ordinary mode, neglecting induced processes and considering inverse Compton as the leading process, is given by

$$\mu\frac{\partial}{\partial r}n_{\rm O}(\mu,\nu,\vec{r}) = \int dp\, d\sigma_{\rm O\to O}\{n_{\rm O}(\mu',\nu',\vec{r})N_e(p') - n_{\rm O}(\mu,\nu,\vec{r})N_e(p)\} - \sigma_{\rm O\to E}\bar{N}_e\, n_{\rm O}(\mu,\nu,\vec{r}) \tag{2.13}$$

where $N(\epsilon)$ is the electron distribution function, that we assume to be the one-dimensional Maxwellian distribution, $\bar{N}_e$ is the integrated Maxwellian. In order to find an approximate solution of the integro-differential equation (2.13), we expand both the occupation number and the Maxwellian electron distribution in Taylor series up to second order in $\Delta\nu$ and $\Delta\epsilon$, respectively [3]. After term collection, we may write equation (2.13) in a more compact form as

$$\mu\frac{\partial}{\partial r}n_{\rm O}(\mu,\nu,\vec{r}) = -\left(\sigma_{\rm OO}+\sigma_{\rm OE}\right)\bar{N}_e\, n_{\rm O}(\mu,\nu,\vec{r}) + \bar{N}_e\int d\sigma_{\rm OO}(1+\widehat{A})\, n_{\rm O}(\mu',\nu,\vec{r}), \tag{2.14}$$

where

$$\widehat{A} = \langle(\Delta\nu)^2\rangle\left[\frac{1}{2}\frac{\partial^2}{\partial\nu^2}+\frac{h}{kT}\frac{\partial}{\partial\nu}+\frac{1}{2}\left(\frac{h}{kT}\right)^2\right]+\langle\Delta\nu\rangle\left[\frac{\partial}{\partial\nu}\frac{h}{kT}\right]. \tag{2.15}$$

Note that, where an external magnetic field is present, even after the Taylor expansion, equation (2.13) does not reduce to a purely differential equation, like in the general case reported in Par. 2.2.
Following the arguments reported in L88, it worth noticing that the Comptonization parameter, which in strong magnetic fields is $y_{\rm NR} = (2/15)(4kT/m_ec^2)N_{\rm sc}$, is considerably smaller than in the unmagnetised case. Thus, we need to assume that our system is optically thick ($\tau \gg 1$), so that the number of scatterings may be large enough to make the Comptonization process effective.
The condition of large optical depth ensures us that multiple scattering occurs and, as we will discuss briefly, a sort of diffusion approximation can be applied. Indeed, we cannot simply use the usual Fokker Planck approximation (diffusion approximation), because of the intrinsic anisotropic nature of the problem. Due to the presence of the magnetic field, we should consider that photons may escape, even from large optical depths, without having done a sufficiently number

of scatterings, if they are moving at small angles $\psi < \tau^{-1}$ to the field [30]. The cross sections (2.9) and (2.11) are, indeed, angular dependent, as we have seen in Fig. 2.2 and discussed in Par. 2.3. Since both the probability of scattering in this range of angles and the probability of diffusion escape scale as $1/\tau^2$, we should take into account the amount of escaping photons in the overall energy balance. Clearly, only the photons which move at sufficiently large angles to the field undergo enough number of scatterings to be effectively Comptonized, i.e. their spectrum will deviate substantially respect to the Planck distribution. At such large angles the optical depth τ is as large as we have supposed above, and we can assume, in first approximation, that Comptonized photons diffuse almost isotropically. Therefore, under the conditions of large angles and large optical depths, we neglect the anisotropic part δn of the occupation number $n = S + \delta n$, where we have defined

$$S(\nu, r) = \frac{3}{8\pi} \int (1 - \mu^2)\ n_{\rm O}(\nu)\, d\Omega, \tag{2.16}$$

which is the angle-averaged occupation number. In fact, in this regime the relation

$$\int f(\overrightarrow{k}) \delta n\, d\overrightarrow{k} \ll S \int f(\overrightarrow{k}) d\overrightarrow{k}, \tag{2.17}$$

with $f(\overrightarrow{k})$ is a bounded function of the angles, holds. Changing the space variable from r to $\tau = \int_0^R \bar{N}_e\, \sigma_{\rm OO}\, dr$ and averaging over angles following the definition (2.16), the equation for the isotropic part $S(\nu, \tau)$ reads as

$$\begin{aligned}
&\frac{8\pi}{3}\left[\frac{4}{3}S(\nu,\tau) - \int_{-\tau_0}^{\tau_0} d\tau' \int_{-1}^{1} d\mu \frac{(1-\mu^2)^2}{|\mu|} e^{-\frac{(1-\mu^2)}{|\mu|}|\tau-\tau'|} S(\nu,\tau')\right] = \\
&+ \int_{-1}^{1} d\mu d\mu' (1-\mu^2)^3 (1-\mu'^2) \widehat{A} \int_{-\tau_0}^{\tau_0} \frac{d\tau'}{|\mu|} e^{-\frac{(1-\mu^2)}{|\mu|}|\tau-\tau'|} n_{\rm O}(\mu', \nu, \tau') \\
&- \frac{3}{8}\left(\frac{\nu}{\nu_{\rm g}}\right)^2 \int_{-1}^{1} d\mu (1-\mu^2)^2 \int_{-\tau_0}^{\tau_0} \frac{d\tau'}{|\mu|} e^{-\frac{(1-\mu^2)}{|\mu|}|\tau-\tau'|} n_{\rm O}(\mu, \nu, \tau').
\end{aligned} \tag{2.18}$$

Under the assumptions of $\tau \gg 1$ and $(1-\mu^2)/|\mu| \gtrsim 1$, if we are assuming that the occupation number is a sufficiently smooth function of τ, we can use the approximated identity

$$\frac{(1-\mu^2)}{|\mu|} \int e^{-\frac{(1-\mu^2)}{|\mu|}|\tau-\tau'|} n(\tau')\, d\tau' \approx n(\tau), \tag{2.19}$$

because the integrand function $e^{-\frac{(1-\mu^2)}{|\mu|}|\tau-\tau'|}(1-\mu^2)/|\mu|$ in this regime can be approximated by a $\delta(|\tau-\tau'|)$ function. Hence equation (2.18) may be written as

$$\begin{aligned}
&\frac{4}{3}\left[S(\nu,\tau) - \int_{-\tau_0}^{\tau_0} d\tau' K(|\tau-\tau'|) S(\nu,\tau')\right] = \\
&\frac{2}{15}\frac{kT}{m_e c^2}\frac{1}{\nu^2}\frac{\partial}{\partial\nu}\nu^4\left[\frac{\partial}{\partial\nu}S(\nu,\tau) + \frac{h}{kT}S(\nu,\tau)\right] - \frac{1}{4}\left(\frac{\nu}{\nu_{\rm g}}\right)^2 S(\nu,\tau),
\end{aligned} \tag{2.20}$$

where we have defined the kernel $K(|\tau - \tau'|)$ of the equation as

$$K(|\tau - \tau'|) = \frac{3}{4}\int \frac{(1-\mu^2)^2}{|\mu|} e^{-\frac{(1-\mu^2)}{|\mu|}|\tau-\tau'|} d\mu. \tag{2.21}$$

Equation (2.20) may be handled with the separation of variable method. Indeed, on the left hand side of (2.20) there is an integral operator depending only on space, while on the right hand side we recognise the characteristic differential Comptonization operator. Defining the dimensionless energy $x \equiv h\nu/kT$, we seek a solution of the form $S(x,\tau) \approx n(x,\tau) = s(\tau)Z(x)$. Substituting it into equation (2.20) and, introducing a source distribution of seed O-photons $\mathcal{S}(x)$, we obtain the system

$$\frac{1}{x^2}\frac{d}{dx}x^4\left(\frac{d}{dx}Z(x) + Z(x)\right) - (lx^2 + \gamma)Z(x) = \mathcal{S}(x), \tag{2.22}$$

$$\left(1 - \frac{3}{4}\lambda\right)s(\tau) = \int_{-\tau_0}^{\tau_0} d\tau' K(|\tau - \tau'|)s(\tau'), \tag{2.23}$$

where we have defined the quantities

$$\gamma = \frac{15}{2}\frac{m_e c^2}{kT}\lambda \qquad \text{and} \qquad l = \frac{15}{8}\frac{m_e c^2}{kT}\frac{1}{{x_{\rm g}}^2}\,. \tag{2.24}$$

Equation (2.22) is a "Kompaneets-like" diffusion equation, without the Z^2-term accounting for the induced processes, plus a term containing the magnetic field dependence, via $x_{\rm g}$, which is the dimensionless cyclotron energy of the electron. Equation (2.22) can be solved using the Green's function convolutional method (see Par. 2.5).
Equation (2.23) is instead an homogeneous Fredholm equation of the second kind (*eigenvalues equation*) with the logarithmically singular kernel (2.21). The solution of equation (2.23) is not straightforward, since the standard integration techniques cannot handle with a kernel singularity, even if it is moderate. We adopt an algorithm suggested by Atkinson & Shampine [31] (see Par. 2.4), which is thought specifically for kernels with a "quasi"-smooth behaviour.
The overall solution of the radiative transfer problem for the isotropic part of the O-photon occupation number described by the system (2.22)-(2.23) should be found in the form

$$n(x,\tau) = \sum_{k=1}^{\infty} n_k(x,\tau) = \sum_{k=1}^{\infty} c_k s_k(\tau) Z_k(x)\,, \tag{2.25}$$

where $s_k(\tau)$ is the kth-eigenfunction of equation (2.23) and $Z_k(x)$ is the solution of equation (2.22) for the kth-eigenvalue. The coefficients c_k are the Fourier coefficients of the series, obtained considering an exponential spatial distribution $f(\tau) = e^{-\tau/2\tau_0}$ of photons as initial condition.

2.4 Solution of the Eigenvalue Problem

The space problem is an homogeneous Fredholm integral equation of the second kind (*eigenvalue problem*), namely

$$L_\tau s(\tau) \equiv \int_{-\tau_0}^{\tau_0} K(|\tau - \tau'|) s(\tau') d\tau' = \sigma s(\tau) \tag{2.26}$$

where $\sigma = \left(1 - \frac{3}{4}\lambda\right)$. The kernel of the equation (2.26) is integral kernel

$$K(|\tau - \tau'|) = \frac{3}{4} \int_0^1 \frac{(1-\mu^2)^2}{\mu} e^{-\frac{(1-\mu^2)}{\mu}|\tau-\tau'|} d\mu. \tag{2.27}$$

Even if the kernel has a logarithmic singularity in $\tau = \tau'$, the integral operator L_τ is still compact. The property of compactness becomes evident integrating the kernel over τ'

$$\int_{-\tau_0}^{\tau_0} K(|\tau - \tau'|) d\tau' = \frac{3}{4} \int_{-\tau_0}^{\tau_0} \int_0^1 \frac{(1-\mu^2)^2}{\mu} e^{-\frac{(1-\mu^2)}{\mu}|\tau-\tau'|} d\mu \, d\tau'. \tag{2.28}$$

Performing the integration over τ', we obtain an analytical expression for the integrand function

$$\int_{-\tau_0}^{\tau_0} K(|\tau - \tau'|) d\tau' = \frac{3}{4} \int_0^1 (1-\mu^2) \left[2 - e^{-\frac{(1-\mu^2)}{\mu}(\tau_0+\tau)} - e^{-\frac{(1-\mu^2)}{\mu}(\tau_0-\tau)} \right] d\mu \,. \tag{2.29}$$

The integrand is smooth and the integral is finite, so the integral operator L_τ is a compact operator, thus it is bounded and it has a complete set of eigenvalues and eigenfunctions (see [25]).

2.4.1 Numerical Treatment of the Singularity

Even though in principle a logarithmic singularity is integrable, we have to pay attention to the behaviour of the kernel at the slab boundaries. In order to do so, we study analytically the kernel for $t = |\tau - \tau'| \to 0$. Expanding the kernel around t, we find

$$\begin{aligned} K(t) &= \frac{3}{4} \int_0^1 \frac{(1-\mu^2)^2}{\mu} e^{\mu t} e^{-\frac{t}{\mu}} d\mu \\ &\approx \frac{3}{4} \int_0^1 \frac{(1-\mu^2)^2}{\mu} \left[1 + \mu t + \frac{(\mu t)^2}{2!} + \dots \right] e^{-\frac{t}{\mu}} d\mu \,. \end{aligned} \tag{2.30}$$

If we change the variable μ into $1/y$, it is possible to write the kernel as a sum of *exponential integrals* (see Abramovitz & Stegun [2]), that for $Re(t) > 0$, are defined as

$$E_n(t) = \int_1^\infty \frac{e^{-yt}}{y^n} dy \,. \tag{2.31}$$

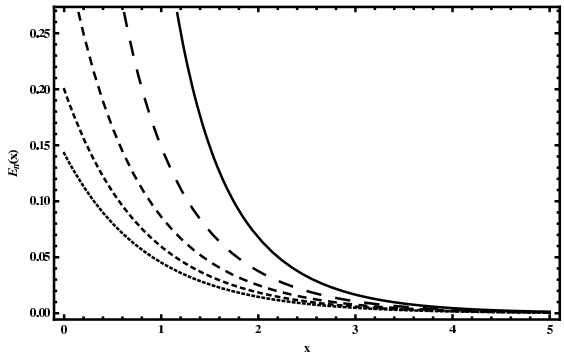

Figure 2.3: *The exponential integrals $E_n(t)$, for $n = 0, 2, 4, 6, 8$ as defined in Abramovitz & Stegun [2]. The solid line is the exponential integral with $n = 0$, the smaller is the dashing the higher is the index n.*

The exponential integrals $E_n(t)$, if $|\arg t| < \pi$, can be written also in the form [24]

$$E_n(t) = \frac{(-t)^{n-1}}{(n-1)} \left[-\log t + \psi(n)\right] - \sum_{\substack{m=0 \\ m \neq n-1}}^{\infty} \frac{(-t)^m}{(m-n+1)m!} \tag{2.32}$$

where

$$\psi(1) = -\gamma, \qquad \psi(n) = -\gamma + \sum_{m=1}^{n-1} \frac{1}{m} \qquad (n > 1) \tag{2.33}$$

and $\gamma = 0.57721...$ is Euler's constant. We note that (2.32) may be write more concisely as

$$E_n(t) = -\log t\, P(t) + Q(t), \tag{2.34}$$

where $P(t)$ is a polynomial and $Q(t)$ is a series around t. Therefore the kernel (2.27) takes the form

$$K(|\tau - \tau'|) = \frac{3}{4} \left[-\log(|\tau - \tau'|) + Q(|\tau - \tau'|)\right], \tag{2.35}$$

in which $P(|\tau - \tau'|) = 1$. In this explicit form, the logarithmic singularity has been separated from the regular part $Q(|\tau - \tau'|)$. Whereas the smooth part can be easily treated, the integration of the logarithmic term requires more attention. Indeed, a direct integration over the logarithmic part of (2.35) is not straightforward to perform with the standard analytical and numerical integration techniques (see references from [33] to [38] and Appendix A).

2.4.2 Atkinson & Shampine Method

Therefore, we adopt the algorithm described by Atkinson & Shampine ([31], hereafter AS07). They present a numerical MATLAB program, called `Fie`, which is taught for solving numerically Fredholm integral equations of the second kind

on a interval that can be either finite $[a, b]$ or semi-infinite $[0, \infty)$. The authors considered not only kernels $K(s, t)$ that are smooth functions on $R = [a, b] \times [a, b]$, but also kernels having a modest singularity behaviour across the diagonal $s = t$. `Fie` is designed to treat different kind of rather smooth kernels, which are the followings

- **Smooth** The kernel $K(s, t)$ is smooth on all R. Simpson's rule* is used to discretize the integration, then the Nyström interpolant provides an approximate solution on all the interval $[a, b]$.
- **Discontinuous** The kernel has a discontinuity in a low-order derivative across the diagonal. `Fie` uses a modified Simpson's rule which gives the same rate of convergence as the canonical Simpson's rule applied to a smooth kernel.
- **Logarithmic Singularity** The kernel can be written as

  $$K(s, t) = L(s, t) \log |s - t|,$$

  where $L(s, t)$ is a smooth function on all R. `Fie` handles the singular behaviour across the diagonal, using product integration. A graded mesh has been chosen to deal with the lack of differentiability of the solution at the end of the interval.
- **Algebraic Singularity** The kernel can be expressed as follows

  $$K(s, t) = L(s, t)/|s - t|^{\alpha},$$

  with $L(s, t)$ which is a smooth function on all R and $0 \leq \alpha \leq 1$. The singularity is handled like in the logarithmic case.

The third class of kernels considered in AS07 has the same singular behaviour which (2.35) has, therefore the algorithm is applicable to our case.
As we see from (2.35), the smooth function $L(s, t)$ for our kernel is a constant. Since we have already shown that the kernel $K(s, t)$ can be split into two terms, and each of them can be handled with the same generalised quadrature rule because of the compactness property of (2.35), we describe the algorithm considering only the logarithmic term implicitly implying that the non-singular term will be treated in the same way.

*The Simpson's rule is a scheme for the approximation of the integral of a function f using quadratic polynomials, instead of straight lines used in the trapezoidal rule. Simpson's rule also corresponds to the 3-point Newton-Cotes quadrature rule. In particular, assuming that the function f is known at points x_0, x_1 and x_2 equally spaced by the distance h and defining $f_n = f(x_n)$, then the Simpson's rule says that

$$\int_{x_0}^{x_2} f(x)dx = \int_{x_0}^{x_0+2h} f(x)dx \approx \frac{1}{3}h(f_0 + 4f_1 + f_2)\,.$$

The error in approximating an integral by Simpson's rule is $(1/90)h^5|f^{(4)}(\xi)|$, where ξ is a number between a and b.

The modified quadrature rule used by AS07 is a product Simpson's rule (see Appendix B). Mildly singular kernels, as long as they conserve compactness, are easily integrated with this method. In addition, since integral equations like

$$\lambda\, x(s) - \int_a^b \log|s-t|\, x(t)\, dt = f(s), \qquad a \le s \le b, \tag{2.36}$$

may have solutions $x(s)$ which cannot be necessarily smooth at the boundaries of the integration interval, AS07 introduced a mesh of integration points $\{t_0, \ldots, t_n\}$ which is *graded* near the integration limits, a and b, where the behaviour of the solution can be critical. The index n is always chosen to be divisible by 4, and sufficiently large, in order to guarantee the existence of a unique solution of the problem. The solution is requested to satisfy the convergence criterion for $n \to \infty$

$$||x - x_n||_\infty \le c\, ||\mathcal{K}\, x - \mathcal{K}_n\, x||_\infty \qquad (c > 0), \tag{2.37}$$

where we have defined the integral operators

$$\mathcal{K}\, x = \int_a^b \log|s-t|\, x(t)\, dt\,, \tag{2.38}$$

and $\mathcal{K}_n$ is its approximated form, that we will describe later on. Inequality (2.37) holds if the separation between the mesh points is chosen properly. Roughly speaking, the grading of the mesh should be intensified near the critical points for the integration. In particular, we want that the error $||x - x_n||_\infty$ should be, at least, of order $\mathcal{O}(n^{-p})$ with $p = 3$. The general prescription about how to calculate the nodes of the mesh given by AS07 is the following: starting from the points with odd index $j = 1, 3, \ldots, n-1$, we have

$$t_j = \frac{1}{2}(t_{j-1} + t_{j+1}), \qquad (b - t_{n-j} = t_j - a). \tag{2.39}$$

The points with even index are instead defined as

$$\begin{aligned} t_j &= a + \frac{b-a}{a}\left(\frac{2j}{n}\right)^q, \\ t_{n-j} &= b + a - t_j, \qquad\qquad j = 0, 2, 4, \ldots, n/2, \end{aligned} \tag{2.40}$$

where $q \ge 1$ is the grading parameter. If the convergence is faster enough, as in this case, $q = 3$ ensures us that $||\mathcal{K}\, x - \mathcal{K}_n\, x||_\infty = \mathcal{O}(n^{-3})$. The general integration scheme, suggested by AS07, says that for any triplet of points $\{t_{j-1}, t_j, t_{j+1}\}$ with j odd, the solution $x(t)$ is approximated with a piecewise quadratic interpolation

function $\widetilde{x}_j(t)$, so that the integral $\mathcal{K}\,x(t)$ becomes

$$\begin{aligned}\mathcal{K}\,x(t) &\equiv \int_a^b \log|s-t|\,x(t)\,dt = \sum_{\substack{j=1,\\ j\,\text{odd}}}^{n-1} \int_{t_{j-1}}^{t_{j+1}} \log|s-t|\,x(t)\,dt \\ &\approx \sum_{\substack{j=1,\\ j\,\text{odd}}}^{n-1} \int_{t_{j-1}}^{t_{j+1}} \log|s-t|\,\widetilde{x}_j(t)\,dt \\ &= \sum_{k=0}^{n} M_k(s)\,x(t_k) \equiv \mathcal{K}_n\,x(s), \end{aligned} \tag{2.41}$$

where $w_k(s)$ are the *weights* of the interpolating function over each subinterval. Thanks to the property of compactness of both terms of (2.35), we use the same mesh to calculate the non-singular part of the kernel too and, thus, we define the total weight matrix $M_k(\tau) = M_k^S + M_k^{NS}$. The solution is found solving the algebraic equation that for each eigenvalue σ is the following

$$\sigma x(\tau) = \sum_{k=0}^{n} M_k(\tau) x(\tau_k), \qquad -\tau_0 < \tau < \tau_0\,. \tag{2.42}$$

To calculate the weight matrix. We need to define three kind of integrals. Considering the quantity $h_j = t_{j+1} - t_j = t_j - t_{j-1}$ for odd j, we have

$$\begin{aligned} I_{1,j} &= \int_{t_{j-1}}^{t_{j+1}} \gamma_{1,j}(t) \log|t-s| dt, \\ I_{2,j} &= \int_{t_{j-1}}^{t_{j+1}} \gamma_{2,j}(t) \log|t-s| dt, \\ I_{3,j} &= \int_{t_{j-1}}^{t_{j+1}} \gamma_{3,j}(t) \log|t-s| dt, \end{aligned} \tag{2.43}$$

where we have defined the product functions

$$\begin{aligned} \gamma_{1,j}(t) &= \frac{(t-t_j)(t-t_{j+1})}{2h_j^2}, \\ \gamma_{2,j}(t) &= \frac{(t-t_{j-1})(t-t_{j+1})}{-h_j^2}, \\ \gamma_{3,j}(t) &= \frac{(t-t_{j-1})(t-t_j)}{2h_j^2}. \end{aligned} \tag{2.44}$$

The function $\gamma_j(t)\,\widetilde{x}_j(t)$ which interpolates better the solution $x(s)$ is a linear composition of the γ-functions

$$x_j(t) = \gamma_j(t)\widetilde{x}_j(t) = a_{1,j}\gamma_{1,j}(t) + a_{2,j}\gamma_{2,j}(t) + a_{3,j}\gamma_{3,j}(t). \tag{2.45}$$

The γ-functions should fulfil the conditions $\gamma_j(t_{j-1}) = a_{1,j}$, $\gamma_j(t_j) = a_{2,j}$, and

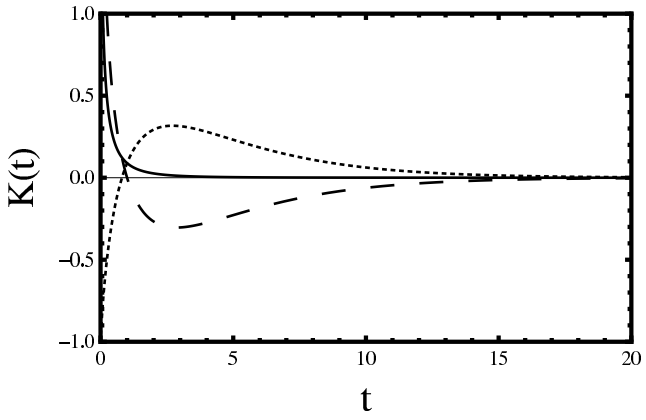

Figure 2.4: *Numerical representation of the kernel (2.35) with $t = |\tau - \tau'|$. The dotted line is the singular logarithmic part of the kernel. The dashed line describes the smooth remaining term of the kernel. The solid line is the sum of the two contributions.*

$\gamma_j(t_{j+1}) = a_{3,j}$. Considering then each triplet of nodes for j odd, and calling $x_j = \widetilde{x}_j(t_j)$, we have

$$\begin{aligned}\mathcal{K}\,x(s) &\approx \sum_{j=1,\,j\,\mathrm{odd}}^{n-1} \int_{t_{j-1}}^{t_{j+1}} \log|s-t|\,\gamma_j(t)\,x_j\,dt \\ &= \sum_{\substack{j=1,\\ j\,\mathrm{odd}}}^{n-1} \int_{t_{j-1}}^{t_{j+1}} \log|s-t|\,\left\{a_{1,j}\gamma_{1,j}(t) + a_{2,j}\gamma_{2,j}(t) + a_{3,j}\gamma_{3,j}(t)\right\} x_j\,dt \\ &= \sum_{\substack{j=1,\\ j\,\mathrm{odd}}}^{n-1} \left\{a_{1,j}\,x_{j-1}\,I_{1,j} + a_{2,j}\,x_j\,I_{2,j} + a_{3,j}\,x_{j+1}\,I_{3,j}\right\}. \end{aligned} \tag{2.46}$$

The explicit form of the sum is the following

$$\begin{aligned}\mathcal{K}\,x(s) \approx\, & a_{1,1}\,I_{1,1}\,x_0 + a_{2,1}\,I_{2,1}\,x_1 + \left(a_{3,1}\,I_{3,1} + a_{1,3}\,I_{1,3}\right) x_2 \\ & + a_{2,3}\,I_{2,3}\,x_3 + \left(a_{3,3}\,I_{3,3} + a_{1,5}\,I_{1,5}\right) x_4 + \ldots \\ & + \cdots + \left(a_{3,n-3}\,I_{3,n-3} + a_{1,n-1}\,I_{1,n-1}\right) x_{n-2} \\ & + a_{2,n-1}\,I_{2,n-1}\,x_{n-1} + a_{3,n}\,I_{3,n}\,x_n\,. \end{aligned} \tag{2.47}$$

If we define the weight matrix for the singular part of the kernel as

$$M^S_{kj} = \begin{cases} a_{1,1}\,I_{1,1}(t_k) & j = 0 \\ a_{2,j}\,I_{2,j}(t_k) & j \text{ odd} \\ \left[a_{3,j-1}\,I_{3,j-1}(t_k) + a_{1,j+1}\,I_{1,j+1}(t_k)\right] & j \text{ even}, j \neq 0, n \\ a_{3,n-1}\,I_{3,n-1}(t_k) & j = n, \end{cases}$$

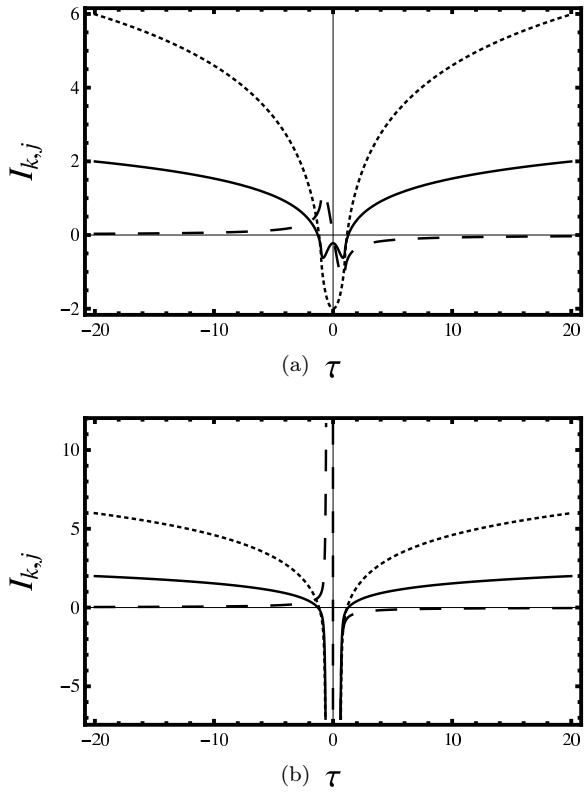

Figure 2.5: *Panel* (a)*: The figure presents the analytical expressions of the auxiliary integrals for small* $|\beta|$ *(2.51). Panel* (b)*: Same picture of Panel* (a) *but for large* $|\beta|$ *(2.53).*

we finally obtain the algebraic system

$$\sum_{j=0}^{n} M_{kj} x_j = \sigma_k x_k \,, \tag{2.48}$$

where the matrix M_{kj} is the sum of M_{kj}^{S} which are the weights for the singular part of the kernel, and M_{kj}^{NS}, that accounts for the smooth part of $\mathcal{K}(|\tau - \tau'|)$. The matrix M_{kj}^{NS} is calculated applying the same algorithm without loss of generality. The integrals $I_{1,j}, I_{2,j}, I_{3,j}$ can be rewritten using the auxiliary integrals method [32], which consists in replacing the actual integration function with a suitable *auxiliary* (primitive function) that facilitates the integration. In terms

of auxiliary integrals, the integrals (2.43) reads as

$$\begin{aligned} I_{1,j} &= \frac{1}{3} h_j \log h_j + \frac{h_j}{2} \left[I_2(\beta) - I_1(\beta) \right], \\ I_{2,j} &= \frac{4}{3} h_j \log h_j + h_j \left[I_0(\beta) - I_2(\beta) \right], \\ I_{3,j} &= \frac{1}{3} h_j \log h_j + \frac{h_j}{2} \left[I_2(\beta) + I_1(\beta) \right], \end{aligned} \tag{2.49}$$

where we have defined as auxiliary integrals

$$I_k(\beta) = \int_{-1}^{1} u^k \log |u - \beta| du, \qquad k = 0, 1, 2 \tag{2.50}$$

with $\beta = (s - t_j)/h_j$. These integrals, in the case of relatively small $|\beta|$, have the analytical expressions

$$\begin{aligned} I_0(\beta) &= (1-\beta)\log|1-\beta| + (1+\beta)\log|1+\beta| - 2, \\ I_1(\beta) &= -\beta + \frac{1}{2}(1-\beta^2)\log\left|\frac{1-\beta}{1+\beta}\right|, \\ I_2(\beta) &= -\frac{2}{9}(1+3\beta^2) + \frac{1}{3}(1-\beta^3)\log|1-\beta| + \frac{1}{3}(1+\beta^3)\log|1+\beta|. \end{aligned} \tag{2.51}$$

However, for graded mesh $|\beta|$ can be quite large and we need more sophisticated expressions for auxiliary integrals to deal with large $|\beta|$ properly. Equation (2.50) becomes

$$I_k(\beta) = \int_{-1}^{1} u^k \left\{ \log|\beta| + \log\left|1 - \frac{u}{\beta}\right| \right\} du. \tag{2.52}$$

Expanding the term $\log|1 - u/\beta|$ in Taylor series, for $|\beta| > 10$, we use the approximations given by AS07, which are

$$\begin{aligned} I_0(\beta) &\approx 2\log|\beta| - 2\left\{ \frac{1}{6\beta^2} + \frac{1}{20\beta^4} + \frac{1}{42\beta^6} + \frac{1}{72\beta^8} + \frac{1}{110\beta^{10}} + \frac{1}{156\beta^{12}} \right\}, \\ I_1(\beta) &\approx -2\left\{ \frac{1}{3\beta} + \frac{1}{15\beta^3} + \frac{1}{35\beta^5} + \frac{1}{63\beta^7} + \frac{1}{99\beta^9} + \frac{1}{143\beta^{11}} \right\}, \\ I_2(\beta) &\approx \frac{2}{3}\log|\beta| - 2\left\{ \frac{1}{10\beta^2} + \frac{1}{28\beta^4} + \frac{1}{54\beta^6} + \frac{1}{88\beta^8} + \frac{1}{130\beta^{10}} + \frac{1}{180\beta^{12}} \right\}. \end{aligned} \tag{2.53}$$

Each of these expressions accounts for an error which is negligible.

2.5 Green's Function of the RTE Energy Operator

The energy problem (2.22) is an inhomogeneous differential equation or, to be more specifically, a confluent hypergeometric equation which is typically solved with the Green's function method. After collecting terms, we obtain a more explicit form of (2.22), which is

$$x^2 \frac{d^2 Z}{dx^2} + \left(4x + x^2\right) \frac{dZ}{dx} + \left(4x - lx^2 - \gamma\right) Z = \frac{\delta(x - x_0)}{x^3}, \tag{2.54}$$

where, following the Green's function prescription, the source term $\mathcal{S}(x)$ on the right hand side has been replaced by a delta function $\delta(x - x_0)$, divided by x^3, representing a monochromatic source of injected photons. The solution of the equation is given by the Green's function which has the general form

$$G(x, x_0) = \frac{\varrho(x_0)}{x_0^3 p(x_0) w[Z_1(x_0), Z_2(x_0)]} \begin{cases} Z_1(x)Z_2(x_0), & x \leq x_0, \\ Z_1(x_0)Z_2(x), & x \geq x_0, \end{cases} \tag{2.55}$$

where $\varrho(x_0)$ is an integrand factor which allows to write the correspondent homogeneous equation of the (2.54) in the self-adjoint form

$$[p(x)Z'(x)]' + q(x)Z(x) = 0, \tag{2.56}$$

and $w[Z_1(x_0), Z_2(x_0)]$ is the wronskian of the two solutions of (2.56).
The integrand factor is defined as

$$\varrho(x) = e^{\int \frac{b(x)}{a(x)} dx}. \tag{2.57}$$

For equation (2.54) $a(x) = 1$ and $b(x) = 1 + 4/x$, thus, in our case, the integrand factor is $\varrho(x) = x^4 e^x$. Once that the self-adjoint form of (2.54) has been found, we should expect for a solution in the form $Z(x) = x^{-2} e^{-x/2} W(x)$ [66] where $W(x)$ are the Whittaker functions [2]. The homogeneous equation then becomes

$$\frac{d^2W}{dx^2} + W\left[-\frac{(\gamma + 2)}{x^2} + \frac{2}{x} - l - \frac{1}{4}\right] = 0. \tag{2.58}$$

Defining $z = x\sqrt{1 + 4l}$ we obtain

$$\frac{d^2W_z}{dz^2} + W_z\left[-\frac{1}{z^2}\left(\frac{1}{4} - \frac{9}{4} - \gamma\right) + \frac{1}{\sqrt{1 + 4l}}\frac{2}{z} - \frac{1}{4}\right] = 0, \tag{2.59}$$

which, after some algebra, explicitly becomes the Whittaker equation

$$\frac{d^2W_z}{dz^2} + W_z\left[\frac{1}{z^2}\left(\frac{1}{4} - m^2\right) - \frac{1}{4} + \frac{k}{z}\right] = 0, \tag{2.60}$$

where

$$k = \frac{2}{\sqrt{1 + 4l}} \qquad \text{and} \qquad m = \sqrt{\frac{9}{4} + \gamma}. \tag{2.61}$$

The two linearly independent solutions of equation (2.60) are

$$\begin{aligned} M_{k,m}(z) &= e^{-\frac{z}{2}} z^{m+1/2}\ {}_1F_1\left(\frac{1}{2} + m - k, 1 + 2m, z\right), \\ W_{k,m}(z) &= e^{-\frac{z}{2}} z^{m+1/2} U\left(\frac{1}{2} + m - k, 1 + 2m, z\right). \end{aligned} \tag{2.62}$$

The explicit form of the solutions of the homogeneous equation (2.54) are then the following

$$\begin{cases} Z_1(x) = e^{-\frac{x}{2}} x^{-2} e^{-\frac{x}{2}\sqrt{1+4l}} (x\sqrt{1 + 4l})^{m+1/2} 1F_1\left(\frac{1}{2} + m - k, 1 + 2m, x\sqrt{1 + 4l}\right), \\ Z_2(x) = e^{-\frac{x}{2}} x^{-2} e^{-\frac{x}{2}\sqrt{1+4l}} (x\sqrt{1 + 4l})^{m+1/2} U\left(\frac{1}{2} + m - k, 1 + 2m, x\sqrt{1 + 4l}\right), \end{cases} \tag{2.63}$$

and their associated wronskian is

$$w\left[Z_1(x), Z_2(x)\right] = e^{-x}x^{-4}\sqrt{1+4l}\frac{\Gamma(1+2m)}{\Gamma(1/2+m-k)}. \tag{2.64}$$

Thus, the Green's function of equation (2.54) is given by

$$G(x,x_0) = \frac{e^{\frac{x_0}{2}\left(1-\sqrt{1+4l}\right)}}{x_0\,\Gamma(2\alpha+4)} \times$$

$$\begin{cases} {}_1F_1(\alpha+2-k, 4+2\alpha, x\sqrt{1+4l})e^{-\frac{x}{2}\left(1+\sqrt{1+4l}\right)} \left(\dfrac{x}{x_0}\right)^{\alpha+3} I(x_0,\alpha,l), & x \le x_0, \\ {}_1F_1(\alpha+2-k, 4+2\alpha, x_0\sqrt{1+4l})e^{-\frac{x_0}{2}\left(1+\sqrt{1+4l}\right)} \left(\dfrac{x}{x_0}\right)^{-\alpha} I(x,\alpha,l), & x \ge x_0, \end{cases} \tag{2.65}$$

where the function

$$I(\alpha,x,l) = \int_0^\infty (x\sqrt{1+4l}+t)^{\alpha+1+\frac{2}{\sqrt{1+4l}}} t^{\alpha+1-\frac{2}{\sqrt{1+4l}}} e^t dt, \tag{2.66}$$

is evaluated using the steepest descend method (see Appendix C), and α is the spectral index

$$\alpha = -\frac{3}{2} + \sqrt{\frac{9}{4}+\gamma}, \tag{2.67}$$

which defines the final shape of the spectrum. The spectral index depends on the eigenvalue of the space equation (2.23) through the parameter γ which is proportional to λ as described in the first relation in (2.24), therefore we have a Comptonization mode for each eigenvalue. Once we get the Green's function of equation (2.54), it is possible to obtain the O-photons emerging Comptonization spectrum for a proper seed photon energy distribution $\mathcal{S}(x)$ through the integral convolution

$$Z_{O,k}(x) = \int_0^\infty G_O(x,x_0,\lambda_k)\mathcal{S}(x_0)\,dx_0, \tag{2.68}$$

which is, indeed, the solution of (2.22) for a single eigenvalue λ_k of equation (2.23).

2.6 Angular Distribution and Specific Intensity

The solution of the system (2.22)-(2.23) for a particular eigenvalue is

$$n_k(\nu,\tau) = s_k(\tau)Z_k(\nu), \tag{2.69}$$

thus we can write the specific intensity $I = h\nu^3 n/c^2$ as a series of products of two functions with separated dependences on the independent variables, energy

and space. Therefore, apart from dimensional factors and using the solutions obtained from (2.22)-(2.23), the specific intensity is

$$I(x,\mu,\tau) \approx \sum_{k=1}^{\infty} c_k J_k(\mu,\tau) Z_k(x), \tag{2.70}$$

where $Z(x)$ is given by (2.68), in which we dropped the label "O" for the sake of clarity, while the angular distribution is related with the eigenfunctions $s_k(\tau)$, solutions of the space problem (2.23), as described in the following relation

$$J_k(\mu,\tau) = \begin{cases} (1-\mu^2)\displaystyle\int_{-\tau_0}^{\tau} e^{-\frac{(1-\mu^2}{\mu}(\tau-\tau')} s_k(\tau')\frac{d\tau'}{\mu}\,, & \mu > 0, \\ -(1-\mu^2)\displaystyle\int_{\tau}^{\tau_0} e^{\frac{(1-\mu^2}{\mu}(\tau'-\tau)} s_k(\tau')\frac{d\tau'}{\mu}\,, & \mu < 0. \end{cases} \tag{2.71}$$

The coefficients c_k are calculated as the projection of the eigenfunctions over the spatial distribution of the source, i.e.

$$c_k = \int_{-\tau_0}^{\tau_0} s_k(\tau') e^{-\frac{\tau'}{2\tau_0}} d\tau', \tag{2.72}$$

where we have assumed that the initial spatial distribution is exponential.
However, we should recall that in equation (2.13) we have included also the term which accounts for mode-switching from O to E, thus we should calculate the contribution to the total specific intensity provided by the population of extraordinary photons which has been created by this mechanism.
After having performed the angular integration which leads to equation (2.18), we notice that the term accounting for the creation of E-photons is angle-independent. Thus, the E-photons originated via mode-switching $O \to E$ from a fraction of the O-photons, can be considered isotropically distributed, namely $I_E = Z_E$, where Z_E is their energy flux defined as (see L88)

$$Z_E(x) = \frac{1}{4}\left(\frac{x}{x_g}\right)^2 \sum_{k=1}^{n} Z_{O,k}(x) \int_{-\tau_0}^{\tau_0} s_k(\tau) d\tau, \tag{2.73}$$

with $Z_{O,k}(x)$ as calculated in (2.68). The flux of E-photons turns out to be, under this very rough approximation, a small fraction respect to the sum of $Z_{k,O}$ over all k, and, besides, further modulated by the sum of the eigenfunction integrals and suppressed by the magnetic field.

3

Emerging Spectra in Strong Magnetic Field

In Chap. 2, we have discussed the details which lead us to the solution of the radiative transfer problem for a plane parallel slab of thermal plasma in presence of a strong magnetic field. We have obtained the solution of the radiative transfer equation through separation of variables under the assumptions of large angles θ and large optical depth τ. We have solved a system of two equations resulting from the separation of variables and we have found the overall solution as an infinite series. Each term of the series is a product of two functions with separated dependences on energy and space, which are solutions of the two equations of the system.
In this Chapter we present the solution of the two equations, separately, and the entire solution of the problem. Then, we discuss our results and we compare them to those formerly derived in L88.

3.1 Solution of the Space Equation: Eigenvalues & Eigenvectors

Since energy equation (2.22) can be solved only if we know eigenvalues and eigenfunctions of the space equation (2.23), we need to solve, at first, the eigenvalue problem. The algorithm we have described in Chapter 2, in principle, is able to find all the terms of the infinite series of eigenvalues and eigenvectors. Nonetheless, the limitation comes from the numerical accuracy. We assess, as distinct eigenvalues, near eigenvalues which differ, at least, at the order of 10^{-3}.
In Panel (a) of Fig. 3.1 we show five sets of 64 eigenvalues for increasing maximum optical depth τ_0 (from filled circles to filled down triangles). The number of eigenvalues we have chosen to plot is completely arbitrary, the only request needed is that the number should be a multiple of 4, because of the kind of grid we want to

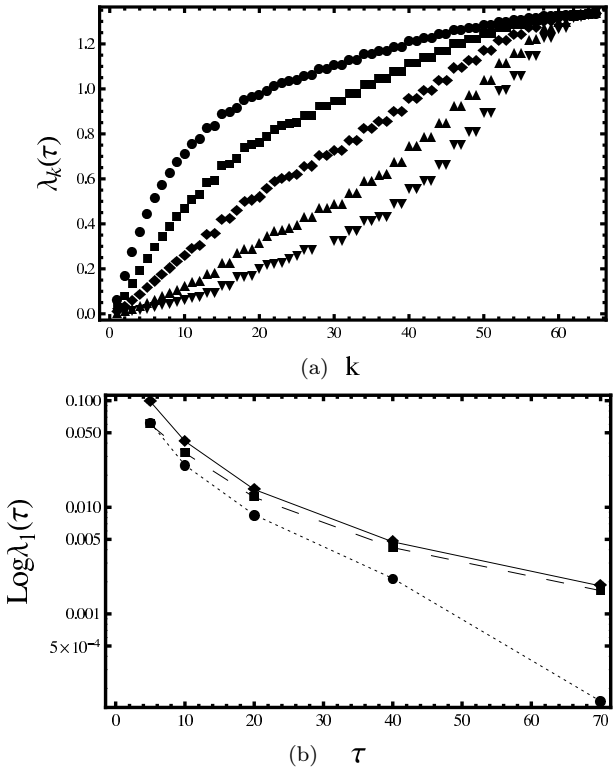

Figure 3.1: *Panel* (a)*: Five series of eigenvalues of equation (2.23) for optical depths* $\tau_0 = 5, 10, 20, 40, 70$*. The filled dots are the eigenvalues for* $\tau_0 = 5$*, the filled squares for* $\tau_0 = 10$*, the filled rhombuses for* $\tau_0 = 20$*, the filled up triangles* $\tau_0 = 40$ *and the filled down triangles for* $\tau_0 = 70$*. Panel* (b)*: Comparison between first eigenvalue obtained with different methods and optical depth* τ_0 *as defined in Panel* (a)*. The filled rhombuses are the numerical eigenvalues we found with the method described in Chapter 2. The filled squares represent the eigenvalues obtained with the variational approach proposed by Lyubarskii (3.2). The filled circles are the first eigenvalues as calculated in (3.1).*

consider. We have defined in Appendix (2.4) the relation $\sigma_k = 1 - 3\lambda_k/4$, where σ_k are the eigenvalues we found directly from the AS technique. The calculation of the actual eigenvalues λ_k from the above relation is straightforward. As we expect, all the sets of eigenvalues λ_k are monotonically increasing from a value close to zero up to the saturation value ~ 1.3.

Although we are able to find with this algorithm the entire set of eigenvalues, it is worth noticing that we obtain perfectly distinguishable eigenvalues for $k \lesssim 10$ due to the error introduced by numerical treatment, and the calculation becomes

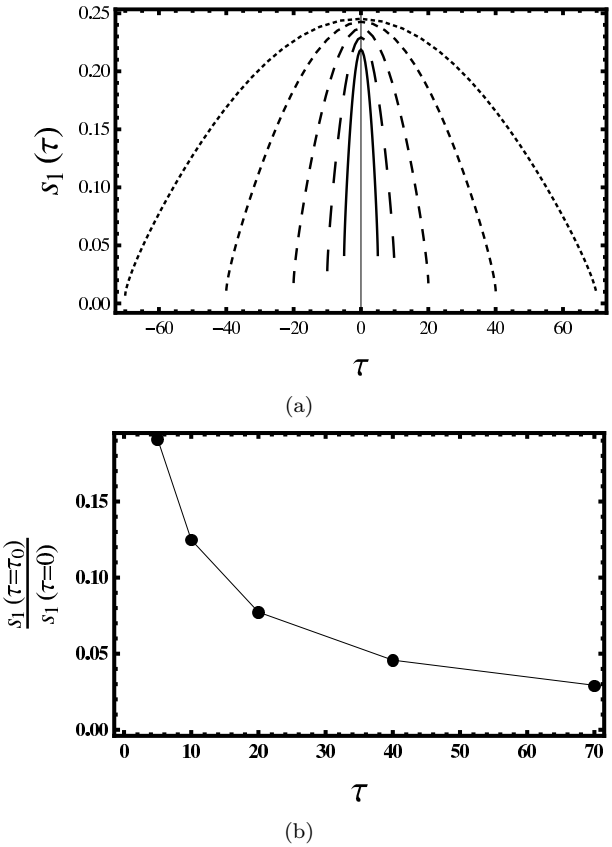

Figure 3.2: *Panel* (a)*: First eigenfunctions for different values of maximum optical depth* $\tau_0 = 5, 10, 20, 40, 70$ *(from solid to dotted line as* τ_0 *increases). Panel* (b)*: The dots represent the ratio between the values of the first eigenfunction at the boundary of the slab* $\tau = \tau_0$ *and at the centre* $\tau = 0$*.*

more and more complex for increasing maximum optical depth. However, the physical upper limit to the optical depth of the simplified system under consideration can be reasonably set to $\tau_0 \approx 20$, which we will consider from now on as the value of optical depth when it will be assumed as a constant. Large optical depth is required in order to maintain the system in the regime of unsaturated Comptonization and multiple scattering. Additionally, we will show that, not only eigenvalues with $k \gtrsim 10$ are not necessary for the understanding of the physics, but that the leading term in the series is indeed exclusively the first ($k = 1$).
In Panel (b) of Fig. 3.1, we compare the first eigenvalue that we obtain from numerical computations with respect to the analytical estimates performed in L88. Lyubarskii provides two estimates of the first eigenvalue: one is obtained performing a Fourier transform of the kernel (2.21), assuming $\tau_0 \to \infty$, which

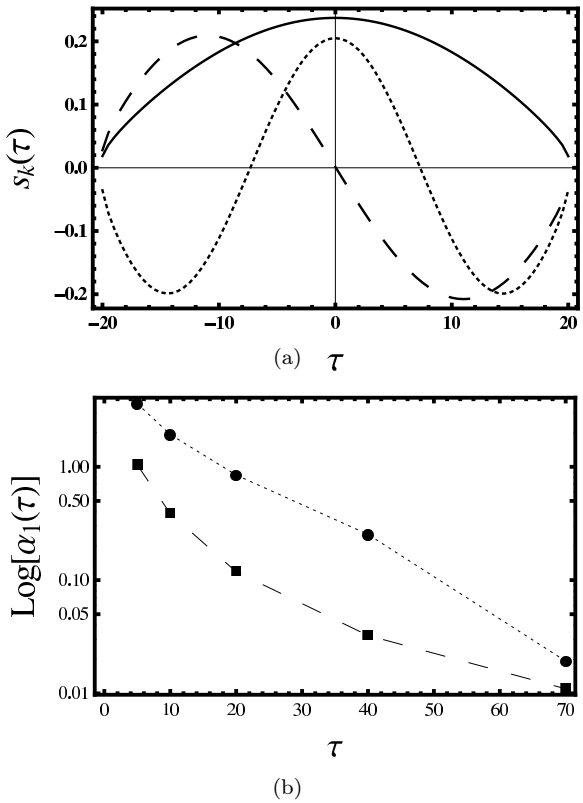

Figure 3.3: *Panel* (a)*: Eigenfunctions for* $k = 1, 2, 3$ *and maximum optical depth* $\tau_0 = 20$*. Panel* (b)*: The points present on the dotted line indicate the spectral index of the flux when a strong magnetic field is present (3.5). The points on the dashed line represents the case in which there is a negligible, or relatively small, magnetic field (3.6).*

gives

$$\lambda_1 = \frac{\pi^2}{4\tau_0^2}(\log 4\tau_0 - 2), \tag{3.1}$$

instead, the other estimate, which is

$$\lambda_1 = \frac{5}{2\tau_0^2}\left(\log 8\tau_0 + \gamma - \frac{13}{3}\right), \tag{3.2}$$

is found solving (2.23) with a variational method. Here γ is the Euler's constant $0.577\ldots$. As suggested by the author, the relation (3.1) is no longer satisfied if we are in the case of large optical depths ($\tau_0 \gtrsim 20$). Nevertheless, the eigenvalue obtained by (3.2) is, by definition, an upper limit of the exact value of λ_1, hence we expect smaller first eigenvalues for fixed optical depth. Even though the behaviour is quite similar, especially at small τ, the numerical computation finds smaller eigenvalues with respect to the eigenvalues obtained either from the

variational method or from the Fourier transformation of the kernel.
Panel (a) of Fig. 2.4 represents the first eigenfunction for different values of maximum optical depth τ_0. The plot shows that, in analogy with other physical situations, like, for instance, a potential well with increasing height, eigenfunctions are decreasing at the boundaries, approaching zero as $\tau \to \infty$. Then, we suggest that the larger is the optical depth the smaller is the number of photons which escape from the slab boundary, the closer is the regime of saturated Comptonization. This behaviour can be seen, even more clearly, if we compare the ratio of the eigenfunction at $\tau = \tau_0$ and at $\tau = 0$ (right panel in Fig. 2.4). The ratio rapidly decreases to zero as optical depth becomes larger and larger. Comparing this result with respect to the analytic expression of the first eigenfunction considered in L88, which is

$$s_1(\tau) = 1 - \left(\frac{\tau}{\tau_0}\right)^2, \tag{3.3}$$

it is evident that this function cannot describe the actual eigenfunction at the boundaries. In fact, in order to proceed with the calculations, Lyubarskii introduces a modified first eigenfunction, namely

$$\widetilde{s_1}(\tau) = s_1(\tau) + \frac{3}{2\tau_0}\int_0^1 \mu \left[e^{-\frac{(1-\mu^2)}{\mu}(\tau_0-\tau)} + e^{-\frac{(1-\mu^2)}{\mu}(\tau_0+\tau)}\right] d\mu \tag{3.4}$$

in which the integral term gives a nonzero contribution at $\tau = \tau_0$.
In Panel (a) of Fig. 3.3 we present the eigenfunctions $s_k(\tau)$ for $k = 1, 2, 3$ and maximum optical depth $\tau_0 = 20$. It is worth noticing that the eigenfunctions $s_k(\tau)$ are quite similar in shape and parity to the eigenfunctions of other physical problems, such as the one-dimensional harmonic oscillator. The eigenfunctions are orthogonal and normalized to unity. Besides, all eigenfunctions turn out to be nonzero, at the slab boundary.
A crucial test that we can do in order to verify our results is to draw comparisons with a known and well studied similar system. In Panel (b) of Fig. 3.3 we compare the spectral index of the emerging energy flux for different maximum optical depth values both in the case of a strong magnetic field and without a considerably large magnetic field. The analytic expression of the spectral index that we obtain in presence of a strong magnetic field is

$$\alpha_{\mathrm{mag,k}} = -\frac{3}{2} + \sqrt{\frac{9}{4} + \frac{15}{2}\frac{m_e c^2}{kT_e}\lambda_k}. \tag{3.5}$$

In principle, we can calculate the spectral index for any eigenvalue, and thus for any Comptonization mode. Following Sunyaev & Titarchuk [66], when the magnetic field is negligible, or, at least, well at below its critical value ($B = 4.4\times10^{13}$G), for a planar geometry, the spectral index is described by the relation

$$\alpha_{\mathrm{nomag}} = -\frac{3}{2} + \sqrt{\frac{9}{4} + \frac{m_e c^2}{kT_e}\lambda}, \tag{3.6}$$

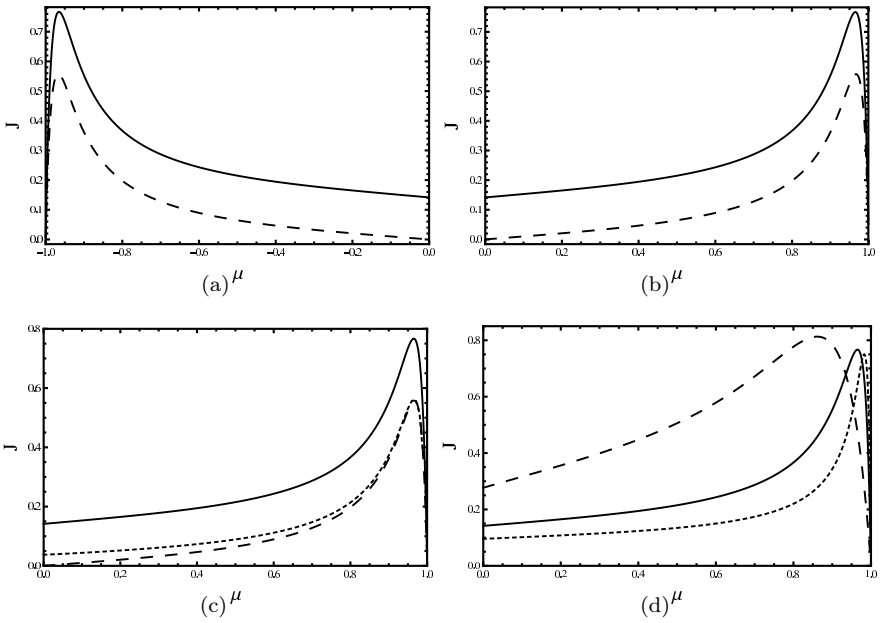

Figure 3.4: *Panel (*a*): Angular distribution of O-photons for* $-1 \leq \mu \leq 0$*. Panel (*b*): Angular distribution of O-photons for* $0 \leq \mu \leq 1$*. The solid line is the angular distribution for the first eigenfunction obtained with the algorithm described in Chapter 2. The dashed line presents the angular distribution for the first eigenfunction defined by Lyubarskii. Panel (*c*): The same figure of Panel (*b*), but with the dotted line representing the corrected angular distribution (3.8). Panel (*d*): Angular distribution of O-photons for* $0 \leq \mu \leq 1$*. The dotted line is the angular distribution calculated for* $\tau_0 = 5$*, the solid line is the same for* $\tau_0 = 20$ *and the dashed line is for* $\tau = 40$*.*

where λ accounts exclusively for the first eigenvalue and reads as

$$\lambda = \frac{\pi^2}{12\left(\tau_0 + \frac{2}{3}\right)^2}. \tag{3.7}$$

In the case of not remarkably large magnetic fields, the authors claimed that the contribution of the first eigenvalue, i.e. the first Comptonization mode, is the leading term in the series (2.25), and consequently the main contribution to the formation of the emerging spectrum. As we will discuss in the Par. 3.3, the magnetic field no longer affects the number of leading terms in the series. We find that the spectral index of the first Comptonization order in the strong magnetic field case is larger with respect to the unmagnetised case for any considered value of optical depth. Indeed, the magnetic field makes the Comptonization process less efficient overall, because photons, travelling at small angles to the field lines, undergo a small amount of scattering, giving no contribution to the high energy

k	$\lambda_k(\tau=\tau_0)$	$\alpha_k(\tau=\tau_0)$
1	0.0085	0.8460
2	0.0297	2.1922
3	0.0555	3.3498
4	0.0838	4.3623
5	0.1130	5.2496

τ	$\lambda_1(\tau)$	$\alpha_1(\tau)$
5	0.0622	3.6101
10	0.0248	1.9290
20	0.0085	0.8460
40	0.0021	0.2533
70	0.0001	0.0193

Table 3.1: *Left: Eigenvalues λ_k and spectral index α_k (3.5) for $k = 1, 2, 3, 4, 5$ and fixed optical depth $\tau_0 = 20$. Right: First eigenvalue $\lambda_1(\tau)$ and related spectral index $\alpha_1(\tau)$ for optical depth $\tau = 5, 10, 20, 40, 70$.*

part of the spectrum.
Following this considerations, we calculate the angular distribution J, as defined in equation (2.71), assuming that the first eigenfunction gives the dominant contribution. In Panel (a)-(b) of Fig. 3.4 we compare the angular distribution we obtain with the algorithm described in Chap. 2 (solid line) and the angular distribution calculated using the first eigenfunction suggested in L88 (dashed line). The distributions appear qualitatively the same, except for a scale factor. The normalization gap remains practically unchanged even if we use the angular distribution

$$\widetilde{J}(\mu,\tau_0) = \frac{2}{\chi\tau_0} - \frac{2}{(\chi\tau_0)^2} + \left[\frac{2}{\chi\tau_0} - \frac{2}{(\chi\tau_0)^2}\right] e^{-2\chi\tau_0} + \frac{3\chi}{2\tau_0}\left(\frac{2+\chi^2}{2\sqrt{4+\chi^2}}\log\left[\frac{2+\chi+\sqrt{4+\chi^2}}{2+\chi-\sqrt{4+\chi^2}}\right] - 1 - \frac{\chi}{2}\log\chi\right), \qquad (3.8)$$

calculated including the corrected first eigenfunction (3.4) introduced in L88. Here we have defined the quantity $\chi = (1-\mu^2)/\mu$. However, the angular distribution (3.8), which has been corrected including the boundary effect, does not vanish at $\mu = 0$ as it results from our estimates and it is due to the use of the eigenfunction (3.4).
Panel (d) of Fig. 3.4 presents the change in the angular distribution for $\tau = 5, 20, 40$. The peak of the distribution becomes wider and is shifting through the centre of the slab as the optical depth increases. As expected, for $\tau \to \infty$ the function J tends to be flatter throughout the slab, approaching to an isotropic distribution of the photons.

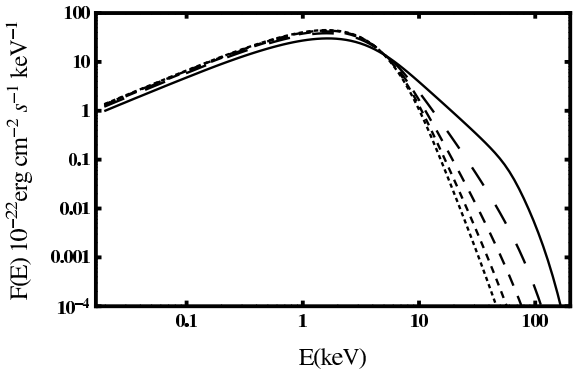

(a)

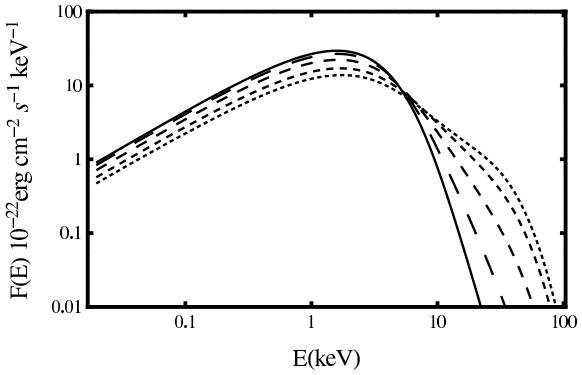

(b)

Figure 3.5: *Panel* (a)*: Energy fluxes, solution of equation (2.22) for eigenvalues* λ_k *with* $k = 1, 2, 3, 4, 5$ *(see the left table in Tab. (3.1)) and maximum optical depth* $\tau_0 = 20$*. The index* k *increases from solid to dotted line. Panel* (b)*: Energy fluxes, as in Panel* (a) *for spectral index* $\alpha(\tau, \lambda_1)$ *defined in the relation (3.5) and maximum optical depth* $\tau_0 = 5, 10, 20, 40, 70$*. The values of the spectral indexes and eigenvalues are reported in Tab. 3.1*

3.2 Solution of Energy Equation: Energy Fluxes

Once that eigenvalues and eigenfunctions have been found and studied, we are able to handle equation (2.22) and seek the energy emerging flux. However, before we should choose initial distribution and position of the injected photons. We assume that photons propagate from the bottom of the slab through the upper boundary and we consider as seed photon spectrum a blackbody distribution

$$S(x) = Ce^{-\tau/2\tau_0} kT_e^3 \frac{x^3}{e^{x(kT_e/kT_{\rm bb})} - 1} \tag{3.9}$$

at temperature $kT_{\rm bb}$ where kT_e is the electron temperature and $C = R_{\rm Km}/D_{10}^2$ a normalization constant with a blackbody emitting area in kilometres $R_{\rm Km}$ and a source distance in units of 10 Kpc D_{10}.
For all the figures we are going to discuss from now on, we assume a magnetic field of order of $B \sim 10^{14}$ G, blackbody temperature $kT_{\rm bb} \sim 1$ keV and a plasma temperature $kT_e \sim 10$ keV.
In Fig. 3.5, the left panel represents the energy flux for eigenvalues λ_k with ($k = 1, 2, 3, 4, 5$) for a fixed maximum optical depth $\tau_0 = 20$. It is worth noting that the Comptonization mode, relative to the first eigenvalue, dominates at high energies, which is precisely what happens in the case of pure thermal Comptonization, like was predicted, for instance, by [66]. Also L88 made this assumption in order to find an analytical solution of equation (2.23), but the author never verified it. We extended the solution of L88 in order to study higher orders of the series and verify if the assumption of taking as leading term exclusively the first, still holds within a good approximation.
Panel (a) of Fig. 3.5 demonstrates that, above the blackbody peak (for a $kT_{\rm bb} \approx 1$ is of order of ~ 3 keV), the first Comptonization mode is completely dominant with respect to the others. In the left table of Tab. 3.1, we present the eigenvalues $\lambda_k(\tau = \tau_0)$, found as described in the Par. 3.1, and the spectral index $\alpha_k(\tau = \tau_0)$ (3.5) for $k = 1, 2, 3, 4, 5$ and fixed optical depth $\tau_0 = 20$. As we expect from relation (3.5), the larger is the eigenvalue, the larger is the index, which means that the spectrum becomes steeper and steeper. In particular, the step between the first and the second eigenvalue is peculiar: even though eigenvalues and indexes are, in good approximation, equally separated, basically only the first energy flux remarkably differs from a "BB-like" spectrum. Of course, this statement holds if the system remains in the regime of multiple scattering and unsaturated Comptonization. On the other hand, higher orders give a relevant contribution to the soft energy peak, nonetheless, even if we do not include such terms, this feature can be modelled with an additional blackbody component with a proper normalization [43][74][81][82][83].
In Panel (b) of Fig. 3.5, we present five energy fluxes for increasing maximum optical depth $\tau_0 = 5, 10, 20, 40, 70$. The optical depth becomes larger from solid to dotted line. Varying τ corresponds to a change in the spectral index α as pointed out in the right table of Tab. 3.1. The spectral indexes considered here are those relative to the first eigenvalue. We found that the larger is the optical depth, the flatter becomes the spectrum and, as in the previous case, it is possible to see that, directly from the table. Indeed, the spectral index drops rapidly for increasing optical depth. Smaller indexes imply more and more Comptonized spectra that physically can be interpreted as the approach of the spectrum to saturation as $\tau \to \infty$. Therefore, photons get scattered more efficiently and gain a large amount of energy, shifting to the high energies part of the spectrum.

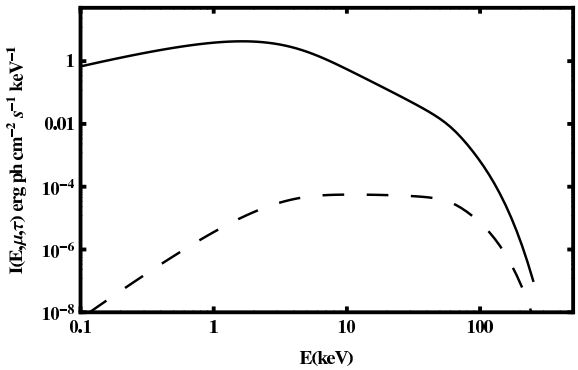

Figure 3.6: *The solid line is the solution of equation (2.14), i.e. the specific intensity of O-photons (3.10) and the dashed line is the specific intensity of E-photons created via mode-switching from a fraction of O-photons as calculated in (2.73) for* $\tau_0 = 20$ *and* $\lambda_1 = 0.0085$.

3.3 Specific Intensity

As a consequence of the above considerations, we consider only the first term of the series of Comptonization mode, thus the specific intensity for the ordinary photons is

$$I(x, \mu, \tau) \approx J_1(\mu, \tau_0) Z_1(x) \tag{3.10}$$

where the angular distribution $J_1(\mu, \tau_0)$ is calculated following (2.71) including exclusively the eigenfunction $s_1(\tau)$, and $Z_1(x)$ is the energy flux for the first eigenvalue $\lambda_1(\tau)$ at $\tau_0 = 20$. We include in Fig. 3.6, together with the specific intensity for the O-photons, the specific intensity of that fraction of photons which changes polarisation mode during the scattering process, becoming extraordinary photons. The amount of E-photons which is produced via the mode-switching mechanism is several order smaller than the total number of O-photons. Following L88, we consider extraordinary photons isotropically distributed, since their cross section is extremely suppressed for energies well below the cyclotron energy, that for a magnetic field of order of $\sim 10^{14}$ G is about $x_g \sim 11.6$ MeV. The spectrum of E-photons that we are presenting in the Fig. 3.6 has been calculated through the relation (2.73). Since such spectrum belong to photons which were already scattered as O-photons, the spectral shape is basically a small bump at high energies in correspondence with the Comptonized part of the O-photons spectrum. Nonetheless, this cannot be treated like an actual physical information about the radiative transfer of extraordinary photons just because we do not have any other information with respect to the overall number of E-photons, being outside the purpose of this thesis. We can only say that, from the considerations resulting from our calculations, we may reasonably expect that the specific intensity resulting from the solution of the radiative transfer equation for extraordinary photons will give a much higher specific intensity, of the order of the O-photons specific intensity, with a pronounced soft energy peak, because most of them will escape

almost freely from the medium for $x \ll x_g$, due to their small cross section.

4

A Relaxation Method for RTE

The solution of the radiative transfer equation (RTE) describing the modification of a seed photon spectrum due to Comptonization in a plasma is actually a strong mathematical issue. The general equation is an integro-differential equation [4], which, in principle, cannot be analytically solved except under assumptions that are typically very restrictive, such as electron temperature $T_{\rm e} = 0$ [74] or in the energy domain when the emerging spectrum is a power-law [67]. A typical approach in order to transform the equation into a pure differential one [3] is to make the assumption of small photon energy exchange at each scattering process ($\nu^{'} - \nu/\nu \ll 1$), which is commonly known as the Fokker-Planck approximation. This statement holds in the regime of non-relativistic electron temperature ($kT_{\rm e} \lesssim 100$ keV) and sufficiently large optical depth ($\tau \gtrsim 1$).
In this Chapter, we present the general approach to RTE in Fokker-Planck approximation, then we describe a numerical algorithm that can be used with the purpose of finding solutions of such problem.

4.1 Introduction to the RTE problem

The general integro-differential radiative transfer equation [4] for the specific intensity of radiation $I(\nu, \mathbf{\Omega})$ including induced processes, reads as

$$\begin{aligned}\frac{1}{c}\frac{\partial I(\nu,\mathbf{\Omega})}{\partial t} + \mathbf{\Omega}\cdot\nabla I(\nu,\mathbf{\Omega}) = S(\nu)\left[1+\frac{c^2}{2h\nu^3}I(\nu,\mathbf{\Omega})\right] - \sigma_a(\nu)I(\nu,\mathbf{\Omega}) \\ + \int_0^\infty d\nu' \int_{4\pi} d\mathbf{\Omega}' \frac{\nu}{\nu'}\sigma_s(\nu'\to\nu, \mathbf{\Omega}'\cdot\mathbf{\Omega})I(\nu',\mathbf{\Omega}')\left[1+\frac{c^2}{2h\nu^3}I(\nu,\mathbf{\Omega})\right] \\ - \int_0^\infty d\nu' \int_{4\pi} d\mathbf{\Omega}'\sigma_s(\nu'\to\nu, \mathbf{\Omega}\cdot\mathbf{\Omega}')I(\nu,\mathbf{\Omega})\left[1+\frac{c^2}{2h\nu^3}I(\nu',\mathbf{\Omega}')\right],\end{aligned} \tag{4.1}$$

where $S(\nu)$ is a generic source function, σ_a and σ_s are the absorption and scattering coefficients, respectively.
Frequently, there are two basic approximations which are made that we have discussed in Chap. 1. The first is to assume LTE, whenever is possible, and the second is to neglect induced processes, considering the classical RTE (1.11).
In the range of low electron temperatures and large optical depths, the radiation field is almost completely isotropized by scattering and the specific intensity can be written as $I(\nu) = J(\nu) + \nabla \cdot \mathbf{F}(\nu)$, where J and $\mathbf{F}$ are the zero and first moment of the intensity field, respectively. This is the so-called Eddington approximation.
Moreover, we should make a further consideration to be sure that Fokker-Planck approximation holds for our system. We want to consider a plasma which is not simply static, but it can have a dynamical bulk motion with a characteristic velocity $\mathbf{v}(\tau)$. If we want to avail the Fokker-Planck approach, such velocity should be sub-relativistic.
The general form of the RTE in Fokker-Planck approximation for the photon occupation number $n(\nu) = J(\nu)/\nu^3$, where $J(\nu)$ is the angle-averaged specific intensity, with non-relativistic electron plasma in the presence of sub-relativistic bulk motion ($kT_{\rm e} \lesssim 100$ keV and $\mathbf{v}(\tau)/c \ll 1$) was firstly derived by Blandford & Payne ([49], hereafter BP81), and can be written as

$$\frac{\partial n}{\partial t} + \mathbf{v} \cdot \nabla n = \nabla \cdot \left(\frac{1}{3 n_e \sigma(\nu)} \nabla n \right) + \frac{1}{3} (\nabla \cdot \mathbf{v}) \, \nu \frac{\partial n}{\partial \nu} + \frac{1}{\nu^2} \frac{\partial}{\partial \nu} \left[\frac{n_e \sigma(\nu)}{m_e} \nu^4 \left(n + T \frac{\partial n}{\partial \nu} \right) \right] + j \, . \tag{4.2}$$

BP81 found an analytic solution of (4.2) in a limiting case. They assumed that the bulk motion of the electrons greatly exceed their thermal velocity, so they consider the energy transfer by thermal motion negligible. The authors suggested that, when bulk velocity is much larger than thermal velocity, the photons that scatters off electrons, gain energy and give rise to a characteristic power-law spectrum at high energies.
Note also that for $\mathbf{v} = 0$ and $\sigma(\nu) = \sigma_T$, equation (4.2) reduces to the Kompaneets equation for a finite medium [51]. Solutions of this static case, when only thermal effects are considered, can be found in references [60],[66], [61].
Nevertheless the study of the mutual influence of thermal effects and bulk motion on the Comptonization process is fundamental for the understanding of radiative transfer.
Lyubarskii & Sunyaev ([57], hereafter LS82), Colpi [64], Riffert [65] considered both thermal and bulk components studying radiative transfer in the framework of accretion onto a black hole.
Analytical solution of (4.2) was reported by Titarchuk, Mastichiadis & Kylafis ([43], hereafter TMK97) for the case of spherical accretion. The authors showed that these solutions can be found assuming a free-fall velocity profile of the accreting matter ($v_R \propto R^{-1/2}$). In this case, equation (4.2) can be handled with the separation of variable method, which leads to an equation of the form

$$L_x n(x, \tau) + L_\tau n(x, \tau) = -s(x, \tau). \tag{4.3}$$

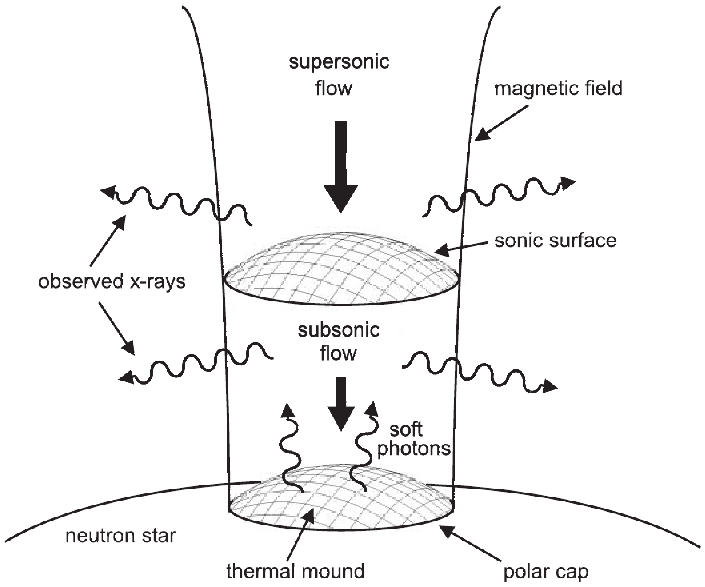

Figure 4.1: *Scheme of a gas accretion column onto the magnetized polar cap of a neutron star proposed by Becker & Wolff [63],[28].*

The solution of equation (4.3) can be written as

$$n(x,\tau) = \sum_{k=1}^{\infty} c_k R_k(\tau) N_k(x), \tag{4.4}$$

where c_k and $R_k(\tau)$ are the expansion coefficients and eigenfunctions of the space operator L_τ, respectively, while $N_k(x)$ is the solution of the differential equation

$$L_x N_k(x) - \gamma_k N_k(x) = -s(x), \tag{4.5}$$

where $\gamma_k \propto \lambda_k^2$ and λ_k^2 is the $\mathrm{k^{th}}$-eigenvalue of the space operator.
TMK97 also pointed out that the Comptonization spectrum obtained by the infinite series (4.4) is dominated at high energies by its first term (i.e., that one correspondent to the first eigenvalue) while the higher terms ($k \geq 2$) contribute to the formation of the soft energy peak.
Starting from the results of TMK97, Farinelli et al. ([55], hereafter F08) developed a model COMPTB for the X-ray spectral fitting package XSPEC which computes the emerging spectrum through the numerical convolution of the Green's function of the energy operator with a blackbody-like seed spectrum. The model has been successfully applied to a sample of sources belonging to the Neutron Star Low-Mass X-ray binary (NS LMXBs) class.

The method of the variable separation has been adopted also by Becker & Wolff ([28], hereafter BW07), to find analytical solutions of the RTE in the case of cylindrical accretion onto the polar cap of a magnetised neutron star (Fig. 4.1).

The starting equation of BW07 is formally the same of BP81: the most significant difference consists in the fact that the Thomson cross-section is replaced by angle-averaged cross sections which takes into account the presence of the magnetic field ($B \sim 10^{12}$ G).
We note that the introduction of such averaged and approximated cross sections allows to maintain the differential nature of equation (4.2) instead of bringing it back to an integro-differential expression like (4.1) or (2.13), even if intrinsically we are still considering the contribution of the magnetic field.
Following the results of LS82, Becker [62],[61], and, later, Becker & Wolff [63] calculated the flow velocity profile

$$v(\tau) = \frac{7}{8} v_c \left\{ 1 - \tanh \left[\frac{7}{2} (\tau - \tau_*) \right] \right\} \tag{4.6}$$

as solution of a second-order nonlinear differential equation derived from the momentum, energy and mass conservation equations, where v_c is the flow velocity at the sonic point ($\tau = 0$) and $\tau_* \equiv (2/7) \tanh^{-1}(1/7) \approx 0.041$. Using the profile (4.6) allows the RTE to be separable in energy and space variable.
In BW07, similarly the authors assumed a velocity profile $v(\tau) \propto -\tau$ with the same purpose. Note that the adopted velocity profile implies that the matter flow stagnates at the stellar surface, contrariwise with the solution of TMK97, where the matter velocity increases towards the central object, which can be either a neutron star or a black-hole. When the velocity profile, however, is not a version of the typical free-fall (TMK97, F08) or $\propto -\tau$ (BW07), the variable separation method can be no longer be applied and the solution of the RTE can be obtained only through numerical methods.
In the next Section we proposed a numerical algorithm which solve RTE in Fokker-Planck approximation for a more general velocity profile for the accreting matter [52].

4.2 Relaxation Method

The algorithm we are proposing is essentially based on the *relaxation method*. Relaxation method takes its name from the idea of convergence from an initial guess to a solution by iterations over a discrete grid of points. In particular, the concept of iteration can be seen as a sort of "time" evolution if, for instance, we express an elliptic partial differential equation (PDE) as a parabolic PDE. If we assume an initial distribution of the unknown function at $t = 0$, then we say that the solution has relaxed to a steady state as $t \to \infty$. Thus, the parabolic PDE reduces to an elliptic PDE when the "time" derivative vanishes at $t \to \infty$.
Remaining within the purpose of this thesis, let's consider, as a general example to explain the method, a linear second-order elliptic PDE [59] with vanishing mixed derivatives and a source term

$$\mathcal{P}(x,y)\frac{\partial^2 u}{\partial x^2} + \mathcal{Q}(x,y)\frac{\partial u}{\partial x} + \mathcal{R}(x,y)u + \mathcal{W}(x,y)\frac{\partial^2 u}{\partial y^2} + \mathcal{Z}(x,y)\frac{\partial u}{\partial y} = -\mathcal{S}(x,y), \tag{4.7}$$

which has, in fact, the general form of the radiative transfer equation in Fokker-Planck approximation. We need to find the function $u(x, y)$ within a certain region $\mathcal{D}$, given the source function $\mathcal{S}(x, y)$ within $\mathcal{D}$, and given the behaviour of $u(x, y)$ at the boundary $\partial\mathcal{D}$. The last condition we have mentioned is necessary in order to fix the boundary conditions. Choosing properly with respect to the specific problem, the boundary conditions can fix the value of the function $u(x, y)$ on $\mathcal{D}$ (*Dirichlet* boundary condition), or the value of its gradient normal to $\partial\mathcal{D}$ (*Neumann* boundary conditions), or a mixture of the two.
We define a three-dimensional grid of discrete points for the variables x, y and t

$$\begin{aligned} x_i &= x_0 + ih_x\,, \quad i = 0, 1, \ldots, N_x, \\ y_j &= y_0 + jh_y\,, \quad j = 0, 1, \ldots, N_y, \\ t_m &= t_0 + mh_t\,, \quad m = 1, 2, \ldots, M, \end{aligned} \tag{4.8}$$

where t is the *fictitious* time we will use to obtain the steady solution of (4.7) at $t \to \infty$ and h_x, h_y, h_t are the grid spacings. The function $u(x, y, t)$ is evaluated at any point of the grid, so we write it as a function of the three indexes, $u_i^{j,m}$. Thus, we write the first and second derivatives over the variables using finite differences:

$$\begin{aligned} \frac{\partial u}{\partial x} &= \frac{u_{i+1}^{j,m} - u_i^{j,m}}{h_x}\,, \quad \frac{\partial^2 u}{\partial x^2} = \frac{u_{i+1}^{j,m} - 2u_i^{j,m} + u_{i-1}^{j,m}}{h_x^2}, \\ \frac{\partial u}{\partial y} &= \frac{u_i^{j+1,m} - u_i^{j,m}}{h_y}\,, \quad \frac{\partial^2 u}{\partial y^2} = \frac{u_i^{j+1,m} - 2u_i^{j,m} + u_i^{j-1,m}}{h_y^2}, \\ \frac{\partial u}{\partial t} &= \frac{u_i^{j,m} - u_i^{j,m-1}}{h_t}. \end{aligned} \tag{4.9}$$

Substituting the above definitions into equation (4.7) and collecting terms, we obtain

$$a_i^j u_{i-1}^{j,m} + b_i^j u_i^{j,m} + c_i^j u_{i+1}^{j,m} + d_i^j u_i^{j-1,m} + e_i^j u_i^{j,m} + f_i^j u_i^{j+1,m} = -S_i^j\,, \tag{4.10}$$

where the coefficients have the general form

$$\begin{aligned} a_i^j &= \frac{\mathcal{P}(x_i, y^j)}{h_x^2}, \\ b_i^j &= -\frac{2\mathcal{P}(x_i, y^j)}{h_x^2} - \frac{\mathcal{Q}(x_i, y^j)}{h_x} + \mathcal{R}(x_i, y^j), \\ c_i^j &= \frac{\mathcal{P}(x_i, y^j)}{h_x^2} + \frac{\mathcal{Q}(x_i, y^j)}{h_x}, \\ d_i^j &= \frac{\mathcal{W}(x_i, y^j)}{h_y^2}, \\ e_i^j &= -\frac{2\mathcal{W}(x_i, y^j)}{h_y^2} + \frac{\mathcal{Z}(x_i, y^j)}{h_y}, \\ f_i^j &= \frac{\mathcal{W}(x_i, y^j)}{h_y^2} - \frac{\mathcal{Z}(x_i, y^j)}{h_y}, \\ S_i^j &= \mathcal{S}(x_i, y^j), \end{aligned} \tag{4.11}$$

that, together with the boundary conditions, can be written in the matrix form

$$\mathbb{A}\cdot \mathbf{u} = \mathbf{S}, \tag{4.12}$$

and can be solved, in theory, directly inverting the matrix $\mathbb{A}$, that represents the action of the differential operator. The matrix $\mathbb{A}$ is called "tridiagonal with fringes" and it is, typically, a sparse matrix. Nevertheless, in the case of (4.7), the nonzero entries of such matrix may not be constants, therefore we need alternative approaches to find the solution without an extremely expensive computational storage.
One of the possible method to handle this problem is the relaxation technique. Basically, we are going to find the solution of (4.10) by generating a series of guesses $u_i^{j,m}$ which starts with an arbitrary configuration $u_i^{j,0}$, and that converges to the solution $u_i^{j,\infty}$ of the linear system (4.12). One possibility to generate such sequence is to imagine that we are not solving (4.7), but rather the time-dependent equation

$$\mathcal{P}(x,y)\frac{\partial^2 u}{\partial x^2} + \mathcal{Q}(x,y)\frac{\partial u}{\partial x} + \mathcal{R}(x,y)u + \mathcal{W}(x,y)\frac{\partial^2 u}{\partial y^2} + \mathcal{Z}(x,y)\frac{\partial u}{\partial y} = \frac{\partial u}{\partial t} - \mathcal{S}(x,y), \tag{4.13}$$

which actually is a parabolic PDE. Iterating for a sufficient number of steps, the initial configuration $u(x,y;0)$ will relax to a time-independent configuration $u(x,y;\infty)$ that satisfies $u_{xx}(x,y;\infty) + u_{yy}(x,y;\infty) + \mathcal{S}(x,y) = 0$, which is, of course, (4.7). Therefore, we need to solve equation (4.13) that in the finite difference representation is the following

$$a_i^j u_{i-1}^{j,m} + b_i^j u_i^{j,m} + c_i^j u_{i+1}^{j,m} + d_i^j u_i^{j-1,m} + e_i^j u_i^{j,m} + f_i^j u_i^{j+1,m} = \frac{(u_i^{j,m} - u_i^{j,m-1})}{h_t} - S_i^j\,. \tag{4.14}$$

Defining the differential operators over the x and y variables as

$$\begin{aligned} \Delta_x &= a_i^j + b_i^j + c_i^j, \\ \Delta_y &= d_i^j + e_i^j + f_i^j, \end{aligned} \tag{4.15}$$

and introducing in the 3D grid intermediate points $m-1/2$ in the fictitious time direction, we are able to split (4.14) into a system of two equations, which is

$$\begin{cases} \Delta_x u^{m-1/2} + \Delta_y u^{m-1} = \dfrac{u^{m-1/2} - u^{m-1}}{h_t} - S\,; \\ \qquad\qquad \Delta_y (u^m - u^{m-1}) = \dfrac{u^m - u^{m-1/2}}{h_t}\,, \end{cases} \tag{4.16}$$

where we have temporarily dropped the indexes i, j for the sake of simplicity. The first equation of (4.16) is basically (4.14) which one that provides us the solution at the intermediate $m-1/2$ layer, given the initial guess function u^{m-1}. At the step $m = 1$, i.e. $t = 0$, we should set the initial arbitrary configuration u^0. Then, the solution u^m of the second equation in (4.16) can be found using both configurations that we already know, u^{m-1} and $u^{m-1/2}$, and it is the solution of

equation (4.10) at $t = t*$. Iterating this procedure for a certain number of steps, u^M relaxes on the actual time-independent solution of (4.10).
The numerical accuracy of the solution can be estimated by combining both equations in the system (4.16), from which we get

$$\Delta_x u^m + \Delta_y u^m + S - \underbrace{h_t \Delta_x \Delta_y \left(u^m - u^{m-1}\right)}_{\text{residuals}} = \frac{u^m - u^{m-1}}{h_t}, \tag{4.17}$$

where the underlined term is the residual error introduced by the application of the relaxation method. As first step in finding solution of the problem, the equations of the system (4.16) can be rearranged by collecting the terms with the same index in both equations (4.16), obtaining

$$\begin{aligned} \left(\Delta_x - \frac{1}{h_t}\right) u^{m-1/2} &= -\left(\Delta_y + \frac{1}{h_t}\right) u^{m-1} - S, \\ \left(\Delta_y - \frac{1}{h_t}\right) u^m &= \Delta_y u^{m-1} - \frac{u^{m-1/2}}{h_t}. \end{aligned} \tag{4.18}$$

Both equations are defined inside a 2D (x, y)-domain, with boundary conditions defined according to the specific problem under consideration. In particular, we need to fix the solution at the (x, y) boundaries for any t and give the initial configuration at $t = 0$, as we have discussed above.
First of all, for any m and j value, we should impose the boundary condition at the left of the x-domain ($i = 0$) for the function $u_0^{j,m-1/2}$, which is

$$u_0^{j,m-1/2} = g_0^j, \tag{4.19}$$

while the source term S_0^j is defined at the beginning. Thus, for $i = 0$, the first equation of system (4.18) can be written as

$$u_0^{j,m-1/2} = \hat{L}_0^j u_1^{j,m-1/2} + \hat{K}_0^j, \tag{4.20}$$

where

$$\begin{aligned} \hat{L}_0^j &= -\frac{c_0^j}{b_0^j - \frac{1}{h_t}}, \qquad \hat{K}_0^j = \frac{\hat{S}_0^{j,m-1}}{b_0^j - \frac{1}{h_t}}, \\ \hat{S}_0^{j,m-1} &= -\left(d_0^j + e_0^j + f_0^j + \frac{1}{h_t}\right) u_0^{j,m-1} - S_0^j. \end{aligned} \tag{4.21}$$

with the coefficients defined in equations (4.11).
At the next step, $i = 1$, using equation (4.20) we obtain

$$\left(a_1^j \hat{L}_0^j + b_1^j - \frac{1}{h_t}\right) u_1^{j,m-1/2} + c_1^j u_2^{j,m-1/2} = \hat{S}_1^{j,m-1} - a_1^j \hat{K}_0^j, \tag{4.22}$$

which can be written as a function of the new coefficients $\hat{L}_i^j$ and $\hat{K}_i^j$ as follows

$$u_1^{j,m-1/2} = \hat{L}_1^j u_2^{j,m-1/2} + \hat{K}_1^j, \tag{4.23}$$

where we have defined

$$\hat{L}_1^j = -\frac{c_1^j}{a_1^j \hat{L}_0^j + b_1^j - \frac{1}{h_t}}\,, \quad \hat{K}_1^j = \frac{\hat{S}_1^{j,m-1} - a_1^j \hat{K}_0^j}{a_1^j \hat{L}_0^j + b_1^j - \frac{1}{h_t}}. \tag{4.24}$$

From this first steps, we derived the general form of the first equation in (4.18) and the coefficients for any iteration of the index i, obtaining

$$u_i^{j,m-1/2} = \hat{L}_i^j u_{i+1}^{j,m-1/2} + \hat{K}_i^j, \tag{4.25}$$

where

$$\hat{L}_i^j = -\frac{c_i^j}{a_i^j \hat{L}_{i-1}^j + b_i^j - \frac{1}{h_t}}\,, \qquad \hat{K}_i^j = \frac{\hat{S}_i^{j,m-1} - a_i^j \hat{K}_{i-1}^j}{a_i^j \hat{L}_{i-1}^j + b_i^j - \frac{1}{h_t}}. \tag{4.26}$$

Then, imposing the second boundary condition at the right boundary of the x-domain ($i = N_x$)

$$u_{N_x}^j = g_{N_x}^j\,, \tag{4.27}$$

and using equation (4.25), we can thus build up the solution over the x-variable iteratively as

$$\begin{aligned}
u_{N_x-1}^{j,m-1/2} &= \hat{L}_{N_x-1}^j\, g_{N_x}^j + \hat{K}_{N_x-1}^j, \\
u_{N_x-2}^{j,m-1/2} &= \hat{L}_{N_x-2}^j\, u_{N_x-1}^{j,m-1/2} + \hat{K}_{N_x-2}^j, \\
&\cdots \qquad\qquad \cdots \\
u_0^{j,m-1/2} &= \hat{L}_0^j\, u_1^{j,m-1/2} + \hat{K}_0^j.
\end{aligned} \tag{4.28}$$

Thus, the construction of the solution is obtained in two steps: a bottom-up process which allows to build the coefficients $\hat{L}_i^j$ and $\hat{K}_i^j$ (Eq. [4.26]) starting from the left boundary condition on u_0^j (Eq. [4.19]), followed by a top-down procedure determined by the right boundary condition $u_{N_x}^j$ (Eq. [4.27]).
Once the solution over the x-variable for the $m - 1/2$ layer is obtained for any j (the index of the y variable), then we may proceed with the solution of the second equation in the system (4.16). The procedure is fundamentally the same that we have described above, hence we should start imposing the initial boundary condition at $j = 0$

$$u_i^{0,m} = \widetilde{L}_i^0 u_i^{1,m} + \widetilde{K}_i^0, \tag{4.29}$$

then, similarly to equation (4.26), we derived the general expressions for the coefficients $\widetilde{L}_i^j$ and $\widetilde{L}_i^j$, which are

$$\widetilde{L}_i^j = -\frac{f_i^j}{d_i^j \widetilde{L}_i^{j-i} + e_i^j + \frac{1}{h_t}}\,, \qquad \widetilde{K}_i^j = -\frac{\widetilde{S}_i^{j,m} - d_i^j \widetilde{K}_i^{j-1}}{d_i^j \widetilde{L}_i^{j-i,m} + e_i^j + \frac{1}{h_t}}, \tag{4.30}$$

where

$$\widetilde{S}_i^{j,m} = \left(d_i^j + e_i^j + f_i^j + \frac{1}{h_t}\right) u_i^{j,m-1} - \frac{u_i^{j,m-1/2}}{h_t} \tag{4.31}$$

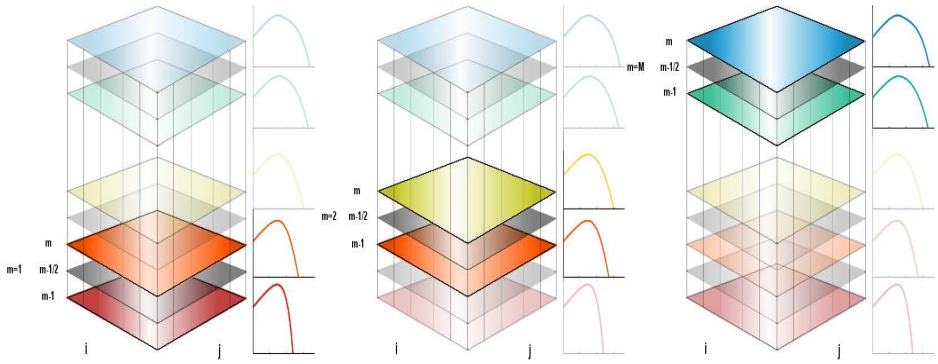

Figure 4.2: *Picture of the iteration scheme. Each plane represents the solution of the system (4.18) at fixed m. The grey planes are those related with the intermediate layers $m - 1/2$. The picture shows the evolution of the solution through the iteration process.*

depends on the solutions $u_i^{j,m-1/2}$ and $u_i^{j,m-1}$ obtained in the layers $m-1/2$ and $m-1$. As required for the procedure over the x-variable, the coefficients $\widetilde{L}_i^j$ and $\widetilde{K}_i^j$ are built from $\widetilde{L}_i^0$ and $\widetilde{K}_i^0$, therefore they are determined by the left boundary conditions ($j = 0$) for the function u_i^0. The solution for any j is determined, given the right boundary condition $u_i^{N_y} = g_i^{N_y}$, by a similar bottom-up iteration:

$$\begin{aligned} u_i^{N_y-1,m} &= \widetilde{L}_i^{N_y-1} u_i^{N_y,m} + \widetilde{K}_i^{N_y-1}, \\ u_i^{N_y-2,m} &= \widetilde{L}_i^{N_y-2} u_i^{N_y-1,m} + \widetilde{K}_i^{N_y-2}, \\ \cdots & \qquad \cdots \\ u_i^{0,m} &= \widetilde{L}_i^0 u_i^{1,m} + \widetilde{K}_i^0. \end{aligned} \tag{4.32}$$

Up to now, we have shown how to build a specific configuration $u_i^{j,m}$ for each x and y and a generic t. Practically, we have found the solution of the system (4.18) for a given value of the index m.
At the first step ($m^* = 1$), we provide, as arbitrary guess at $m = m^* - 1$ ($t = 0$), a source function distribution, thus the solution $u_i^{j,m}$ at $m = m^*$ corresponds to the relaxation of the source function at first iteration. For $m^* \geq 2$, we use the configuration u_i^{j,m^*} as initial guess for the next step, i.e. for seeking solution of the system (4.18) at $m = m^*$, according to the scheme

$$\begin{aligned} & m = 1 \to (u^0, u^{1/2}, u^1), \\ & m = 2 \to (u^1, u^{3/2}, u^2), \\ & \cdots \quad \cdots \quad \cdots, \\ & m = M \to (u^{M-1}, u^{M-1/2}, u^M). \end{aligned} \tag{4.33}$$

The loop over m stops when the some convergence criterion is satisfied, which physically means that the solution has "relaxed" to its stationary value.

The amount of performed iterations is a crucial point. Too much relaxations may lead to numerical instabilities, while too little may slow down convergence. Similarly, a poorly chosen convergence criterion can lead to either poor results (when too loose) or excessive computational times (when too tight).
Therefore, selecting the number of relaxations and the convergence criterion properly can be difficult, but, nonetheless, it is necessary to find the actual solution of the problem within a reasonable amount of computational time. The choice among different convergence criteria depend on the specifics of the problem to be solved and may change during the evolution of the configuration. Unfortunately, there are no universal guidelines for selecting convergence criterion because it depends not only on the physical processes being approximated, but also on the details of the numerical formulation.
For the numerical formulation given here, one possible criterion could be $1-\varepsilon < |u|^{m-1}|/|u|^{m-1/2} < 1+\varepsilon$ and $1-\varepsilon < |u|^{m-1/2}|/|u|^{m} < 1+\varepsilon$, where ε is a user defined numerical tolerance.
In the next Chapter we will show instead the convergence criterion we have chosen to stop the iteration procedure, for the particular case of the RTE in Fokker-Planck approximation in the presence of strong magnetic fields.

5

Application to Cylindrical Accretion Onto Magnetised Objects

In this Chapter we apply the algorithm described in Chap. 4 to obtain the solution of the RTE in Fokker-Planck approximation for accretion towards the polar cap of magnetised neutron star. The mathematical formalism was developed in BW07, in the framework of spectral formation of accretion-powered X-ray pulsars. We slightly modify such formalism and, removing some of the constraints introduced in BW07, we solve the RTE for a more general velocity profile. With the purpose to compare our results with that one given in BW07, we solve the problem also for the velocity profile $v \propto -\tau$.

5.1 Application to the RTE and Boundary Conditions

As we have already pointed out in Chap. 4, the general form of the RTE in the presence of subrelativistic bulk motion of a plasma with constant temperature $T_{\rm e}$ is given by (see Eq.[18] in BP81)

$$\frac{\partial n}{\partial t} + \mathbf{v}\cdot\nabla n = \nabla\cdot\left(\frac{1}{3n_{\rm e}\sigma(\nu)}\nabla n\right) + \frac{1}{3}\left(\nabla\cdot\mathbf{v}\right)\nu\frac{\partial n}{\partial\nu} + \frac{1}{\nu^2}\frac{\partial}{\partial\nu}\left[\frac{n_{\rm e}\sigma(\nu)}{m_{\rm e}}\nu^4\left(n + T_e\frac{\partial n}{\partial\nu}\right)\right] + j(\nu,\mathbf{r}), \tag{5.1}$$

where $n(\nu,\mathbf{r})$ is the zero-moment occupation number of the intensity of the radiation field, $\mathbf{v}$ is the plasma bulk velocity vector, $\sigma(\nu)$ is the electron scattering cross-section, $n_{\rm e}(\mathbf{r})$ is the electron density and $j(\nu,\mathbf{r})$ is the source term. Given that the spectral formation is determined by the optical depth τ of the system,

we use the latter quantity as the actual space variable throughout the change of variable $d\tau = n_e \sigma dz$. The solution of equation (5.1) is fulfilled by imposing as inner boundary condition at the stellar surface ($\tau = 0$, which represents the starting point of the integration domain) for the spectral flux, which is given by

$$\mathbf{F}(\nu, r) = -\nu^3 \left[\left(\frac{1}{3 n_{\rm e} \sigma(\nu)} \nabla n \right) + \frac{1}{3} \mathbf{V} \nu \frac{\partial n}{\partial \nu} \right]. \tag{5.2}$$

Under particular symmetries of the system configuration (e.g., cylindrical or spherical), the problem becomes one-dimensional. For constant electron temperature $T_{\rm e}$ it is also more convenient to use the dimensionless variable $x \equiv h\nu / kT_{\rm e}$; moreover, when performing numerical integration using finite-difference methods, we use a logarithmic binning of the energy through the additional change of variable $x \to e^q$. Under these assumptions, equation (5.2) becomes

$$F(q, \tau) = -\left[\frac{1}{3} \frac{\partial J}{\partial \tau} + \frac{1}{3} v \left(\frac{\partial J}{\partial q} - J \right) \right], \tag{5.3}$$

where $J \equiv n\, x^3$ is the specific intensity.
At the inner boundary we impose the condition

$$F(q, 0) = -\frac{1}{2} \left(\frac{1 - A}{1 + A} \right) J, \tag{5.4}$$

where A is the albedo at the surface. A fully absorptive surface ($A = 0$) is appropriate for a black hole, while $0 < A \leq 1$ accounts, e.g., for a neutron star atmosphere. However, the inner boundary condition (5.4) depends on energy as well as space (see Eqs. [5.2] and [5.3]). For mixed boundary value problems, no analytical solutions are possible (see Appendix E in TMK97) and numerical methods may lead to unstable solutions. We propose a phenomenological approximation which allows to avoid this issue. As previously noted by TMK97, the spectrum can be modelled with a power-law in a properly chosen energy interval, when we are in the case of unsaturated Comptonization. In this range, the specific intensity can be written as $J(x, \tau) = R(\tau) x^{-\alpha}$, thus substituting this relation into equation (5.4), we find

$$-\frac{dR}{d\tau} + \beta_0 (\alpha + 3) R = -\frac{3}{2} \left(\frac{1 - A}{1 + A} \right) R, \tag{5.5}$$

where β_0 is the bulk velocity at the inner radius ($\tau = 0$). It is worth noticing that the boundary condition (5.5) depends exclusively on the space variable τ and on the power-law index α.
Writing the derivative in terms of finite-difference at $j = 0$ (i.e., $\tau = 0$), equation (5.5) then becomes

$$-\frac{u_i^1 - u_i^0}{h_\tau} + \beta_0 (\alpha + 3) u_i^0 = -\frac{3}{2} \left(\frac{1 - A}{1 + A} \right) u_i^0. \tag{5.6}$$

After collecting terms, we obtain the inner boundary condition in the form

$$u_i^0 = \frac{1}{1 + h_\tau [\beta_0 (\alpha + 3) + G(A)]} u_i^1, \tag{5.7}$$

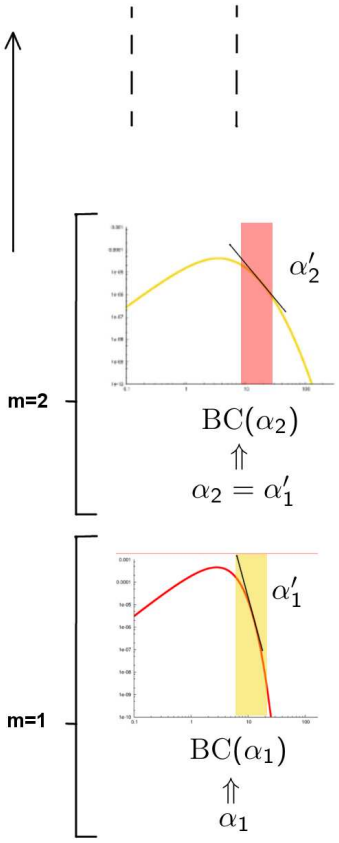

Figure 5.1: *Iteration scheme describing the determination of the spectral index α_m for each m step. At first step, the spectral index α_1 is given as initial guess. Then, it used in the calculation of the boundary condition (BC) (5.7). When the emerging spectrum has been found, we estimate its spectral index α_1' which becomes the index used in the calculation of the BC at the next step.*

where we have defined the quantity $G(A) = 3/2(1-A)/(1+A)$. Following the procedure described in Chap. 4, equation (5.7) provides the definition of the coefficients $\widetilde{L}_i^0$ and $\widetilde{K}_i^0$ (4.30) as

$$\widetilde{L}_i^0 = \frac{1}{1 + h_\tau[\beta_0(\alpha+3) + G(A)]}, \qquad \widetilde{K}_i^0 = 0. \tag{5.8}$$

As outer boundary condition over τ, we impose that $u_i^{N_y} = 0$, which means that the specific intensity goes to zero for $\tau \to \tau_{\max}$.
Concerning the energy variable $x = h\nu/kT_e$, we impose that the solution u_i^j, which, in the framework of RTE, physically represents a specific intensity, it must

be, by definition, approach zero in the limits $h\nu \to 0$ and $h\nu \to \infty$, therefore we set $u_0^j = u_{N_x}^j = 0$ (see Eqs. [4.19] and [4.27]).
We emphasise that the general condition $u_i^j > 0$ for any (i, j)-value implies a specific restriction in the choice of the step size h_τ, which ensures that $\widetilde{L}_i^0 > 0$ (as $\beta_0 \leq 0$). More specifically, we imposed this condition on h_τ such that the number of steps over τ be $N_\tau = \tau_{\max}/h_\tau \geq 10$.

5.1.1 Convergence Criterion

As we have already mentioned in Chap. 4, the choice of a proper convergence criterion is a fundamental step for seeking the actual solution of the equation we are dealing with. Considering the boundary condition (5.7), we note that at each iteration m, the power-law index α_m of the configuration $u_i^{0,m}$ (corresponding to $\tau = 0$) is calculated, in a given energy range $E_{\min} - E_{\max}$. In order to minimise bias or wrong estimates of α_m, the definition of the energy interval for the computation of the spectral slope must be chosen carefully. If the seed photon spectrum is a blackbody with temperature $kT_{\rm bb}$, a reasonable choice can be the assumption $E_{\min} \approx 7\,kT_{\rm bb}$ and $E_{\max} \approx 20\,kT_{\rm bb}$, respectively, given that this interval is above the major contribution of the blackbody component and below the expected high-energy cut-off value.
At the first iteration ($m = 1$), we set an initial guess for the spectral index, which will be provided to the boundary condition (5.7). Fulfilling this condition, we extrapolate the specific intensity at $m = 1$ and we calculate the spectral index that will be used in the boundary condition at the next iteration. Repeating this scheme for each m step, we expect to see that the solution $u_i^{j,m}$ should relaxes into the final configuration satisfying the initial equation.
We stop the iteration process when α_m and α_{m+1} differ less than 10^{-5} provided that the condition holds for a sufficiently high number of iterations (> 100). Note that the same criterion is adopted also if $\beta_0 = 0$, even if, of course, $\widetilde{L}_i^0$ remains constant across the iteration. We have also verified that this criterion automatically satisfies the convergence of the norms $|u|^{m-1}$, $|u|^{m-1/2}$, and $|u|^m$.

5.2 Cylindrical accretion onto a magnetised neutron star

We applied our algorithm to solve the problem of radiative transfer in the scenario of matter accretion towards the polar cap of a magnetised neutron star, whose mathematical formalism was developed by BW07 in the framework of the spectral formation of accretion-powered X-ray pulsars.
As we described in Chap. 2, the strong magnetic field ($B \gtrsim 10^{12}$G) of the neutron star is expected to channel the accretion flow towards the polar caps, and for small values of the altitude of the accretion column above the stellar surface, the problem can be treated in a axis-symmetric approximation where the space variable is defined by the vertical coordinate Z. The medium, subjected

to the effect of the magnetic field, becomes birefringent entailing the formation of two linear polarisation modes (ordinary and extraordinary) of the radiation, each having a characteristic scattering cross-section. For energy below the first cyclotron harmonic at $E_{\rm c} \approx 11.57\ B_{12}$ keV (where $B_{12} \equiv B/10^{12}$ G), BW07 defined angle-and energy-averaged cross-sections parallel and perpendicular to the magnetic field lines as $\sigma_{\parallel} = 10^{-3}\sigma_{\rm T}$ and $\sigma_{\perp} = \sigma_{\rm T}$, respectively, where $\sigma_{\rm T}$ is the Thomson scattering cross-section. Such approximation allows to handle the problem, both analytically and numerically. Indeed, averaging the cross-section over the angle, smears out anisotropy effects and makes applicable the Fokker Planck approximation.

A full angle-dependent treatment of the radiative transfer problem can be faced only through the use of MonteCarlo techniques. For instance, Nobili et al. ([[41]], hereafter NTZ08), developed a 3D Monte Carlo code for a twisted magnetospheric model with resonant Compton scattering (RCS) assuming that isotropic and unpolarised blackbody photons are emitted at the neutron star surface. Such photons are then Comptonized by a Maxwellian population of electrons which moves in 1D dimension across the field lines, subjected to a global bulk motion. In order to avoid complications introduced by Quantum Electrodinamic (QED) effects in the scattering cross section, NTZ08 generated a grid of spectra for different sets of the model parameters only up to 15 keV. NTZ08 successfully applied their model to a sample of highly magnetised compact objects, namely AXPs and SGRs, observed by *XMM* and *INTEGRAL*. On the other hand, we note that Ferrigno et al. [56], starting from the analytical solutions reported in BW07, developed a model that was later almost successfully tested on the accreting pulsar 4U 0115+63. Their model is based essentially on the convolution of the column-integrated Green's function of the thermal plus bulk scattering operator with a given seed photon distribution. The basic assumption of this derivation is that the velocity profile of the accreting matter is assumed to be $v(\tau) \propto -\tau$, which allows one to find analytical solutions through the variable separation method (Eqs. [36] and [37] in BW07).

The numerical algorithm we developed directly solves the RTE in Fokker-Planck approximation, without the need of this prescription for the dynamical configuration of the accreting matter field. Specifically, we included some modifications with respect to the approach of BW07 and Ferrigno et al.[56]. First, following TMK97, we include in equation (5.1) a second term in the thermal Comptonization operator that accounts for the contribution of the bulk motion velocity of electrons in addition to their thermal (Maxwellian) component. Besides, we consider the time-independent version of (5.1), in order to apply correctly the algorithm described in Chap. 4. With this prescription in mind, equation (5.1) becomes

$$
\begin{aligned}
-\mathcal{S}(\epsilon, Z) = &-\frac{v}{c}\frac{\partial n}{\partial Z} + \frac{dv}{dZ}\frac{\epsilon}{3c}\frac{\partial n}{\partial \epsilon} + \frac{\partial}{\partial Z}\left(\frac{1}{3n_{\rm e}\sigma_{\parallel}}\frac{\partial n}{\partial Z}\right) \\
&- \frac{n}{ct_{\rm esc}} + \frac{n_{\rm e}\overline{\sigma}}{m_{\rm e}c^2}\frac{1}{\epsilon^2}\frac{\partial}{\partial \epsilon}\left\{\epsilon^4\left[n + \left(kT_{\rm e} + \frac{1}{3}m_{\rm e}v^2\right)\frac{\partial n}{\partial \epsilon}\right]\right\}, \qquad (5.9)
\end{aligned}
$$

where $\epsilon \equiv h\nu$, $\overline{\sigma} = 10^{-1}\sigma_{\rm T}$, while $t_{\rm esc}$ is the photon mean escape timescale (see Eq. [17] in BW07)

$$t_{\rm esc} = \frac{n_{\rm e}\sigma_{\perp} r_0^2}{c}. \tag{5.10}$$

Now, defining the optical depth as $d\tau = n_{\rm e}\sigma_{\parallel} dZ$ and introducing the dimensionless energy $x \equiv h\nu/kT_{\rm e}$, (5.9) becomes

$$\begin{aligned} -\frac{\sigma_{\parallel}}{\overline{\sigma}}\mathcal{S}(x,\tau) = &-\frac{\sigma_{\parallel}}{\overline{\sigma}}\frac{v}{c}\frac{\partial n}{\partial \tau} + \frac{\sigma_{\parallel}}{\overline{\sigma}}\frac{1}{c}\frac{dv}{d\tau}\frac{x}{3}\frac{\partial n}{\partial x} + \frac{1}{3}\frac{\sigma_{\parallel}}{\overline{\sigma}}\frac{\partial^2 n}{\partial \tau^2} - \left(\frac{\xi v}{c}\right)^2 \frac{\sigma_{\parallel}}{\overline{\sigma}} n \\ &+ \frac{kT_e}{m_e c^2}\frac{1}{x^2}\frac{\partial}{\partial x}\left\{x^4\left[n + \left(1 + \frac{1}{3}\frac{m_e v^2}{kT_e}\right)\frac{\partial n}{\partial x}\right]\right\} \end{aligned} \tag{5.11}$$

where we have divided all the equation by $\overline{\sigma}/\sigma_{\parallel}$ and we have introduced the dimensionless parameter ξ given by (see Eq. [26] in BW07)

$$\xi = \frac{15.8\, r_0}{\dot{m}}. \tag{5.12}$$

Looking at equation (5.11), we see that, in the escape time prescription provided by BW07, the spatial diffusion of photons is described by

$$\frac{1}{3}\frac{\sigma_{\parallel}}{\overline{\sigma}}\frac{\partial^2 n}{\partial \tau_{\parallel}^2} - \left(\frac{\xi v}{c}\right)^2 \frac{n}{\sigma_{\rm R}} = \lambda^2 n, \tag{5.13}$$

or, more clearly, by

$$\frac{1}{3}\frac{\sigma_{\parallel}}{\overline{\sigma}}\frac{\partial^2 n}{\partial \tau_{\parallel}^2} - \frac{n}{r_0 n_e \overline{\sigma}\tau_{\perp}} = \lambda^2 n, \tag{5.14}$$

where $d\tau_{\parallel} = n_e\sigma_{\parallel} dZ$ is the optical depth along the Z-axis and $d\tau_{\perp} = n_e\sigma_{\perp} dr$ is the optical depth along the r-axis, perpendicular to the magnetic field, and λ is the eigenvalue. The right hand side of equation (5.14) can be approximated as

$$\left[\frac{1}{3\tau_{\parallel}^2}\frac{\sigma_{\parallel}}{\overline{\sigma}} - \frac{1}{r_0 n_e \overline{\sigma}\tau_{\perp}}\right] n \approx \lambda^2 n \tag{5.15}$$

and, as we know from Chap. 2 and 3, since the eigenvalue $\lambda^2 < 1$, also both the coefficients on the right hand side of (5.15) should be less than 1, simultaneously, in order for diffusion approximation to hold. In particular, the coefficient $\mathcal{D}_{\parallel} = \sigma_{\parallel}/(3\overline{\sigma}\tau_{\parallel}^2)$ takes into account the spatial diffusion of photons propagating along the magnetic field lines, while the coefficient $\mathcal{D}_{\perp} = 1/(r_0 n_e \overline{\sigma}\tau_{\perp})$ accounts for the diffusion of photon travelling perpendicular to the field.
Following the approach of BW07, since $\tau_{\parallel} \ll \tau_{\perp}$ thus $\mathcal{D}_{\parallel} \gg \mathcal{D}_{\perp}$, which means that, the spatial diffusion in the perpendicular direction (r-axis) is more efficient than along the Z-axis, therefore photons travelling at large angles to the field lines have a smaller diffusion escape probability, i.e. a smaller coefficient $\mathcal{D}_{\perp}$. As result, the authors focused their attention on the diffusion of those photons propagating along magnetic field lines, approximating a proper treatment of the diffusion in the perpendicular direction (i.e. the solution of integral equation

(2.23)) with the coefficient $\mathcal{D}_\perp$.
Having these considerations in mind, we go ahead with our calculations. Introducing a logarithmic binning of the dimensionless energy, the stationary version of equation (5.9) for the mean specific intensity $J(q,\tau)$ becomes

$$-\frac{\mathcal{S}(q,\tau)}{H} = \left[1+\frac{m_{\rm e}v(\tau)^2}{3kT_{\rm e}}\right]\frac{\partial^2 J}{\partial q^2} + \left[\frac{3kT_{\rm e}(e^q-3+\hat{\delta})-m_{\rm e}v(\tau)^2}{3kT_{\rm e}}\right]\frac{\partial J}{\partial q} + \left[e^q-3\hat{\delta}-\frac{\xi^2 v(\tau)^2}{Hc^2}\right]J + \frac{1}{3H}\frac{\partial^2 J}{\partial \tau^2} - \frac{v(\tau)}{Hc}\frac{\partial J}{\partial \tau}, \tag{5.16}$$

where we have defined the quantities

$$H = \frac{\overline{\sigma}}{\sigma_\parallel}\frac{kT_{\rm e}}{m_{\rm e}c^2}, \tag{5.17}$$

and

$$\hat{\delta} = \frac{1}{3H}\frac{d\beta(\tau)}{d\tau}, \tag{5.18}$$

in which $\beta(\tau) = v(\tau)/c$. Equation (5.16) is given in the general form (4.7) and for this particular case, we find that the coefficients are

$$\begin{aligned}
\mathcal{P}(\tau) &= 1+\frac{m_{\rm e}v(\tau)^2}{3kT_{\rm e}},\\
\mathcal{Q}(\tau) &= \frac{3kT_{\rm e}(e^q-3+\hat{\delta})-m_{\rm e}v(\tau)^2}{3kT_{\rm e}},\\
\mathcal{R}(\tau) &= e^q-3\hat{\delta}-\frac{\xi^2 v(\tau)^2}{Hc^2},\\
\mathcal{W}(\tau) &= \frac{1}{3H},\\
\mathcal{Z}(\tau) &= -\frac{v(\tau)}{Hc},\\
\hat{\mathcal{S}}(q,\tau) &= \frac{\mathcal{S}(q,\tau)}{H}.
\end{aligned} \tag{5.19}$$

To solve equation (5.16), it is necessary to define the behaviour of the velocity profile $\beta(\tau)$. We considered two possibilities: the first one is to assume a generic profile

$$\beta(Z) = -\mathscr{A}(Z_s/Z)^{-\eta}, \tag{5.20}$$

where the normalization constant is defined as $\mathscr{A} = \beta_0(Z_0/Z_s)^\eta$, and β_0 is the terminal velocity at the stellar surface Z_0.
The continuity equation for the system under investigation gives the electron number density

$$n_{\rm e} = \frac{\dot{M}}{\pi m_p|\beta(Z)|cR_0^2}, \tag{5.21}$$

where $\dot{m} \equiv \dot{M}/\dot{M}_{\rm E}$ is the mass accretion rate in Eddington units and R_0 is the radius of the accretion column.
We then define the dimensionless quantities z and r_0 through the change of

variables $Z \rightarrow R_{S\odot} m z$ and $R_0 \rightarrow R_{S\odot} m r_0$, where $m \equiv M/M_\odot$, while $M_{S\odot}$ and $R_{S\odot}$ are the Sun mass and Schwarzschild radius, respectively. The effective vertical optical depth of the accretion column is then given by

$$\tau(z) = \int_{z_0}^{z} n_e \sigma_\parallel dZ' = C \frac{\dot{m}}{\mathscr{A} {r_0}^2} \frac{\left(z^{\eta+1} - z_0^{\eta+1}\right)}{\eta + 1}, \tag{5.22}$$

where $C = 2.2 \times 10^{-3}$, and z_0 is the vertical coordinate at the neutron star surface. Inverting relation (5.22), we also define the velocity profile of the accreting matter as a function of the optical depth τ instead of the space variable z

$$\beta(\tau) = -\mathscr{A} \left\{ z_0^{\eta+1} + \frac{\mathscr{A} r_0^2 (1+\eta)\tau}{C\dot{m}} \right\}^{-\frac{\eta}{\eta+1}}. \tag{5.23}$$

As a second possibility, following BW07, we considered the velocity profile

$$\beta(\tau) = -\Psi\tau, \tag{5.24}$$

where $\Psi = 0.67\xi/z_0$ (see Eq. [32] in BW07).
Since the optical depth τ represents one of the free parameters of our model, once we provide the dimensionless accretion column radius r_0, the accretion rate is determined inverting equation (5.22), if $\beta(\tau)$ is defined as in equation (5.23), or from equation (28) in BW07 if $\beta(\tau)$ belongs to equation (5.24). This step is necessary to determine the ξ parameter (Eq. [5.12]), and requires fixing the maximum altitude of the accretion column $z_{\max}$. We assumed $z_{\max} = 2z_0$, and all emerging spectra that we will present in the next Chapter were computed with this choice.

6

Examples of Emerging Spectra

In this Chapter we report some examples of the theoretical spectra obtained by the application of our model, described in Chap. 4, 5, to equation (5.16). We discuss the spectral shapes we obtain for different sets of the physical quantities which define the system.

6.1 Results

We consider a blackbody seed photon spectrum at given temperature $kT_{\rm bb}$ with exponential spatial distribution across the vertical direction, according to

$$S(x,\tau) = C_{\rm n} e^{-\tau} \frac{kT_{\rm e}^3 x^3}{e^{kT_{\rm e}/kT_{\rm bb}\ x} - 1}, \tag{6.1}$$

with the normalization constant defined as $C_{\rm n} = R_{\rm km}^2/D_{10}^2$, where $R_{\rm km}$ and D_{10} are the blackbody emitting area in kilometres and the source distance in units of 10 kpc, respectively. The spectra were computed using the velocity profiles defined in equations (5.23) and (5.24), respectively. The common parameters for both cases are consequently the blackbody temperature $kT_{\rm bb}$, the electron temperature $kT_{\rm e}$, the optical depth τ, the albedo at the inner surface A and the radius of the accreting column r_0. On the other hand, for $\beta(\tau)$ belonging to equation (5.23), additional parameters are the index η and the terminal velocity at the star surface β_0. We first present the results for this second physical case. In Fig. 6.1 we show the emerging spectra for different values of the electron temperature $kT_{\rm e}$ and two terminal velocities $\beta_0 = 0.1$ and $\beta_0 = 0.64$. As expected, both times higher values of $kT_{\rm e}$ produce flatter spectra and push the cut-off energy $E_{\rm c}$ to higher energies; on the other hand, the bulk contribution as a second channel of Comptonization depends on the value of $kT_{\rm e}$. The two extreme temperature values reported here, $kT_{\rm e} = 5$ keV and $kT_{\rm e} = 50$ keV, are particularly instructive: for low electron temperatures the spectrum changes from blackbody-like when $\beta_0 = 0.1$ to a cut-off power law with $E_{\rm c} \gtrsim 30$ keV when $\beta_0 = 0.64$, while the

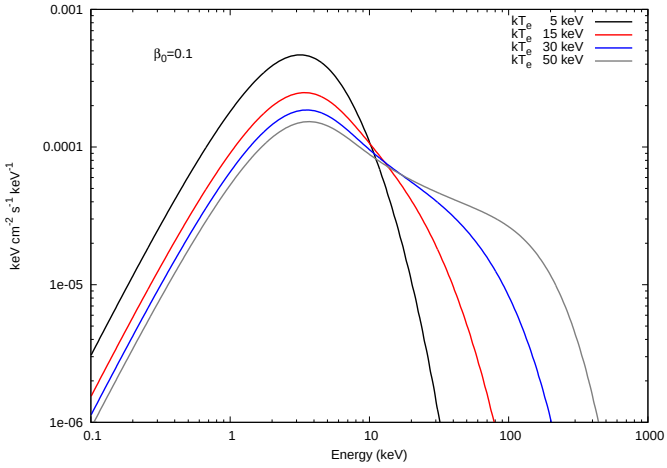

(a)

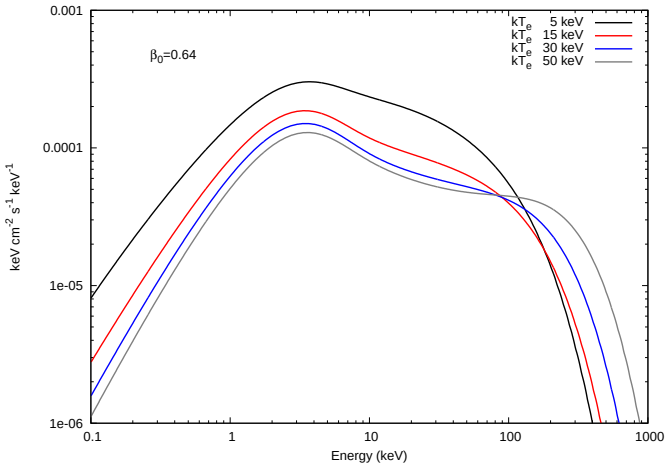

(b)

Figure 6.1: *Emerging spectra obtained from the solution of equation (5.16) for different values of the electron temperature kT_e, with the velocity profile of equation (5.23). In both cases the fixed parameters are $kT_{bb} = 1$ keV, $\tau = 0.2$, $\eta = 0.5$, $r_0 = 0.25$, $A = 1$.*
Panel (a)*: $\beta_0 = 0.1$, Panel* (b)*: $\beta_0 = 0.64$.*

spectral change is much less enhanced for a hot plasma. These can be considered as typical examples of bulk-dominated and thermal-dominated Comptonization spectra, respectively. Together with the electron temperature, the optical depth τ is an important parameter that plays a key role in determining the spectral slope and cut-off energy, as clearly shown in Fig. 6.2. We note that in Fig. 6.1 and Fig. 6.2 the index of the velocity profile was chosen to be $\eta = 0.5$, typical

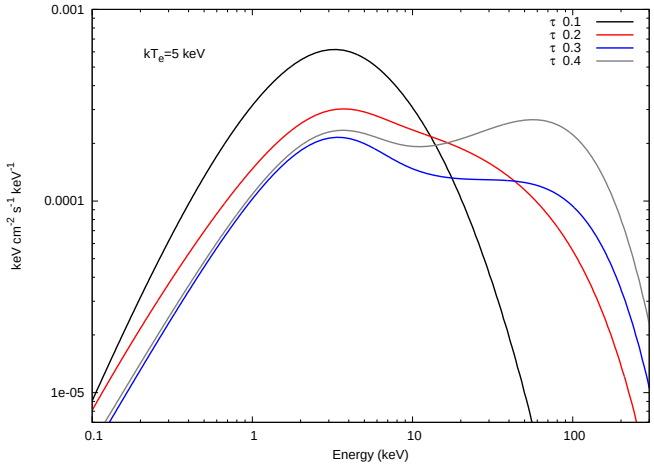

(a)

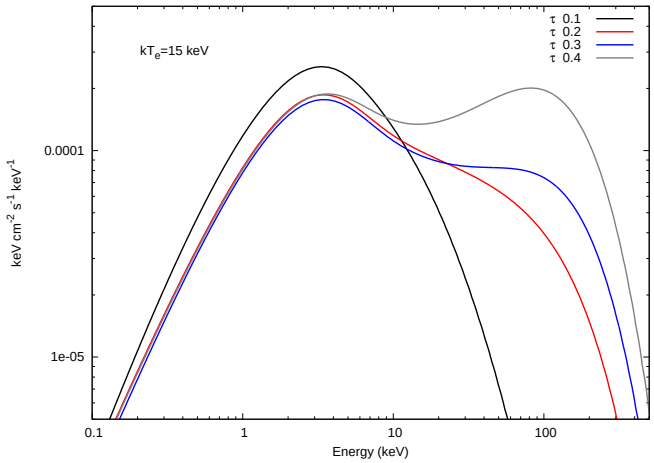

(b)

Figure 6.2: *Same as Fig. 6.1 but for different values of the optical depth τ, with the velocity profile of equation (5.23). Fixed parameters are $kT_{\rm bb} = 1$, $r_0 = 0.25$, $\eta = 0.5$, $\beta_0 = 0.64$, $A = 1$. Panel (a): $kT_{\rm e} = 5$ keV, Panel (b): $kT_{\rm e} = 15$ keV.*

of accretion onto a compact object where gravity and radiation pressure are the only force terms that determine the dynamical configuration. Here, the terminal value of the matter velocity β_0 depends on the ratio of the radiative and gravitational forces, provided the condition $|\mathbf{F}_{\rm r}|/|\mathbf{F}_{\rm g}| \lesssim 1$ is satisfied. This relatively simple approach is valid for low values of optical depth τ, while when $\tau > 1$ radiative transfer becomes important, the problem requires in principle a more accurate radiation-hydrodynamics treatment. It is outside the scope of

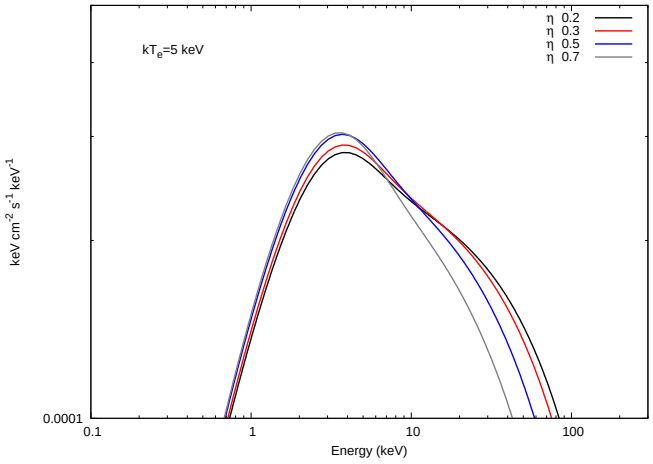

(a)

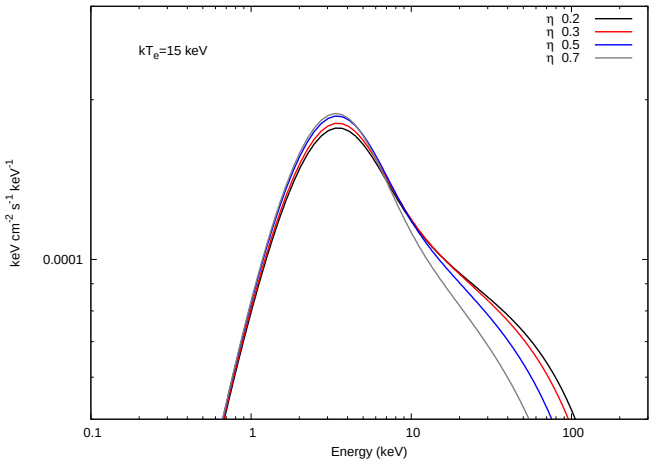

(b)

Figure 6.3: *Same as Fig. 6.1 but for different values of the index of the velocity profile η (see Eq. 5.23). Fixed parameters are $kT_{\rm bb} = 1$, $\tau = 0.2$, $\beta_0 = 0.64$, $r_0 = 0.25$, $A = 1$. Panel (a): $kT_{\rm e} = 5$ keV, Panel (b): $kT_{\rm e} = 15$ keV.*

this paper to compute the exact velocity profile for accreting matter under the presence of a strong radiation field in a high optical depth environment. We merely introduced a simple parametrisation for modifying the velocity field by changing the index η, with the results shown in Fig. 6.3, for two different values of the electron temperature $kT_{\rm e}$. As Fig. 6.3 shows, the lower the value of η, the harder the spectrum: this behaviour can be explained in a quantitative and a qualitative way. Indeed, as η increases, the velocity profile $\beta(z)$ becomes sharper, and for a fixed terminal velocity β_0, electron temperature $kT_{\rm e}$, and optical depth

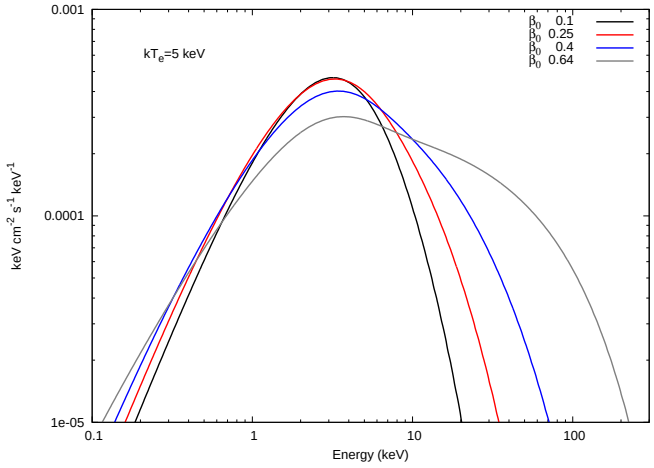

(a)

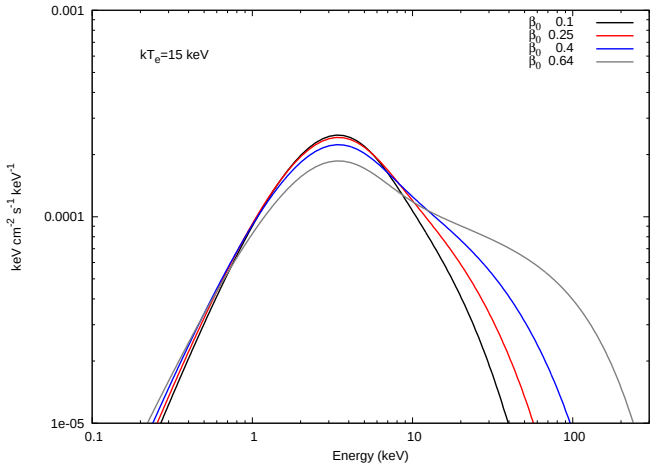

(b)

Figure 6.4: *Same as Fig. 6.1 but for different values of the inner velocity β_0 for the velocity profile of equation (5.23). Fixed parameters are $kT_{\rm bb} = 1$, $\tau = 0.2$, $\eta = 0.5$, $r_0 = 0.25$, $A = 1$.*
Panel (a)*: $kT_{\rm e} = 5$ keV, Panel* (b)*: $kT_{\rm e} = 15$ keV.*

τ, while photons diffuse through the bounded medium, on average the energy of the electrons (caused by their Maxwellian plus bulk motion) will be lower, and consequently the net energy gain of the photons due to inverse Compton will be less. From the mathematical point of view, it is worth mentioning that Mastichiadis & Kylafis ([68], hereafter MK92) reported the analytical solution of the RTE in the Fokker-Planck approximation with the variable separation method for spherical accretion without magnetic field in the limit $T_{\rm e} = 0$. Assuming a

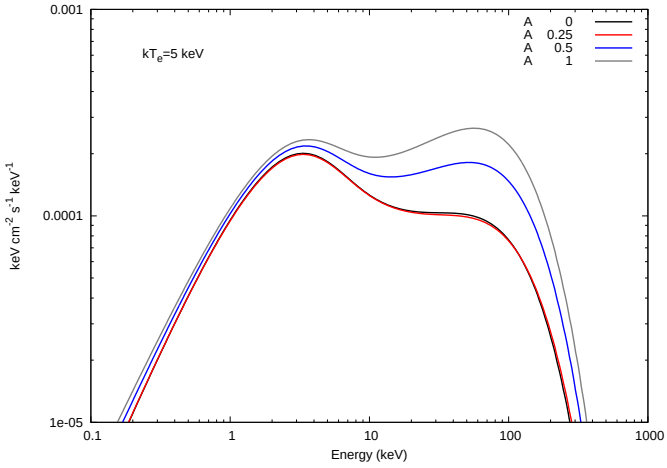

(a)

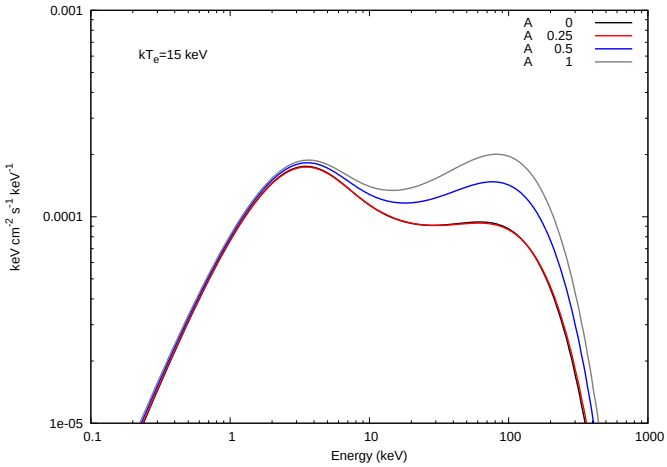

(b)

Figure 6.5: *Same as Fig. 6.1 but for different values of the albedo A, with the velocity profile of equation (5.23). Fixed parameters are* $kT_{\rm bb} = 1$, $\tau = 0.4$, $\eta = 0.5$, $\beta_0 = 0.64$, $r_0 = 0.25$.
Panel (a) $kT_{\rm e} = 5$ *keV, Panel* (b)*:* $kT_{\rm e} = 15$ *keV.*

general velocity profile $\beta_{\rm r} \propto r^{-\eta}$, the authors showed that the spectral index of the $k^{\rm th}$-Comptonization order emerging spectrum yields $\alpha_{\rm k} = 3+3\lambda_{\rm k}/(2-\eta)$ (see Eq. [4.4]), where $\lambda_{\rm k}$ is the $k^{\rm th}$-eigenvalue of the space operator. Using equation (B12) of MK92, it follows immediately that as η increases, the spectral index $\alpha_{\rm k}$ increases as well. This mathematical result in terms of spectral formation can be considered as general in the framework of the Fokker-Planck treatment, and is accordingly qualitatively meaningful for our research. We also emphasise that

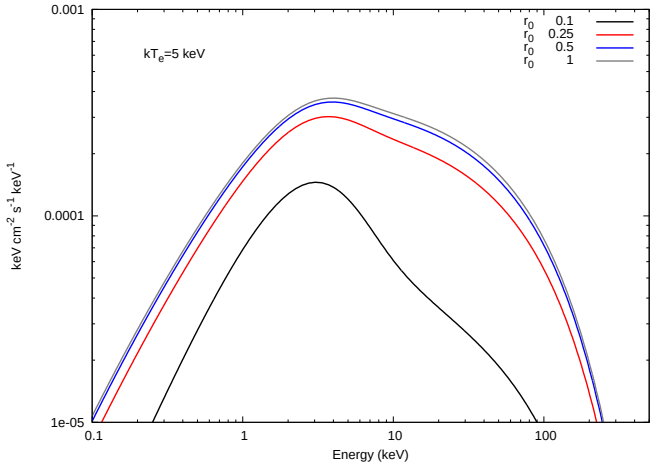

(a)

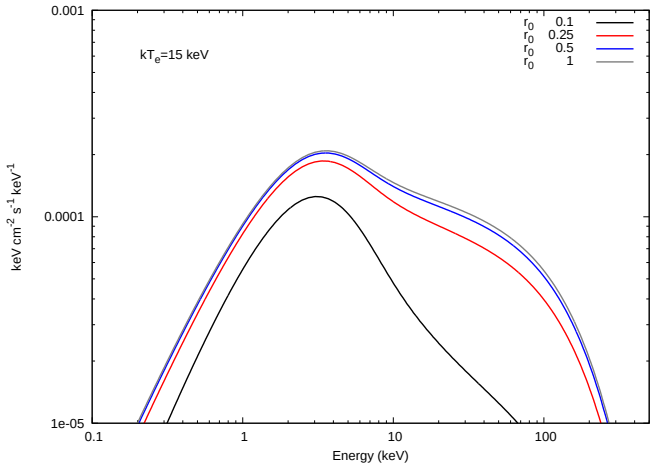

(b)

Figure 6.6: *Same as Fig. 6.1 but for different values of the accretion column radius r_0, with the velocity profile of equation (5.23). Fixed parameters are $kT_{\rm bb} = 1$, $\tau = 0.2$, $\eta = 0.5$, $\beta_0 = 0.64$, $A = 1$.*
Panel (a): $kT_{\rm e} = 5$ keV, Panel (b): $kT_{\rm e} = 15$ keV.

analytical solutions for $\eta \neq 0.5$ have been possible for MK92 only because of the condition $T_{\rm e} = 0$, which drops the thermal Comptonization operator in the RTE, while when $T_{\rm e} > 0$ this is possible only for $\eta = 0.5$ (TMK97, F08). In Fig. 6.4 we show results for different terminal bulk velocities β_0 for two electron temperature values. The figure can be considered an extension and completion of Fig. 6.1 because more values of β_0 are shown to better appreciate the induced changes in the emerging spectra. The spectral modifications as a result of dif-

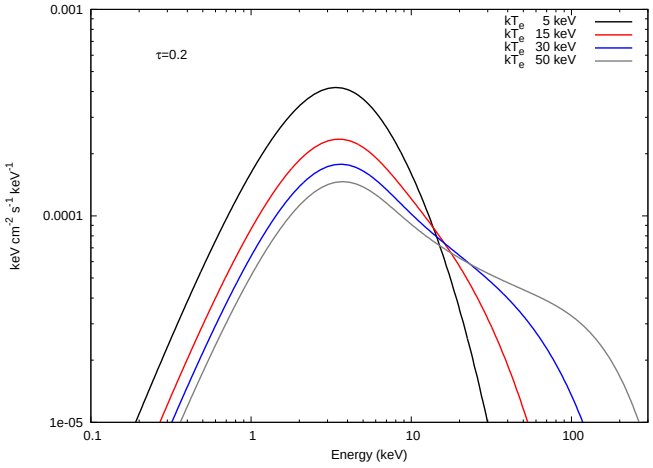

(a)

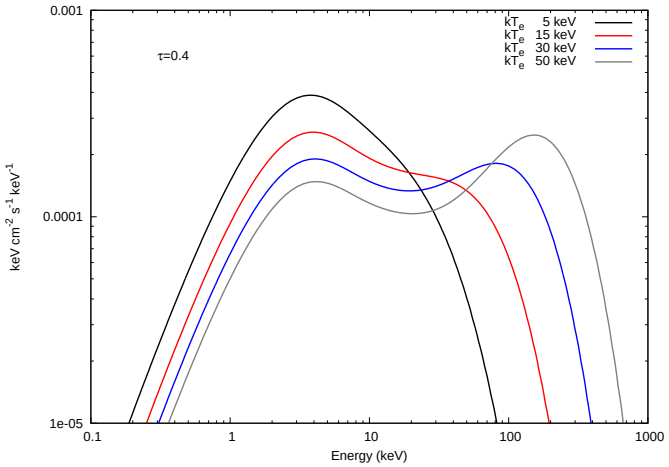

(b)

Figure 6.7: *Emerging spectra obtained from the solution of equation (5.16) for different values of the electron temperature $kT_{\rm e}$, with the velocity profile of equation (5.24). In both cases the fixed parameters are $kT_{\rm bb} = 1$ keV, $\tau = 0.2$, $\beta_0 = 0.64$, $r_0 = 0.25$, $A = 1$.*
Panel (a)*: $\tau = 0.2$, Panel* (b)*: $\tau = 0.4$.*

ferent values of the albedo A at the inner surface are instead shown in Fig. 6.5, where we explored full absorption ($A = 0$) and full reflection ($A = 1$), together with other intermediate values. From the point of view of a physical link to astrophysical objects it would be natural to associate a black hole to the condition $A = 0$ and a neutron star to the condition $A = 1$, as was respectively suggested by Titarchuk & Fiorito [54] and Farinelli & Titarchuk [53], even though this

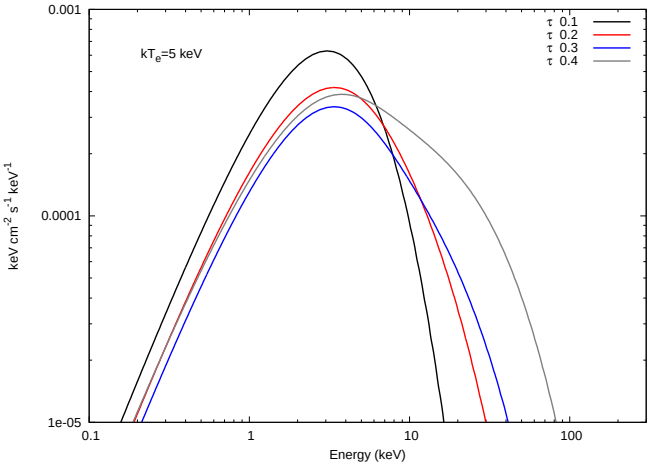

(a)

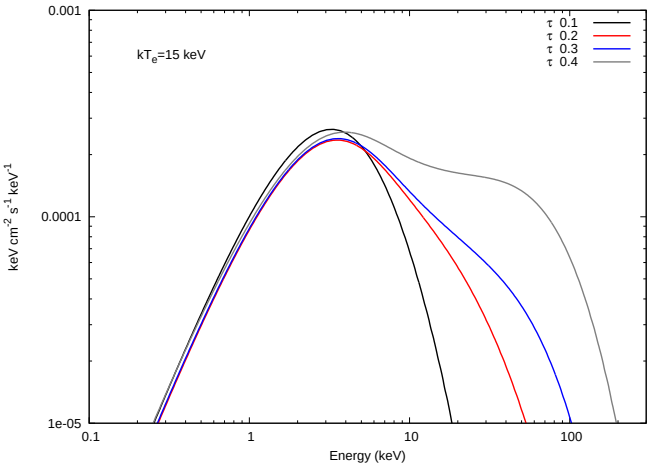

(b)

Figure 6.8: *Same as Fig. 6.1 but for different values of the optical depth τ, with the velocity profile of equation (5.24). Fixed parameters are $kT_{\rm bb} = 1$, $r_0 = 0.25$, $\eta = 0.5$, $\beta_0 = 0.64$, $A = 1$. Panel (a): $kT_{\rm e} = 5$ keV, Panel (b): $kT_{\rm e} = 15$ keV.*

latter assumption may be considered an oversimplification of the problem. A most realistic approach would consist indeed in an energy-dependent treatment of the albedo, a problem that could be faced only with MonteCarlo simulations, with the additional complications arising from a detailed treatment of the star photosphere (surface) properties. For our unavoidably simplified assumptions, the net effect of increasing values of A is a progressive flattening of the emerging spectra. This is physically explained because when $A > 0$, a fraction of photons

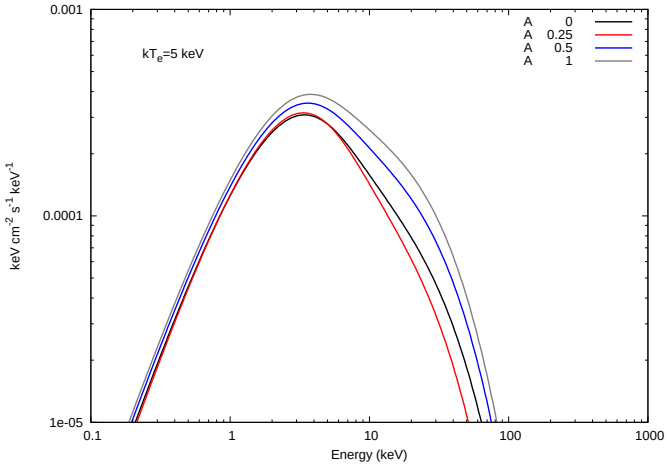

(a)

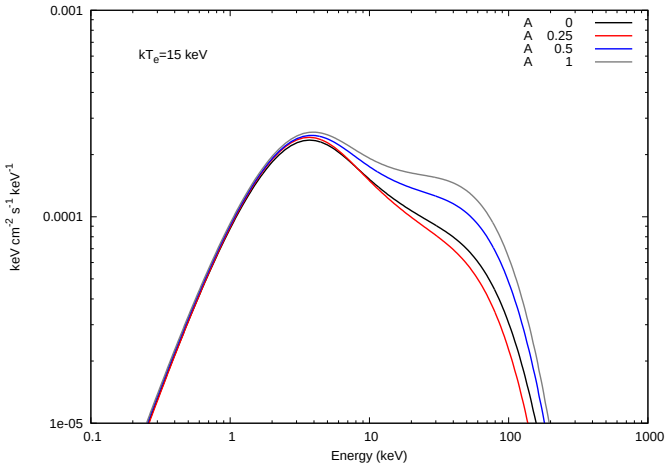

(b)

Figure 6.9: *Same as Fig. 6.1 but for different values of the albedo A, with the velocity profile of equation (5.24). Fixed parameters are* $kT_{\rm bb} = 1$, $\tau = 0.4$, $\eta = 0.5$, $\beta_0 = 0.64$, $r_0 = 0.25$.
Panel (a)*:* $kT_{\rm e} = 5$ *keV, Panel* (b)*:* $kT_{\rm e} = 15$ *keV.*

(which becomes 100% when A=1) suffers on average more scattering with respect to $A = 0$. Qualitatively, the spectral modification leads in the same direction as an enhanced optical depth of the system. The last parameter that strongly influences the spectral formation is the radius of the accretion column r_0, whose effects are shown in Fig. 6.6. Indeed, following the BW07 prescription, the mean escape time for photons using the diffusion approximation $t_{\rm esc} \propto r_0^2$ (see Eq. [5.10]). On the other hand, both the bulk and thermal Comptonization parame-

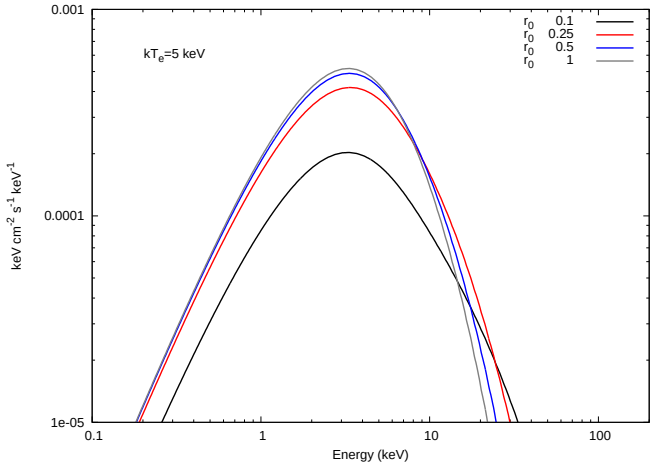

(a)

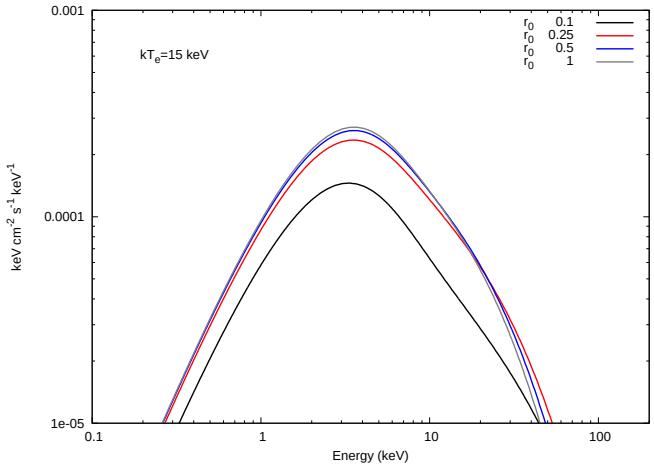

(b)

Figure 6.10: *Same as Fig. 6.1 but for different values of the accretion column radius r_0, with the velocity profile of equation (5.24). Fixed parameters are $kT_{\rm bb} = 1$ keV, $\tau = 0.2$, and $A = 1$. Panel (a): $kT_{\rm e} = 5$ keV. Panel (b): $kT_{\rm e} = 15$ keV.*

ters ($y_{\rm bulk}$ and $y_{\rm th}$, respectively) are related to the mean number of scatterings that photons experience in the medium via

$$\begin{aligned} y_{\rm bulk} &\approx N_{\rm av}^{\rm bulk}\zeta_{\rm bulk}, \\ y_{\rm th} &\approx N_{\rm av}^{\rm th}\zeta_{\rm th}, \end{aligned} \tag{6.2}$$

where $N_{\rm av}^{\rm bulk}$, $\zeta_{\rm bulk}$, $N_{\rm av}^{\rm th}$ and $\zeta_{\rm th}$ are the averaged number of scatterings and the fraction energy gain per scattering for bulk and thermal Comptonization,

respectively. Both $N_{\rm av}^{\rm bulk}$ and $N_{\rm av}^{\rm th}$ are of course also proportional to $t_{\rm esc}$ (see Eqs.[94]-[97] in BW07). Evidently therefore, for fixed velocity profile parameters $\mathscr{A}$ and η (see Eq. [5.20]), once the optical depth τ is defined (see Eq. [5.22]), to keep its value constant for increasing r_0 (as reported in Fig. 6.6), the accretion rate $\dot{m}$ must also increase in a way to keep the ratio $\dot{m}/r_0^2$ constant. Combining equation (5.10) and (5.21) yields $t_{\rm esc} \propto \dot{m}$, which in turn leads to an enhancement of the Comptonization parameters $y_{\rm bulk}$ and $y_{\rm th}$ in equation (6.3) with a hardening of the spectral shape. Considering now the velocity profile defined in equation (5.24), we see that the results are qualitatively the same as in equation (5.23) as far as the spectral modifications induced by variations of $kT_{\rm e}$ are concerned (Fig. 6.7), τ (Fig. 6.8) and A (Fig. 6.9), respectively. But there are opposite effects that are induced in the emerging spectra by different values of the accretion column radius r_0 for the velocity profile here considered. Indeed, using equation (5.12) and the definition of τ in equation (28) of BW07, which allows us to express the accreting matter velocity in terms of the z-coordinate, in spite of the optical depth τ, it is straightforward to see that $\beta(z) \propto r_0^{-1/2}$. In particular, if $z_0 = 2.42$ and $z_{\rm max} = 2z_0$ we have $\beta_{\rm max}$=0.60 for $r_0 = 0.1$, $\beta_{\rm max}$=0.38 for $r_0 = 0.25$, $\beta_{\rm max}$=0.27 for $r_0 = 0.5$ and $\beta_{\rm max}$=0.2 for $r_0 = 1$, respectively. Note that because equation (5.24) describes matter that stagnates at the star surface, here $\beta_{\rm max}$ represents the velocity at the accretion column altitude $z_{\rm max}$. In other words, while using equation (5.23), the choice of r_0 does not modify the velocity field of the accreting matter, which is only determined by the choice of β_0 and η, for (5.24) as r_0 increases the bulk contribution to the spectral formation becomes less important, and this drop is not compensated by the increase of the photon mean escape time $t_{\rm esc}$, which, as explained above, would instead contribute to spectral hardening.

6.2 XSPEC implementation

Our model will be distributed as a contributed model to the official XSPEC* web page.
In Table 6.1 we report a summary of the free parameters of the model, with their physical meaning. The code was written in C-language, and can be easily installed following the standard procedure reported both in the official XSPEC manual and in the brief cookbook which will be delivered together with the source code. As a general concern for users, it is important to point out that, in general, the emergent spectrum obtained from the Comptonization of a seed photon population with any given energy distribution S(E) can be presented as the sum of the seed spectrum plus its convolution with the scattering Green's function $G(E, E_0)$ of the electron plasma, each with their relative weight, according to the general formalism

$$F(E) = \frac{C_n}{A+1}[S(E) + A\ S(E) * G(E, E_0)], \tag{6.3}$$

*http://heasarc.nasa.gov/xanadu/xspec/newmodels.html

Table 6.1: *Parameter description of the XSPEC model COMPMAG .*

Parameter	Units	Description
$kT_{\rm bb}$	(keV)	Seed photons blackbody temperature
$kT_{\rm e}$	(keV)	Electron temperature
τ		Optical depth of the accretion column
η		Index of the velocity profile (Eq. [5.23])
β_0		Terminal velocity at the NS surface (Eq. [5.23])
r_0		Radius of the accretion column in units of the NS Schwarzschild radius
A		Albedo at the NS surface
Prof		If Prof= 1, $\beta(\tau)$ defined in equation (5.23) otherwise as in equation (5.24)
Norm		$R^2_{\rm km}/D^2_{10}$

where C_n is a normalization constant. The ratio $A/(A+1)$ is the Comptonization fraction and its value qualitatively determines the contribution to the total spectrum of the Comptonized photons. The value of A may depend on several geometrical and physical factors, such as, e.g., the spatial seed photon distribution inside the system configuration (see Fig. [4] in TMK97). The lower the value of A, the more enhanced is the direct seed photon spectrum S(E). Examples of XSPEC models which make use of the definition in equation (6.3) are BMC (TMK97) and COMPTB (F08). Either model, however, does not solve the full RTE including the photon spatial diffusion and distribution, the latter being an unknown quantity which is phenomenologically described through the continuum parameter log(A). On the other hand, in our present model it is not possible to change arbitrarily, i.e., according to the observed spectra, the value of log(A). Its value is implicitly determined once the seed photon spatial distribution is fixed. We have presented the results of simulated spectra assuming a uniform distribution over τ for S(E), which was assumed to be a black-body; in this case, the transition from the low-energy part of the spectrum (the Rayleigh regime for $E \lesssim 3kT_{\rm bb}$) to the high-energy (Comptonized) power-law shape is almost smooth; this corresponds approximately to the case $A \gg 1$ in equation (6.3). However, for other seed photons spatial distributions (e.g., exponential over tau), the onset between the black-body peak and the powerlaw-like regime can be characterised by a jump, meaning $A \lesssim 1$. Thus, for observed spectra where a direct and enhanced blackbody-like component is required by the fit, our claim is to model the source continuum with a (BB + COMPMAG) model by keeping the temperatures of the direct and Comptonized black-body component fixed and equal to each other.

7

SFXTs Spectral Fitting

The present Chapter will be dedicated to the spectral fitting of the *Swift* observation of the prototype Supergiant Fast X-ray Transients (SFXTs) XTE J1739-302 (or, equivalently, IGR J17391-3021) and IGR J17544-2619 with several models including COMPMAG .

7.1 Swift Gamma-Ray Burst Mission

The *Swift* Gamma-Ray Burst Mission is a robotic spacecraft, developed by an international collaboration between United States, United Kingdom and Italy. *Swift* is a part of NASA's Medium Explorer Program (MIDEX) and is managed by the NASA Goddard Space Flight Center. The spacecraft was launched into orbit on 20 November 2004, 17:16:00 UTC on a Delta II 7320-10C expendable launch vehicle. The near-perfect orbit is a 586×601 km of altitude, with an inclination of 20°. The telescope was declared fully operational on February 1, 2005, when the *Swift* team released the first light picture of the ultraviolet/optical instrument.

The name *Swift* is not a mission related acronym, but rather a reference to the capability of the instrument to change direction abruptly and the nimble bird of the same name. Indeed, the mission was conceived as dedicated to the study of Gamma-Ray Bursts (GRBs) that need a very quick pointing in order to detect the overall event from prompt emission to the end of the afterglow. In the time between GRBs events, *Swift* is available for other scientific investigations. Observation times can be obtained through the submission of proposals.

The *Swift* Mission Operation Center (MOC), where commanding of the satellite is performed, is placed in State College, Pennsylvania. The Swift main ground station is located at the Broglio Space Centre near Malindi on the coast of Eastern Kenya, and is operated by the Italian Space Agency. The operations are directed by the Pennsylvania State University and industry subcontractors. The

Science Data Center (SDC) and the archive are located at the Goddard Space Flight Center outside Washington D.C. The UK *Swift* Science Data Centre is located at the University of Leicester.
The spacecraft bus was built by Spectrum Astro, which was later acquired by General Dynamics Advanced Information Systems. *Swift* is a multi-wavelength space-based observatory made of three instruments that work together to detect events from gamma-ray to optical wavebands.
The Burst Alert Telescope (BAT) firstly detects the GRBs events and calculates its coordinates in the sky. It covers one steradian fully coded and three steradians partially coded over the 12.6 steradians of the full sky. Within 15 seconds it determines the position of the event with an accuracy of 1 to 4 arc-minutes. The coordinates are immediately communicated to the ground, where some wide-field, rapid-slew ground-based telescopes catch themselves the GRB. The BAT uses a coded-aperture mask of 52,000 randomly placed 5 mm lead tiles, 1 metre above a detector plane of 32,768 four mm CdZnTe hard X-ray detector tiles; it is purpose-built for Swift. The energy range coverage spans from 15 keV up to 150 keV. This instrument was thought for the study of bursts with a large variety of intensities, duration and temporal structures. The solid state detector array allows the detection even of very weak bursts, while the large field of view (FOV) guarantees to see a good fraction of bright bursts. Since the field of view of the BAT includes also the FOV of the other two instruments, its possible to study simultaneously the duration gamma-ray/X-ray and UV/optical emission. The BAT data will produce over the course of *Swift*'s two years mission, a sensitive hard X-ray all-sky survey.
The X-ray Telescope (XRT) takes images and performs spectral analysis of the GRB afterglow. The XRT provides a more definite location of the event, with a typical error circle of approximately 2 arc-seconds radius. Then it continues monitoring the GRB afterglow light curves for a period of days up to weeks after the event, depending on the brightness of the afterglow (it will cover a dynamic range of more than 7 order of magnitude in flux). The XRT uses a Wolter Type I X-ray telescope with 12 nested mirrors, focused onto a single MOS charge-coupled device (CCD) similar to those used by the XMM-Newton EPIC MOS cameras. The instrument is able to select by itself the most appropriate observing mode for each object, depending on its measured count rate. The energy range of the XRT is 0.2-10 keV.
After Swift has rapidly changed its pointing direction towards a GRB, the Ultraviolet/Optical Telescope (UVOT) is used to detect an optical afterglow. The UVOT provides a sub-arcsecond position and provides optical and ultra-violet photometry through lenticular filters and low-resolution spectra (170–650 nm) in a $17' \times 17'$ field through the use of its optical and UV grisms. Despite its limited aperture, UVOT is a powerful complement to other instruments because of its UV capabilities and the absence of atmospheric extinction, diffraction, and background. The UVOT is also used to provide long-term follow-ups of GRB afterglow light curves. The UVOT is based on the XMM-Newton mission's Optical Monitor (OM) instrument, with improved optics and upgraded on board

processing computers. The UVOT is a diffraction-limited 30 cm (12" aperture) modified Ritchey-Chretien UV/optical reflector, sensitive to magnitude 24 in a 17 minute exposure, CO-aligned with the XRT. An 11-position filter wheel allows low-resolution grism spectra of bright GRBs, magnification, and broad-band UV/visible photometry. Photons register on a microchannel plate intensified CCD (MIC) [122][*,†].
The scientific goals of the *Swift* mission, as the name suggests, are focused on the GRBs physics. Indeed, the objectives are: the determination of GRBs' origin, their classification and, possibly, the discovery of new types, the interaction of the ultra-relativistic outflows of GRBs with the surrounding medium, and the use of GRBs to study early universe out to $z > 10$. However, in addition, the mission is performing an hard X-ray survey to a sensitivity of $\sim 2 \times 10^{-11}$ erg cm^{-2} s^{-1} in the 15-150 keV, which will substantially improve the *HEAO 1* A-4 survey. The extremely rapid follow-up observations and the rapid data sharing system are making the mission very effective also for all the types of high-energy transient sources, like Supergiant Fast X-ray Transients (SFXTs).

7.2 Supergiant Fast X-ray Transients

After the *INTEGRAL* galactic plane survey, which started in 2002, was claimed the existence of a new class of High Mass X-ray Binaries (HMXBs). SFXTs are binary systems, associated with an OB supergiant, and a compact object, presumably a neutron star. they are persistent X-ray sources, which show a variability on short timescales, probably due to the physical characteristic of wind accretion, and a relatively stable behaviour on the long term [84].
The outburst activity is shorter than typical Be/X-ray binaries and are characterised by bright flares, that last a few hours [85],[86],[87], with a peak luminosity of order of $10^{36} - 10^{37}$ erg s^{-1} [88],[89]. A small number of SFXTs has been observed in a quiescent state, characterised by a soft spectrum approximately thermal with lower luminosities ($L_x \sim 10^{32}$ erg s^{-1}) [90],[91],[92]. The SFXT luminosity seems to have a wide dynamical range and, if the orbit is eccentric, can be modulated on the orbital period of the system [93].
A typical SFXT outburst is defined as a strong peak plus a flaring activity, with secondary peaks before and after the maximum flux of the main peak. The average duration of the activity period is about ~ 6 hours, but it depends on the peculiar characteristic of the outbursts. As a general classification, there are fainter ($L_x \sim 10^{33} - 10^{34}$ erg s^{-1}) and more numerous outbursts having a mean count rate ~ 10 count s^{-1}, and may have a very short duration (~ 0.6 h), in addition to brighter and less frequent outbursts with a mean count rate of order of ~ 60 count s^{-1}, up to ~ 190 count s^{-1} and, on average, they last 1 hour more than the fainter ones [94].
The hard X-ray spectral shape of SFXTs presents all the characteristics of a spec-

[*] http://www.swift.psu.edu/
[†] http://en.wikipedia.org/wiki/Swift_Gamma-Ray_Burst_Mission

trum belonging to a HMXB hosting a neutron star. At energies below 10 keV the spectrum is a flat hard power-law, then, for $E \sim 15-30$ keV, there is high-energy cut-off. Moreover, a fraction of SFXTs shows a strong absorption at soft energies [96],[97].

Although, these features seem to confirm undoubtedly the identification of the compact object as a pulsar, just a few SFXTs indeed show a pulsation, namely, AX J1841.0-0536 with $P_{spin} \sim 4.7$ s [98], IGR J16465-4507 with $P_{spin} \sim 228$ s [99], IGR J11215-5952 with $P_{spin} \sim 187$ s [100] and IGR J18483-0311 with $P_{spin} \sim 21$ s [101]. Several attempts have been proposed to explain the lack of pulsations in the most of SFXTs. The photon index and, probably, a marginal evidence of Cyclotron Resonant Scattering Feature (CRSF) at 30 keV and 60 keV, suggested by [94] for XTE J1739-302, cannot completely ruled out the possibility that the compact object is a black hole. Geometrical effects are also being investigated as possible explanation [102], [103], [104]. For instance, if the magnetic axis is aligned with the spin axis of the neutron star, we are able to see only one pole, or, we could obtain the same result if the orbit has a very small inclination angle. Another possibility is that the pulsars in SFXTs are slowly pulsating, like 2S 0114+650 with a period of ~ 2.8 h [105], or 4U 1954+319 in a Low Mass X-ray Binaries (LMXBs) with a period of ~ 5 h [106]. However, the apparent lack of pulsations can be due, for instance, to electron scattering occurring in an optically thick medium that smears out the pulsations [107]. This effect is supported by the evidence of the presence of an high absorption column.

The large variety of activities and dynamic range of luminosities of SFXTs have aroused the interest of the linked scientific community and different models have been proposed to explain their properties. The Bondi-Hoyle accretion, *per se*, can not, in fact, explain all types of outbursts.

In 2007, Sidoli et al. [108] suggested that the SFXTs period outbursts can be originated by the crossing of an additional equatorial wind component. Indeed, the authors proposed that, besides the spherical symmetric wind from the supergiant, there may be a denser and slower equatorial component, which can, in principle, be inclined with respect to the orbital plane of the system. Depending on the inclination angle and on the eccentricity of the orbit, this model suggests a possible explanation for both the periodic and persistent emission of SFXTs.

Grebenev & Sunyaev [109] and Bozzo et al. [110] proposed a gated mechanism involving transitions across a magnetic or centrifugal barrier. The accretion can be interrupted traversing the barrier. Such mechanism requires specific properties of the neutron star, which are long spin periods ($P_{\rm spin} \gtrsim 1000$ s) and strong magnetic fields ($B \gtrsim 10^{14}$ G). Nonetheless, a magnetar-like field seems to be extremely large for the hosted compact object in the SFXTs [94], [111].

Alternatively, in't Zand [91] discussed the possibility to have a spherically symmetric clumpy wind. The short flares within this scenario are attributed to the accretion of massive clumps ($10^{22} - 10^{23}$ g) which are present in the supergiant wind. The distribution of the clumps decreases as the distance from the OB star increases. Therefore, HMXBs show a persistent emission because of the small separation between the compact object and the companion. Conversely, SFXTs

are transient sources due to the larger distance between the two components of the system [112], [113], [114]. The main drawback of the clumpy wind model is that it cannot explain the outburst periodicity.
A smart combination of the equatorially enhanced wind and a clumpy spherical symmetric wind with distribution for the masses and the initial dimensions of the clump have been proposed by Ducci et al. [115].
From the observational point of view, *Swift* [122] has been shedding new light on the phenomenon of SFXTs, thanks to its unique properties of automatic fast-slewing and broad-band energy coverage, that make it the only observatory which can detect outbursts from SFXTs from the very beginning and observe their evolution panchromatically.
The bright flares from SFXTs have been triggering the Burst Alert Telescope [135] since early after launch. Several flares were also observed with the X-ray Telescope [136] during the monitoring campaigns that were performed, taking advantage of Swift's scheduling flexibility, on 4 SFXTs during 2007-2009 [138], [137],[132]. A few more flares were also caught by the BAT Transient Monitor [129], [139][‡].
XTE J1739-302 and IGR J17544-2619 are considered the prototypes of the SFXT class, and were therefore extensively studied with *Swift*. In this Chapter, we examine the most recent outbursts of these two sources, which triggered BAT in 2011.

7.3 XTE J1739-302

The source XTE J1739-302 is widely recognised as a SFXTs prototype. It was discovered in August 1997 with *Rossi X-Ray Timing Explorer* (RXTE) after a short outburst and was detected for a period of a few hours [116]. The spectrum is well modelled with a bremsstrahlung component at temperature $21 - 22$ keV with a peak flux of 3.6×10^{-9} erg cm^{-2} s^{-1} in the $2 - 25$ keV range and possible absorption features (CRSF) at 30 and 60 keV [94]. Otherwise, an absorbed (4.2×10^{22} cm^{-2}) cut-off power-law model was proposed [116]. Other short flares were observed with the *RXTE/Proportional Counter Array* (RXTE/PCA) [90]. The optical counterpart was identified by *Chandra* as a O8I star [89] situated at 2.7 kpc [117]. From March 2003 up to 2005 *INTEGRAL IBIS/ISGRI* observed six bright outbursts, each of them lasted ~ 5 hours and has a complex structure [118], [90]. Recently, it was detected by *Swift* BAT, which managed to observe the brightest part of a flare at soft energies [119] with the *Swift* X-Ray Telescope (XRT). The same event was also detected by the *INTEGRAL/JEM-X* monitor [120]. Throughout all these observations, no periodicity was found up to timescales of 1000 s.
Recently, Drave [95] reported the discovery of a 51.47 ± 0.02 d orbital period based on ~ 12.4 Ms of *INTEGRAL* data.

[‡]http://swift.gsfc.nasa.gov/docs/swift/results/transients/

Table 7.1: *Spectral fits of simultaneous XRT and BAT data of XTE J1739-302 with several models.*

Parameters	Models			
	COMPMAG	COMPTT	CUTOFF-PL	BB+BB
$N_{\rm H} \times 10^{22}$ cm^{-1}	$1.18^{+0.12}_{-0.09}$	$0.81^{+0.11}_{-0.10}$	$1.97^{+0.17}_{-0.16}$	$1.07^{+0.10}_{-0.09}$
$kT_{\rm bb}$ (keV)	$1.63^{+0.10}_{-0.17}$	-	-	-
$kT_{0,\rm bb=1}$ (keV)	-	$1.34^{+0.07}_{-0.06}$	-	$1.88^{+0.09}_{-0.15}$
$kT_{0,\rm bb=2}$ (keV)	-	-	-	$6.60^{+0.57}_{-0.48}$
kT_e (keV)	$9.62^{+4.05}_{-2.58}$	$8.83^{+1.88}_{-1.11}$	-	-
Γ	-	-	$0.25^{+0.11}_{-0.10}$	-
E_{cut} (keV)	-	-	$9.19^{+0.95}_{-0.80}$	-
τ	$0.33^{+0.30}_{-0.03}$	$3.61^{+0.51}_{-0.79}$	-	-
β_0	0.05	-	-	-
r_0	0.25	-	-	-
$F^*_{0.1-200\,\rm keV}$	7.4	6.8	7.1	5.6
χ^2/d.o.f.	1.21/242	1.19/242	1.50/243	1.18/242

* Unabsorbed 2–10 keV fluxes (10^{-9} erg cm^{-2} s^{-1}).

7.4 IGR J17544-2619

IGR J17544-2619 was first detected by *INTEGRAL* in 2003 by [123], when the source reached a flux of 160 mCrab (18–25 keV). Several more flares, lasting up to 10 hours, were detected by *INTEGRAL* in the following years [124], [126], [90], [125], [127] with fluxes up to 400 mCrab (20–40 keV); some were also found in archival *BeppoSAX* observations [128]. Subsequent flares were observed by *Swift* [129], [130],[131], [132], [133], [134], and *SUZAKU* [140]. [141] reported the discovery of a 4.926 ± 0.0001 d orbital period based on the $\sim$ 4.5 years of *INTEGRAL* data. The optical counterpart is an O9Ib star at 3.6 kpc [142], [143].

7.5 Spectral Analysis

We perform a broad-band spectroscopy of the 2011 outburst data collected by *Swift* of the two SFXTs XTE J1739-302 and IGR J17544-2619. We extracted simultaneous spectra from both XRT and BAT event lists in the time interval 147-903 s for XTE J1739-302 and 133-783 s for IGR J17544-2619 since the BAT trigger. The energy band we considered are: $0.5 - 10$ keV and $15 - 60$ keV for XRT and BAT, respectively. We include in the fitting process a factor for each instrument, constrained within its allowed range (0.9-1.1), in order to have correct normalisation uncertainties between the two instruments.
We fit these data with several models, including COMPMAG . In particular, we compare: *a)* a generic Comptonization model (COMPTT) in diffusion approximation for a disk geometry without dynamical bulk component, *b)* a power-law model with an exponential cutoff (CUTOFF-PL), which is a typical phenomenological model used to describe the X-ray emission from the accreting pulsars hosted in HMXBs, *c)* a composition of two blackbodies with different temperatures and radii, sometimes used to fit *magnetar* (BB+BB) [29] and *d)* our COMPMAG model for accretion column onto magnetised pulsars with bulk velocity profiles (5.23) with $\eta = 0.5$ and $\beta_0 = 0.05$. The radius of the accretion column is set to the value $r_0 = 0.25$ and the optical depth is calculated following (5.22). The set of initial parameters for both XTE J1739-302 and IGR J17544-2619 should satisfy the conditions on the spatial diffusion coefficients $\mathcal{D}_\parallel$ and $\mathcal{D}_\perp$ (see Par. 5.2). For XTE J1739-302, we have

$$\mathcal{D}_\parallel \sim 10^{-3} \qquad \text{and} \qquad \mathcal{D}_\perp \sim 3 \times 10^{-2} \tag{7.1}$$

for an optical depth $\tau = 0.33$ and an accretion rate $\dot{m} = 0.64$. For IGR J17544-2619, we obtain

$$\mathcal{D}_\parallel \sim 0.7 \times 10^{-4} \qquad \text{and} \qquad \mathcal{D}_\perp \sim 2 \times 10^{-3} \tag{7.2}$$

for an optical depth $\tau = 1.19$ and an accretion rate $\dot{m} = 2.31$. As we can see, the diffusion coefficients are much less than 1 for both sources, therefore the diffusion approximation, for these sets of parameters is applicable.
Table 7.1 reports the broad-band simultaneous fits we obtained for XTE J1739-302. Comparing the reduced chi-squares, we note that the CUTOFF-PL is the worst ($\widetilde{\chi}^2 = 1.50$ for 243 d.o.f.) with respect to $\widetilde{\chi}^2 = 1.21$ (for 242 d.o.f.) found with COMPMAG , $\widetilde{\chi}^2 = 1.19$ (for 242 d.o.f.) obtained with COMPTT and $\widetilde{\chi}^2 = 1.18$ (for 242 d.o.f.) obtained with BB+BB. In the COMPMAG model we have frozen four parameters: we have chosen the velocity profile (5.23) with $\eta = 0.5$ and $\beta_0 = 0.05$ and the accretion column radius is fixed to $r_0 = 0.25$.
The photons absorption goes from $\sim 0.81 \times 10^{22}$ cm^{-1} of the COMPTT model to $\sim 1.97 \times 10^{22}$ cm^{-1} for the cutoff power-law. All the values of the $N_{\rm H}$ parameter are on average smaller or compatible than the previous estimates of the XTE J1739-302 absorption, but, however, it seems to have wide range of variability [90].

Table 7.2: *Spectral fits of simultaneous XRT and BAT data of IGR J17544-2619 with several models.*

Parameters	Models			
	COMPMAG	COMPTT	CUTOFF-PL	BB+BB
$N_{\rm H} \times 10^{22}$ cm^{-1}	$0.68^{+0.10}_{-0.08}$	$0.58^{+0.07}_{-0.06}$	$0.73^{+0.06}_{-0.06}$	$0.58^{+0.07}_{-0.06}$
$E_{edge}(keV)$	22±2	21±2	23±1	-
τ_{edge}	$0.81^{+0.52}_{0.23}$	$0.62^{+0.35}_{-0.31}$	$1.35^{+0.54}_{-0.43}$	-
$kT_{\rm bb}$ (keV)	$0.73^{+0.11}_{-0.10}$	-	-	-
$kT_{0,\rm bb=1}$ (keV)	-	$0.63^{+0.07}_{-0.08}$	-	$0.93^{+0.07}_{-0.07}$
$kT_{0,\rm bb=2}$ (keV)	-	-	-	$3.45^{+0.08}_{-0.07}$
kT_e (keV)	$3.47^{+0.34}_{-0.02}$	$3.92^{+0.18}_{-0.16}$	-	-
Γ	-	-	$0.04^{+0.07}_{-0.07}$	-
E_{cut} (keV)	-	-	$7.50^{+0.54}_{-0.49}$	-
τ	$1.19^{+0.09}_{-0.10}$	$10.7^{+0.7}_{-0.7}$	-	-
β_0	0.05	-	-	-
r_0	0.25	-	-	-
$F^*_{0.1-200\,\rm keV}$	8.2	8.1	7.7	7.9
χ^2/d.o.f.	1.10/295	1.09/295	1.16/296	1.13/297

* Unabsorbed 2–10 keV fluxes (10^{-9} erg cm^{-2} s^{-1}).

The Comptonization models (COMPTT and COMPMAG) gives as best fit a black-body temperature of the seed photons of the order of $\sim 1.3 - 1.6$ keV and an electron plasma temperature kT_e of ~ 9 keV. Such temperatures suggest that the multiple inverse Compton process should be in the unsaturated regime ($y_{\rm NR} \sim 1$ and τ of the order of unity) therefore both electrons and photons have maintained the original information belonging to the source and the plasma itself.

A possible interpretation that we may provide on the basis of the temperatures found for the two blackbodies can be that, while the softer ($\sim 1.8-1.9$ keV with $R_{\rm bb,1} \sim 1$ km) may carry some information about the seed photon distribution, the harder (~ 6.6 keV with $R_{\rm bb,1} \sim 0.1$ km) population of photons can derived from a saturated Comptonization and gives a Wien spectrum in which there is no trace of the temperature of the plasma.
The power-law index ($\Gamma \sim 0.25$) and the cutoff energy ($E_{cut} \sim 9.2$ keV) seems to be in good agreement with previous spectral analysis [90], [94].
For what concerns the comparison of optical depths between COMPMAG and COMPTT , we need a much more extensively discussion.
From Table 7.1, we note that between the optical depths estimated with the two models there is one order of magnitude ($\tau \sim 0.33$ for COMPMAG and $\tau \sim 3.6$ for COMPTT). In particular, the value reported from the COMPMAG best fit seems to suggest a very low Comptonization parameter (See Chap. 2), thus a tiny deviation in the shape of the spectrum from the initial BB source function and an almost negligible change of the total energy of photons. Nevertheless, as we see also from Fig. 7.1 (Panel (a) and (b)), COMPMAG and COMPTT give rise basically to the same spectrum. This is due to the presence of the strong magnetic field.
In COMPTT , which is a generic (zero external field) static Comptonization model calculated in Fokker-Planck approximation, the optical depth is the standard Thompson optical depth for electron scattering

$$\tau_{\rm T} = \int_r^H \sigma_{\rm T} n_e(r') dr', \tag{7.3}$$

where $\sigma_{\rm T}$ is the classical Thomson scattering cross section, $n_e(r)$ is the electron number density and H is the height of the slab [43].
In the COMPMAG model (applied to BW07) the scenario is more complex.
In BW07, the system under investigation is a cylindrical slab of magnetised plasma. As we have already discuss in the previous Chapters, when a strong magnetic field is present, the medium becomes birefringent respect to the radiation and we may say that, in first approximation, there are two polarisation modes with different cross-sections and, therefore, different opacity, depending on energy and angle between the direction of propagation of photons and the magnetic field.
Following Wang & Frank [121], BW07 introduced constant, energy- and angle-averaged cross-sections, $\sigma_{\parallel}$ and $\sigma_{\perp}$, as a further approximation of (2.10)-(2.12), in order to greatly simplify the RTE, which, in principle, should be a system of two integro-differential equations.
The equation they considered to characterise the problem is the time-independent version of Eq.18 in [49], plus an "escape time" term (see Eq. 5.9). Such equation is purely differential, i.e. a RTE in Fokker-Planck approximation. As we have discussed before, the diffusion approximation does not hold when a strong magnetic field is present, because the photon occupation number can be no longer assumed as isotropically distributed. Under some assumptions, we have seen (see

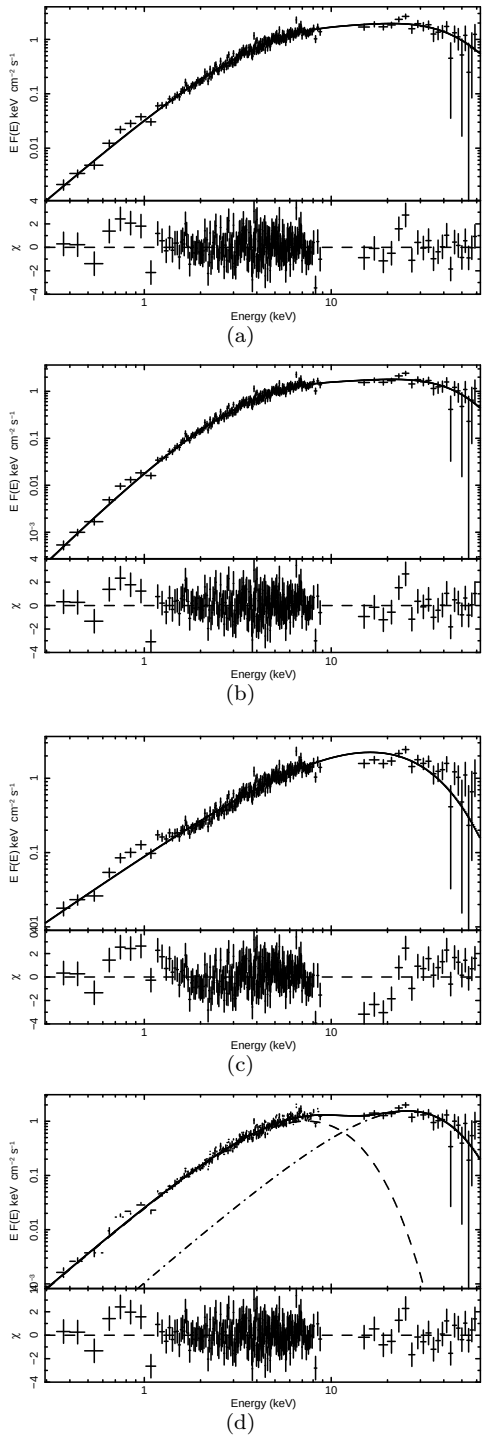

Figure 7.1: *Absorption-corrected EF(E) spectra, best-fit models reported in Table 7.1 and residuals between the data and the model in units of σ for XTE J1739-302. Panel* (a)*: COMPMAG. Panel* (b)*: COMPTT. Panel* (c)*: CUTOFFPL. Panel* (d)*: BB+BB.*

Chap. 2) that is possible to neglect the anisotropic part of the photon occupation number, maintaining the integro-differential nature of RTE.
BW07, instead, argued that the diffusion approximation can be applied also in this case, through the introduction of the escape time term. This term is included in the RTE in order to describe the spatial diffusion of photons through the slab with a differential diffusion operator (see Par. 5.2), replacing the solution of integral equation (2.23).
In particular, if both the coefficients in $\mathcal{D}_{\parallel}$ and $\mathcal{D}_{\perp}$ are < 1, the diffusion approximation is valid. Therefore, it is crucial to choose the COMPMAG parameters in order to operate in this regime.
The details of the escape time prescription and the validity of diffusion approximation are given in [62], [61] and [63].
If we assume that all the above assumptions are valid, the *averaged* optical depth that characterises our system is (5.22) or, more simply $d\tau = n_e\,\overline{\sigma} dz \simeq 0.1\,\sigma_{\rm T} n_e\,dz$, where we have defined the mean cross section $\overline{\sigma} \sim 0.1\,\sigma_{\rm T}$ between the ordinary ($\sigma_{\perp} \sim \sigma_{\rm T}$) and extraordinary ($\sigma_{\parallel} \sim 10^{-3}\sigma_{\rm T}$) photons cross sections, as suggested in [28]. The "effective" averaged optical depth is evidently an order of magnitude less than (7.3).
In Fig. 7.1 are presented the best fit models. In Panel (a) and Panel (b) the spectral fits are those obtained with COMPMAG and COMPTT , respectively, and, as we have already pointed out, there is no appreciable difference between the two fits. In Panel (c) we report the best fit relative to the cutoff power-law. We may see immediately that the index of the power-law is not well constrained by the fit, also due to the wide uncertainties that characterise the high-energy data of BAT instrument. In Panel (d) there is shown the best fit obtained with the two blackbodies.
Table 7.2 reports the best fit of IGR J17544-2619 obtained with the same models adopted for XTE J1739-302. The fit of the broad-band spectrum with a photoelectrically-absorbed cut-off power-law provides $\chi^2 = 1.28$ for 298 d.o.f. and indeed adequately describes the XRT spectrum and the BAT spectrum above 30 keV, but a a sinusoidal-like feature in the 15-30 keV region is clearly observed. Including an absorption edge in the model improves the statistical result to $\chi^2 = 1.16$ for 296 d.o.f., with $E_{\rm ed} \sim 23$ keV and $\tau_{\rm ed} \sim 1.35$. The F-test for discriminating among two different models (namely without and with the absorption edge) provides however a probability of chance improvement (PCI) of about only 20%.
The models COMPTT and EDGE $\times$COMPTT with $E_{\rm ed} \sim 21$ keV and $\tau_{\rm ed} \sim 0.62$ provide $\chi^2 = 1.14$ for 297 d.o.f. and $\chi^2 = 1.09$ for 295 d.o.f., respectively, with PCI of 35%.
A satisfactory fit can also be obtained by the sum of two blackbody spectra, which provides $\chi^2 = 1.13$ for 297 d.o.f. (Panel (b) in Fig. 7.2). The temperatures and apparent radii (at a distance of 3.6 kpc) of the two BBs are $kT_{\rm bb,1} \sim 0.9$ keV, $R_{\rm bb,1} \sim 3.5$ km, and $kT_{\rm bb,1} \sim 3.5$ keV, $R_{\rm bb,2} \sim 0.8$ respectively. Panel (a) in Fig. 7.2 presents the best fit for EDGE $\times$ COMPMAG for the values of the parameters reported in Table 7.2. Also in this case we obtain an improvement if

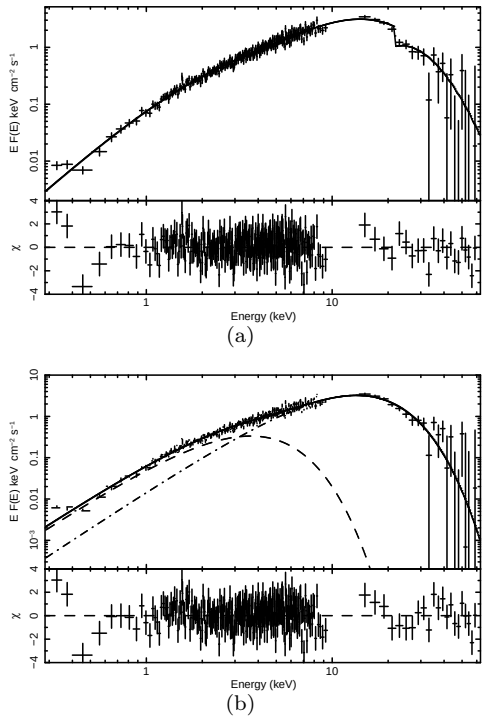

Figure 7.2: *Absorption-corrected EF(E) spectra, best-fit models reported in Table 7.2 and residuals between the data and the model in units of σ for IGR J17544-2619. Panel (*a*): BB+BB. Panel (*b*): EDGE ×COMPMAG , with β_0=0.05, $r_0 = 0.25$.*

we include an edge for $E_{\rm ed} \sim 22$ keV and $\tau_{\rm ed} \sim 0.81$.

7.6 Discussion on SFXTs Accretion Geometry

The joint XRT/BAT spectra of both XTE J1739-302 and IGR J17544-2619 can be described by either a simple Comptonization model, like COMPTT and COMPMAG or phenomenological models such as a sum of two BB spectra or a cutoff power-law (see tables 7.1 and 7.2). From a pure statistical point of view it is not possible to distinguish among these possibilities. There is however an interesting aspect to discuss which has not been yet fully faced in the accretion physics of SFXTs.

If we pay attention on the results using the COMPTT and COMPMAG models, it easy to show that the electron density where Comptonization takes place is of order of 10^{19} cm^{-3}. Indeed, the Thomson optical depth is given by

$$\tau \approx 7\ n_{19}\ r_6, \tag{7.4}$$

where $n_{19} \equiv n_{\rm e}/10^{19}$ and $r_6 \equiv R/10^6$ are dimensionless electron density and system length scale, respectively. If spectral formation occurs close to the neutron star ($r_6 \sim$ 1-2), from the COMPTT best-fit values of τ reported in the tables 7.1 and 7.2, it is evident that $n_{19} \sim 1$. The possible presence of a strong magnetic field ($B \gtrsim 10^{12}$ G), with associated reduction of the Thomson cross-section $\sigma_{\rm T}$ would actually require an even higher electron density. This is indeed confirmed from the results obtained using the COMPMAG model (see tables 7.1 and 7.2) developed by F12.

The electron density for column accretion, which is the configuration assumed in COMPMAG is given by

$$n_{\rm e} = 1.1 \times 10^{19} \frac{\dot{m}}{m r_0^2 \beta_{\rm z}} \ {\rm cm}^{-3}, \tag{7.5}$$

where $\dot{m} \equiv \dot{M}/\dot{M_{\rm Edd}}$ is the accretion rate in Eddington units, $m = M/M_\odot$ is the neutron star mass in units of solar masses, $r_0 = R_0/(R_\odot^{\rm scw} m)$ is the accretion column radius in units of the neutron star Schwarzschild radius, and $\beta_{\rm z} = V_{\rm z}/c$ is the accretion column velocity. We derived $\dot{m}$ from the best-fit value of τ reported in the tables 7.1 and7.2 for XTE J1739-302 and IGR J17544-2619, respectively, (with $r_0 = 0.25$ and $\beta_{\rm max} = 0.05$) and using equation (44) in [52] (hereafter F12) for both sources. Then, substituting $\beta_{\rm z}$ in equation (7.5) with a value averaged over the vertical z-coordinate $< \beta_{\rm z} >$, we obtain $n_{\rm e} \sim 10^{21}$ cm^{-3} in both sources.

Now, let us consider the continuity equation for the wind of the supergiant for spherical case

$$N_{\rm e}^w = 1.4 \times 10^7 \frac{\dot{M}_7}{r_{\rm au}^2 V_8^w} \ {\rm cm}^{-3}, \tag{7.6}$$

where $\dot{M}_7$ is the supergiant mass-loss rate in units of 10^{-7} solar masses for year, $r_{\rm au}$ is the distance from the supergiant centre in astronomical units, and V_8^w is the wind velocity in units of 10^8 cm s^{-1}. For the system and orbital parameter of IGR J17544-2619 ($M_{\rm SG} \sim 30 M_\odot$, $R_{\rm SG} \sim 22 R_\odot$, $\dot{M}_7 \sim 19$, ${\rm P_{orb}} \sim 4.9$ days) and using Kepler's third law, the orbital eccentricity must be $e < 4$. Assuming $e = 3$, the distance of the neutron star from the supergiant centre varies from $R \sim 0.13$ AU at the periastron, to $R \sim 0.13$ AU at the apoastron.

Assuming a terminal velocity of the wind $V_{\rm t} \sim 10^3$ km s^{-1}, the velocity profile defined in equation (3) of [115] and using equation (7.6) it is easy to shown that close to the neutron star $N_{\rm e}^w \sim 10^{10}$ cm^{-3}.

Similar results are obtained for XTE J1739-302 ($M_{\rm SG} \sim 30 M_\odot$, $R_{\rm SG} \sim 22 R_\odot$, $\dot{M}_7 \sim 24$, ${\rm P_{orb}} \sim 51$ days). This values of $N_{\rm e}^w$ are thus about 10 order of magnitude lower than those derived from the Comptonization models. Of course, this huge density contrast can be partially attenuated by the fact that the wind is not homogeneous and that accretion is mostly due to higher density clumps in the wind.

However, even denser clumps do not seem to be able to explain such high densities of the Comptonization plasma. The most likely possibility is the generation of strong shock waves due to the supersonic motion of the neutron star in the wind

during its orbital motion (bow shock region).
The Mach number of the neutron star is given by

$$\mathcal{M} \approx 10^2 V_8^{\rm ns} (\gamma Z T_{\rm e}/\mu)^{-1/2}, \tag{7.7}$$

where $V_8^{\rm ns}$ is the neutron star orbital velocity in units of 10^8 cm s^{-1}, γ is the adiabatic index, $\mu = m_{\rm i}/m_{\rm p}$, Z is the charge state and $T_{\rm e}$ is the wind temperature in eV. For wind temperatures in the range $10^5 - 10^7$ K [115], and velocities of the neutron star derived from the orbital parameters for both for XTE J1739-302 and IGR J17544-2619, $\mathcal{M}$ varies from a few to about 30. The physics of shocks in these systems is however very complicated for the intrinsic three-dimensional nature of the problem. Indeed, if from one side the supersonic motion of the neutron star ensures the formation of a bow shock, on the other hand this discontinuity occurs in a region where the magnetic field plays an important role in determining the gas configuration.
A pure dipolar magnetic field may lead to a channelling of accreting matter towards the magnetic poles of the neutron star, but if non-negligible multipole components are presents (e.g. quadrupole) then matter can also (or mainly) being accreted at the equator of the neutron star.

8

Conclusions

Radiative transfer describes the energy exchange between matter and electromagnetic radiation through absorption, emission and scattering processes, therefore it is a fundamental issue in a wide range of research fields.
In Astrophysics the radiative transfer is undoubtedly one of the most important topics to be studied, since the radiation carries out most, and often all, the information which we may receive from any kind of astrophysical objects, including the Universe itself.
Probably due to its extremely significance, the mathematical structure that describes the physics behind such phenomenon is rather complicated. The equation that properly represents radiative transfer is, indeed, integro-differential. The unknown function, i.e. the specific intensity of the radiation or, apart from a dimensional constant, the photon occupation number, depends on seven independent variables (space, direction, frequency and time). Finding complete solutions of the RTE as a function of all these variables is, de facto, an extremely arduous task, if not even impossible in most of the cases.
Unavoidable simplifications should be introduced starting, for instance, from the choice of the geometry used to describe the system under investigation. Subsequently, considerations about the physics involved may lead to further reasonable assumptions which can restrict the energy range of investigation, the number of independent variables and the number of dominant processes, as well.
In the subclass of cases where a certain set of allowed assumptions is made, analytical, but prevalently numerical, solutions of RTE can be found.
Throughout the present thesis I introduced the problem of radiative transfer in the presence of strong magnetic fields. The importance of studying RTE with the inclusion of the effects of an external magnetic field increased dramatically with the discovery of astrophysical sources which, through indirect evidences, showing huge magnetic fields ($B \gtrsim 10^{12}$ G).
Generally, RTE describing the energy transfer by electromagnetic radiation travelling across magnetised medium maintains its integro-differential nature.

In our first attempt to face such problem, we initially followed the analytic prescription suggested by Lyubarskii [8]-[9]. We assume that the stellar atmosphere can be approximated by a plane-parallel slab of non-relativistic thermal electrons. An external uniform magnetic field of the order of $\sim 10^{14}$ G with the axis aligned with the normal of the slab is assumed and the soft seed photons source is placed at the bottom. In this scenario, we assume that the dominant process which modifies the photon energy is the multiple inverse Compton scattering.
In these circumstances, the non-relativistic electrons follow circular orbits along the field lines. The transverse component of their kinetic energy is quantized in the so-called Landau levels. The quantum of energy is the cyclotron energy $E_c = 11.57 \times B_{12}$ keV.
The properties of the medium are greatly affected by the magnetic field, not least the fact that, in first approximation, it becomes birefringent, causing the formation of two modes of radiation polarisation nearly linear and orthogonal (ordinary and extraordinary), with different cross sections depending on energy and angle between the photon propagation direction and the magnetic field.
Thus the process of photon scattering off electrons has, in principle, cross sections which are resonant respect to the cyclotron energy. To avoid the treatment of resonances, we consider the photon energy range $E \ll E_c$. Under these conditions, simplified cross sections can be used, but we still should solve a system of integro-differential equations.
We decided to study only the RTE describing those photons (ordinary) which have the large cross-section for inverse Compton and, since we include the O$\rightarrow$E mode-switching term (ordinary to extraordinary), we treat also the small amount of extraordinary photons created from this process.
In order to emphasise this choice, we impose that the entire seed photon population has ordinary polarisation.
The final equation can be reduced to a system of two equations if we consider that the photons that can be efficiently Comptonized ($y_{\rm NR} \gtrsim 1$) are those travelling at large angles ($\psi > \tau^{-1}$) respect to the magnetic field axis in a large Thomson optical depth environment ($\tau \gtrsim 20$).
The system is made of an integral homogeneous Fredholm equation of the second kind, which is an eigenvalue problem providing the spatial diffusion of the photons inside the slab, and a differential equation describing the energy exchange between electrons and photons. The energy equation can be solved even analytically without making further restrictions, but the space equation is rather complicated. Lyubarskii provided an approximated treatment of such integral equation, giving good results. We confirmed and tested the Lyubarskii's analytical results and we extended them using numerical techniques. We performed a very accurate analysis of the eigenvalue problem obtaining a large set of eigenvalues and eigenfunctions. Introducing these new results as parameters into the energy equation, we solve for the first five eigenvalues of the integral space operator and we found that, as in the case of zero external field, the leading contribution to the emerging spectrum of the radiation is provided by the first Comptonization mode, related to the first eigenvalue.

Subsequently to this very specific analysis, since, even numerically, handling integro-differential equations is extremely demanding, we decided to implement an algorithm which allows to solve differential RTE.
The problem of radiative transfer is described by a partial differential equation (PDE) when the Fokker-Planck (diffusion) approximation is applicable. Performing a Taylor expansion of the photon occupation number and the electron distribution function for small energy exchange, RTE becomes a second order time-dependent inhomogeneous parabolic PDE.
If we consider the static case, RTE reduces to an inhomogeneous elliptic PDE with vanishing mixed derivatives. Such kind of equation are frequently dealt using relaxation methods. Relaxation methods are based on writing the equation by finite differences then, making an initial guess for the configuration of the unknown function and giving properly chosen boundary conditions, the configuration relaxes into the actual solution of the equation.
We tested our code considering the RTE described by Becker & Wolff [28]. We picked that equation because the authors, using the "escape time" prescription and averaging over angle and energy the magnetic Thomson cross sections, found a differential form of RTE in the case of high magnetic field ($B \sim 10^{12}$ G) for cylindrical geometry, describing an accretion column onto a magnetised neutron star. The details of the algorithm and its application are given and discussed accurately, as for what concerns the implementation of the code on the XSPEC package.
This second approach to the problem of radiative transfer is, of course, a further simplification even respect to our previous treatment of RTE in the presence of strong magnetic fields, because it approximates the solution of the integral operator for spatial photon diffusion at large angles (2.23) to the field with the coefficient $\mathcal{D}_{\perp}$, focusing instead on spatial diffusion of photons travelling along field lines. However, operating in the parameter space in which the equation proposed in [28] is valid, the results obtained by our code are comparable with those we have found in the previous part of this thesis.
The main difference consists in the fact that in the BW07 treatment, they consider angle- and energy-averaged cross sections for the two polarisation modes and related optical depths. This approximation, plus the escape term prescription which implies the substitution of the actual solution of the integral equation describing the spatial diffusion at large angles to the field with a single coefficient ($\mathcal{D}_{\perp}$), smears out all the energy and angle dependences of the photon emerging spectrum and, therefore almost all the physical information we can extrapolate from the solution of RTE.
Instead in the Lyubarskii's approach, although we are making several assumptions too, we are preserving both the dependences on energy and angle in the cross sections and part of the physics, as well. In this scenario, assuming 100% ordinary mode polarisation seed photons, indeed, the spatial diffusion is described by the solution of the integral equation (2.23) for ordinary photons travelling at large angles to the Z-axis, while the few extraordinary photons created via mode-switching escape freely from the slab.
This fundamental point has to be consider using our code and, especially when

we define the initial set of parameters, in order to operate in the parameters space when diffusion approximation holds. A step forward would be a further extension of the Lyubarskii's approach, including also the extraordinary photons, and the implementation of a dedicated code delivered to the scientific community.
As a result of the collaboration with the IASF-Palermo group, we implemented our model in the X-ray spectral fitting package XSPEC and we used it to fit the spectrum of the Supergiant Fast X-ray Transients XTE J1739-302 and IGR J17544-2619 using simultaneous observations of *Swift*/XRT and BAT instruments. We compared our model to the other models which are usually adopted to describe the X-ray spectra of these sources and we found that it provides satisfactory statistical results. The model will be also delivered to the scientific community.
Although my research is still way too far to describe in details all the complex processes that occurs in the atmospheres of strongly magnetised stars, I decided to start from the comprehension of the very basics of the physics involved with the purpose of developing numerical techniques which allow the resolution of RTE at different stages of approximation. A first step towards this goal has been made.

A

A Brief Review of Numerical Integration Methods

The most general Fredholm equation of the second kind is defined as

$$\lambda\, x(s) - \int_a^b K(s,t)\, x(t)\, dt = y(s), \quad a \le s \le b, \quad \lambda \neq 0. \tag{A.1}$$

The integral operator is usually completely continuous and the integration region is commonly a surface in $\mathbb{R}^3$. If the kernel function, $K(s,t)$, is a continuous function, it is possible to find a convergent and stable solution of equation (A.1). The numerical methods used for finding solutions of equation (A.1) are conventionally subdivided into the following main classes [39]:

- Degenerate Kernel Approximation Methods
- Projection Methods
- Nyström Methods (or Quadrature Methods)

with, in addition, their iterative variants, that I will not discuss here.
The integral equation (A.1) can be written in the more compact form $(\lambda\mathcal{I}-\mathcal{K})x = y$. Let's assume that $\mathcal{K}$ is a compact integral operator belonging to a Banach space* $\mathcal{X}$, e.g. $C[a,b]$ or $L^2(a,b)$, for the rest of this paragraph.

A.1 Degenerate Kernel Approximation Methods

A kernel $K(s,t)$ is called *degenerate* if it can be written as

$$K(s,t) = \sum_{j=1}^{n} \alpha_j(s)\beta_j(t). \tag{A.2}$$

*A Banach space is a normed linear space, $\mathcal{X}$, that is a complete metric space with respect to the metric d derived from its norm $||\cdot||$, where $d(x,y) = ||x-y||$.

In this case equation (A.1) turns into a linear system, namely

$$\lambda\, c_j - \sum_{j=1}^{n} (\alpha_j, \beta_j)\, c_j = (y, \beta_j), \quad i = 1, \ldots, n \tag{A.3}$$

with a solution of the form

$$x(s) = \frac{1}{\lambda} \left[y(s) + \sum_{j=1}^{n} c_j \alpha_j(s) \right]. \tag{A.4}$$

Although the majority of the kernels are not degenerate, in some cases it is possible to find an approximate degenerate form for them. We construct an ordered set of degenerate kernels $K_n(s,t)$, which has the following property

$$\max_{a \le s \le b} \int_a^b |K(s,t) - K_n(s,t)| dt \to 0 \ \text{ as } \ \mathrm{n} \to \infty. \tag{A.5}$$

Substituting the original kernel with the approximate $K_n(s,t)$ into equation (A.1), we find the solution x_n. Introducing the same operator notation used above, we define

$$\mathcal{K}_n z(s) = \int_a^b K_n(s,t) z(t) dt, \quad a \le s \le b, \ \ z \in \mathcal{X}. \tag{A.6}$$

The solution x_n fulfills the operator equation $(\lambda \mathcal{I} - \mathcal{K}_n) x_n = y$. Generally the Banach space $\mathcal{X}$ corresponds to $C[a,b]$ or $L^2(a,b)$. In particular, if we assume that the operator $\mathcal{K}$ belongs to $C[a,b]$, then the condition (A.5) is equivalent to $||\mathcal{K} - \mathcal{K}_n|| \to 0$ as n approach infinity. More detailed descriptions can be found in the references [75], [76], [78].

A.2 Projection Methods

The approximate solution found through *projection methods* is a selected function of a finite dimensional linear subspace $\mathcal{Z}$ of the initial $\mathcal{X}$. Let's $z \in \mathcal{Z}$ be this function and let's define the residual

$$r = (\lambda \mathcal{I} - \mathcal{K}) z - y. \tag{A.7}$$

We call x^* the particular z which makes the residual r small, following a proper criterion for the specific problem. If $\{\phi_1, \ldots, \phi_n\}$ is a complete, but not necessarily orthogonal, basis of $\mathcal{Z}$, we define

$$x^*(s) = \sum_{j=1}^{n} c_j\, \phi_j(s)\,, \tag{A.8}$$

and substituting it into the residual, we obtain

$$r(s) = \sum_{j=1}^{n} c_j \{\lambda\, \phi_j(s) - \mathcal{K}\, \phi_j(s)\} - y(s). \tag{A.9}$$

At this point, we have several kind of projection methods in order to minimize the residual and find the solution, but the principal ones are: (a) the *collocation method* consists in setting the collocation node points $\{t_1, \ldots, t_n\} \in [a, b]$, requiring that $r(t_i) = 0$ for $i = 1, \ldots, n$; (b) the *Galerkin method* or *method of moments* is based on the request that the Fourier coefficients of r with respect to the basis $\{\phi_1, \ldots, \phi_n\}$, vanish for $i = 1, \ldots, n$. Independently on the method we decide to follow to obtain the smallest residual, then we are able to define a set of projection operators $\mathcal{P}_n$ over the approximating subspaces $\mathcal{Z} = \mathcal{X}_n$, with $n \geq 1$. Using such operators, we can write equation (A.1) in a set of approximating equations

$$(\lambda\mathcal{I} - \mathcal{P}_n\mathcal{K})x_n = \mathcal{P}_n y. \tag{A.10}$$

The definition of the operation $\mathcal{P}_n x$ is slightly different depending on the specific projection method we are considering.
These methods usually impose that the following relation is satisfied

$$\mathcal{P}_n z \to z \quad \text{as} \quad \text{n} \to \infty, \quad \text{for all} \quad \text{z} \in \mathcal{X}, \tag{A.11}$$

nonetheless there exist important cases in which this is no longer valid. However the weaker, but still reasonable, condition over the projections that still holds is

$$||\mathcal{K} - \mathcal{P}_n\mathcal{K}|| \to 0 \quad \text{as} \quad \text{n} \to \infty\,, \tag{A.12}$$

which follow from (A.11) and from the compactness of the operator $\mathcal{K}$ [39].
Projection methods are probably the most widely used collection for solving integral equations ([77], [78]), even if a number of discrete projection methods recently seems to take place [79].

A.3 Nyström Methods

The Nyström methods consist in approximating the integral operator in (A.1) by numerical integration. Therefore initially we need to choose a proper approximate *quadrature rule*, i.e. a numerical integration scheme

$$\int_a^b y(s)ds \approx \sum_{j=1}^{n} w_j\, y(s_j) \tag{A.13}$$

where the set $\{w_j\}$ are the weights of the quadrature rule and the n-points $\{s_j\}$ are the abscissas [59]. These schemes are convergent as n tends to infinity for all the functions $y \in C\,[a, b]$.
The choice of the quadrature rule is arbitrary, although is preferable to use, at least, high-order quadrature rules, since the solution method involves $O(n^3)$ operations. For instance, the Gauss-Legendre quadrature rule is commonly used for smooth, nonsingular problems [80].
Once that we have decided the most appropriate quadrature rule for the specific

problem, we define

$$\begin{aligned}\mathcal{K}\, z(s) &\equiv \int_a^b K(s,t)\, z(t)\, dt \\ &\approx \sum_{j=1}^{n} w_j K(s,t_j)\, z(t_j) \equiv \mathcal{K}_n\, z(s), \qquad a \le s \le b \end{aligned} \tag{A.14}$$

for all $z \in C\,[a,b]$. Equation (A.1) becomes $(\lambda\mathcal{I} - \mathcal{K}_n)x_n = y$ or equivalently

$$\lambda\, x_i(s) - \sum_{j=1}^{n} w_j K(s,t_j)\, x(t_j) = y(s), \qquad a \le s \le b. \tag{A.15}$$

Calculating this equation at the quadrature points, we obtain a linear system

$$\lambda\, z_l - \sum_{j=1}^{n} w_j K(t_l,t_j)\, z_j = y(t_l), \qquad l = 1,\ldots,n \tag{A.16}$$

where $z_l \equiv x_i(t_l)$. To obtain the solution not only at the integration node points, we have to interpolate the solution all over the interval $[a,b]$. Nyström found that the best interpolation formula, in order to maintain the accuracy of the method, is given by the formula (A.15), slightly rearranged as follows

$$x_i(s) = \frac{1}{\lambda}\left[y(s) + \sum_{j=1}^{n} w_j K(s,t_j)\, z_j\right], \qquad a \le s \le b. \tag{A.17}$$

B

Generalized Quadrature Rules: Simpson's Rule

The standard quadrature rules such as the *trapezoidal rule* or the *Simpson's rule* are powerful tools for the numerical integration of a smooth function. In particular, when we are dealing with integral equations, the standard quadrature rules are used in the cases in which the integral operator is a compact (completely continuous) operator of a Banach space $\mathcal{X}$. Nonetheless, this domain of applicability can be extended to those operators having several continuous derivatives, although they have singularities of the kind

$$\log|s-t|, \qquad |s-t|^{\alpha} \quad \text{for} \quad \alpha > -1, \qquad \log|\cos s - \sin t|. \tag{B.1}$$

In these cases too, the integration is performed by the substitution of the integrand function $f(t)\varphi(t)$ where $\varphi(t)$ is assumed to be a Lebesgue integrable function (or, at least, the integral $\int_a^b |\varphi(t)|\,dt$ should be an ordinary singular integral defined as a limit of Riemann integrals) on the interval $[a,b]$ and $f \in \mathcal{C}[a,b]$, with an approximate sequence $\{f_n\}$, so that the integral becomes

$$\int_a^b f(t)\varphi(t)\,dt \approx \int_a^b f_n(t)\varphi(t)\,dt \tag{B.2}$$

with the error decreasing as n increases. The sequence f_n is generally chosen to be an interpolating polynomial of degree n for the function f or an nth partial sum of a series $\sum \alpha_j r_j(t)$ for f ([25] and references therein). This kind of approaches shares a common drawback. The evaluation of integrals as

$$\int_a^b r_j(t)\varphi(t)\,dt \tag{B.3}$$

becomes increasingly complex as the index n increases. The generalized quadrature rule, proposed by Atkinson and used in Chap.2, assumes, instead, f_n to be

a *piecewise* polynomial interpolating function. The error introduced with such quadrature rule is

$$E_n(f) = \int_a^b |f(t) - f_n(t)|\varphi(t)\,dt,$$
$$|E_n(f)| \leqq ||\varphi||_1 ||f - f_n||, \tag{B.4}$$

where we have defined

$$||\varphi||_1 = \int_a^b \varphi(t)\,dt. \tag{B.5}$$

This approach, in principle, can be valid for the extension of several quadrature rule, such as the trapezoidal rule, the Simpson's rule, etc.

B.1 A Generalized Simpson's Rule

For our purposes, we are interested in a generalized Simpson's rule which is based on the assumptions discussed above. Let consider then a $n \geqq 1$, a spacing between nodes being $h = (b-a)/(2n)$ and nodes defined as $t_j = a + j\,h$, with $j = 0, 1, \ldots, 2n$. We assume that f_n is a piecewise quadratic interpolating function to f on all the points t_j of the grid, with f_n being a quadratic function on each subinterval $\left[t_{2j-2}, t_{2j}\right]$ for $j = 1, \ldots, n$. The quadrature formula becomes

$$\int_a^b f_n(t)\varphi(t)\,dt = \sum_{j=1}^{n} \left[\alpha_j f(t_{2j-2}) + \beta_j f(t_{2j-1}) + \gamma_j f(t_{2j})\right] \tag{B.6}$$

where we have introduced the quantities

$$\alpha_j = \int_{t_{2j-2}}^{t_{2j}} \frac{(t - t_{2j})(t - t_{2j-1})}{2h^2}\varphi(t)\,dt$$
$$\gamma_j = \int_{t_{2j-2}}^{t_{2j}} \frac{(t - t_{2j-1})(t - t_{2j-2})}{2h^2}\varphi(t)\,dt$$
$$\beta_j = \int_{t_{2j-2}}^{t_{2j}} \frac{(t - t_{2j} - 2)(t - t_{2j})}{-h^2}\varphi(t)\,dt. \tag{B.7}$$

Defining the modulus of continuity as

$$\omega(f; h) = \max_{|s_1 - s_2| \leqq h} |f(s_1) - f(s_2)|, \tag{B.8}$$

and, consequently, the inequality

$$||f - f_n|| \leqq \frac{5}{4}\omega(f; h), \tag{B.9}$$

we find that $E_n(f) \to 0$ as $n \to \infty$, assuming that $\omega(f; h) \to 0$ as $h \to 0$. Additionally, Atkinson demonstrates that if $f''' \in \mathcal{C}\,[a, b]$, the relation

$$|E_n(f)| \leqq \frac{\sqrt{3}}{27} h^3 ||f'''||\,||\varphi||_1 \tag{B.10}$$

is valid. It is worth noticing that this relation holds for a lower order with respect to the ordinary Simpson's rule. The reason is that the interpolating function for $\left(t - t_{2j-1}\right)^2$ is odd at t_{2j-1} on the triplet $\left[t_{2j-2}, t_{2j}\right]$. If $\varphi \equiv$const, both the integral and the numerical integral of $\left(t - t_{2j-1}\right)^2$ over the triplet $\left[t_{2j-2}, t_{2j}\right]$ will vanish. Therefore the numerical integration of cubics is exact. This is no longer valid if $\varphi \neq$const. In these cases, the quadrature rule can be extended using higher degree order polynomials as f_n.

C

Steepest Descent Method

The steepest descent method is a very powerful technique that allows the integration of function which are shaped as a narrow asymmetric peak and are almost vanishing all over the rest of the interval. The method described by Titarchuk, Mastichiadis & Kylafis [43] establishes that substituting the integrand function with a Gaussian and neglecting the tail, the integral can be solved with sufficiently high accuracy. Therefore, the numerical and analytical integration of sharp functions is greatly simplified, using such method. In particular, we have used the steepest descent method in order to study the asymptotic behavior of the energy flux when we are in the non-relativistic regime $kT << m_e c^2$, i.e. if the relation $\alpha + 1 + (2/\sqrt{1+4l}) >> 1$ is satisfied in the integral

$$I(x,\alpha,l) = \int_0^\infty e^{-t}(x\sqrt{1+4l}+t)^{\alpha+1+\frac{2}{\sqrt{1+4l}}}\ t^{\alpha+1-\frac{2}{\sqrt{1+4l}}}\ dt\,. \tag{C.1}$$

In order to substitute correctly the integrand function with a Gaussian, it is convenient to define some quantities. Performing the substitution $t' = \alpha t$, we define

$$\begin{aligned} \omega^+ &= \alpha + 1 + \frac{2}{\sqrt{1+4l}} \\ \omega^- &= \alpha + 1 - \frac{2}{\sqrt{1+4l}} \end{aligned} \tag{C.2}$$

and

$$\phi(t) = \alpha\left[t - \frac{\omega^+}{\alpha}\ln(x\sqrt{1+4l}+\alpha t) - \frac{\omega^-}{\alpha}\ln(t)\right]. \tag{C.3}$$

The integral (C.1) expressed with respect to the new quantities reads as

$$I(x,\alpha,\omega^\pm) = (\alpha)^{\omega^- +1}\int_0^\infty e^{-\phi(t)}\,. \tag{C.4}$$

Following the steepest descent method, we should find the approximated form

$$I(x,\alpha,\omega) = \frac{\alpha^\alpha}{t_0}e^{-\varphi(t_0)}\left[\frac{2\pi}{\varphi(t_0)''}\right] \tag{C.5}$$

for the integral (C.4), hence we need to find the minimum of the exponent $\phi(t)$ at $t = t_0$ and its second derivative in such point. The first derivative is the following

$$\phi(t)' = \alpha \left[1 - \frac{\omega^+}{(x\sqrt{1+4l} + \alpha t)} - \frac{\omega^-}{\alpha t} \right], \tag{C.6}$$

which vanishes at the point

$$t_0 = \frac{\left(-x\sqrt{1+4l} + \omega^+ + \omega^-\right)}{2\alpha} + \sqrt{\left(x(1+4l) - \omega^+ - \omega^-\right)^2 + 4\omega^- x\sqrt{1+4l}}. \tag{C.7}$$

After some algebra, we find the second derivative of the exponent $\phi(t)$ which is

$$\phi(t)'' = \alpha \left[\frac{\omega^+ \alpha}{(x\sqrt{1+4l} + \alpha t)^2} + \frac{\omega^-}{\alpha t^2} \right]. \tag{C.8}$$

Then, substituting into (C.5), we obtain the approximated integral

$$I(x, \alpha, \omega^{\pm}) = \alpha^{(\omega^- - 1)} e^{-\phi(t_0)} \left[\frac{2\pi}{\phi(t_0)''} \right]^{\frac{1}{2}}. \tag{C.9}$$

The approximated relation (C.9) provides good results for $\alpha > 1$, while when $\alpha \leq 1$ this approximation does not hold. For $\alpha \leq 1$, we should integrate by parts the integral (C.4), obtaining

$$I(x, \alpha, \omega^{\pm}) = \frac{[I(x, \alpha + 1, y) - \omega_+ I(x, \alpha + 1, y)]}{\omega_- + 1}, \tag{C.10}$$

then, following the same procedure, we find the approximated expression for $\alpha \leq 1$, which is

$$I(x, \alpha, \omega^{\pm}) = \alpha^{\omega_- + 1} e^{-\phi(t_0)} \left[\frac{2\pi}{\phi(t_0)''} \right]^{\frac{1}{2}} \tag{C.11}$$

where

$$\begin{aligned} \phi(t_0) &= \alpha \left[t_0 - \frac{\omega^+}{\alpha} \ln(x\sqrt{1+4l} + \alpha t_0) - \frac{1}{\alpha}(\omega^-) \ln(t_0) \right] \\ \phi(t_0)'' &= \alpha \left[\frac{\omega^+ \alpha}{(x\sqrt{1+4l} + \alpha t_0)^2} + \frac{1}{\alpha t_0^2}(\omega^-) \right]. \end{aligned} \tag{C.12}$$

D

Landau Levels

Let's suppose to have a medium made of ionized hydrogen atoms subjected to the action of an external magnetic field. The physics that governs the motion of a charged particles in a magnetic field is well known and presented in many text books, such as [10], [11]. For a generic non-relativistic particle with charge e_i and mass m_i moving in an external uniform magnetic field oriented along the z-axis, the classical physics states that the particle follows circular orbits along the field lines with angular frequency $\omega_c = |e_i|B/(m_i c)$. In non-relativistic quantum mechanics, the transverse component of the kinetic energy is quantized in Landau levels, and it turns out to be

$$E_{\perp,n} = (n_L + \frac{1}{2})\hbar\omega_c\,, \qquad n_L = 0, 1, 2\ldots \tag{D.1}$$

For an electron, the quantum of energy is the cyclotron energy

$$E_c = \hbar\omega_c = \hbar\frac{eB}{m_e c} = 11.57\left(\frac{B}{10^{12}\mathrm{G}}\right)\ \mathrm{keV}. \tag{D.2}$$

Including the kinetic energy associated with the z-momentum (p_z) and the spin energy $E_{\sigma_z} = e\hbar/(2m_e c)\boldsymbol{\sigma}\cdot\mathbf{B} = \hbar\omega_c\sigma_z/2$ with ($\sigma_z = \pm 1$), the total electron energy becomes

$$E_n = n\hbar\omega_c + \frac{p_z}{2m_e}\,, \tag{D.3}$$

where $n = n_L + (1+\sigma_z)/2 = 0, 1, \ldots$. Note that the ground Landau level ($n = 0$) have spin degeneracy one, because $\sigma_z = -1$, instead all the excited levels have spin degeneracy two ($\sigma_z = \pm 1$). Besides, since the transverse energy (D.1) is independent on the position of the guiding center of the gyration, the Landau levels are degenerate by themselves.
When the external magnetic field is extremely strong such that $\hbar\omega_c \gtrsim m_e c^2$, or equivalently $B \gtrsim B_c = m_e^2 c^3/(e\hbar) = 4.414 \times 10^{13}$ G, the transverse motion of the electrons becomes relativistic. The relativistic expression correspondent to

(D.3) can be found through the solution of the Dirac equation in an homogeneous magnetic field [20], and it reads as

$$E_n = \left[c^2 p_z^2 + m_e^2 c^4 \left(1 + 2n \frac{B}{B_c} \right) \right]^{1/2} . \tag{D.4}$$

The wavefunctions, solution of the Dirac equation, should have the same shape as the classical case. By the choice of these electron wavefunctions depends both the rates and the cross-sections associated to the process in a uniform magnetic field. The correct physical choice was proposed by Sokolov & Ternov (1968) [12] and then confirmed by Graziani (1993) [13]. For further details see [23].

Bibliography

[1] Sharkov E.A., *Passive Microwave Remote Sensing of the Earth. Physical Fondations*, Chirchester, UK: Springer & Praxis Publishing, 2003.

[2] Abramovitz M., Stegun I.A., *Handbook of Mathematical Functions*, New York: Dover, 1970.

[3] Rybicki G.B., Lightman A.P., *Radiative Process in Astrophysics*, New York: John Wiley & Sons, 1979.

[4] Pomraning G.C., *The equation of Radiation Hydrodynamics*, Oxford: Pergamon Press, 1973.

[5] Collins G.W., *The Fundamentals of Stellar Astrophysics*, 2003.

[6] Mihalas D., *Stellar Atmospheres*, 2d ed. W.H. Freeman, San Francisco, 1978.

[7] Tayler R.J., *The Stars, Their Structure and Evolution*, Cambridge University Press, 1970.

[8] Lyubarskii Y., Astrofisika, **28**, 183-191, 1988.

[9] Lyubarskii Y., Astrofisika, **28**, 429-442, 1988.

[10] Landau L.D., Lifshitz E.M., *Quantum Mechanics*, New York: Pergamon Press, 1977.

[11] Mészáros P., *High-Energy Radiation From Magnetized Neutron Stars*, Chicago: University of Chicago Press, 1992.

[12] Sokolov A.A., Ternov I.M., *Synchrotron Radiation*, New York: Pergamon, 1968.

[13] Graziani C, ApJ, **412**, 351, 1993.

[14] Canuto V., Lodenquai J., Ruderman M., Phys.Rev. D, **3**, 2303, 1971.

[15] Ventura J., Phyis. Rev. D, **19**, 1684, 1979.

[16] Herold H., Phys. Rev. D, **19**, 2868, 1979.

[17] Melrose D.B., Parle A.J., Australian J. Phys., **36**, 755, 1983a.

[18] Daugherty J.K., Harding A.K., ApJ, **309**, 362, 1986.

[19] Harding A.K., Daugherty J.K., ApJ, **374**, 687, 1991.

[20] Johnson M.H., Lippmann B.A., *Phys. Rev.*, **76**, 828, 1949.

[21] Bonazzola S., Heyvaerts J., Puget J., A&A, **78**, 53, 1979.

[22] Heitler W., *The Quantum Theory of Radiation*, Oxford Clarendom Press, 1954.

[23] Harding A.K., Lai D., arXiv:astro-ph/0606674v2.

[24] Bleistein N., Handelsman R.A., *Asymptotic Expansions of Integrals*. Dover, 1986.

[25] Atkinson K.E., SIAM J. Numer. Anal., Vol.4, No.3, 1967.

[26] Trümper J., Pietsch W., Reppin C., Voges W., et al., ApJ, **219**, L105, 1978.

[27] Mereghetti S., A&A Review, 2008.

[28] Becker P.A., Wolff M.T., ApJ, 654, 435, 2007.

[29] Israel G.L., et al., ApJ, 685, 1114, 2008.

[30] Lyubarskii Y.E., Sunyaev R.A., Sov. Astron. Lett., 8(5), 1982.

[31] Atkinson K.E., Shampine L.F., ACM *Trans. Math. Software*, **34** (2008), article #21.

[32] Werner A.S., *The Analyst*, *Annals of Mathematics*, Vol.10, No.5, 137-139, (1883).

[33] Morse P.M., Feshbach, H., *Methods of Theoretical Physics*, McGraw-Hill Book Company, Inc., 1953.

[34] Baker C., *The Numerical Treatment of Integral Equations*, Oxford Univ. Press, 1977.

[35] Golberg M.A., *Numerical Solution of Integral Equations*, Plenum Press: New York, 1990.

[36] Hackbusch W., *Integral Equations: theory and Numerical Treatment*, Birkhäuser Verlag, Basel, 1995.

[37] Kress R., *Linear Integral Equations*, 2nd Edition, Springer-Verlag, 1999.

[38] Polyanin A.D., Manzhirov A.V., *Handbook of Integral Equations, 2nd Edition*, Chapman & Hall/CRC, 2008.

[39] Bultheel A., Cools R., *The Birth of Numerical Analysis*, World Scientific Publishing Co Pte Ltd, 2009.

[40] Carothers N.L., *A Short Course on Banach Space Theory*, Cambridge University Press, 2004.

[41] Nobili L., Turolla R., Zane S., MNRAS, 386, 1527-1542, 2008.

[42] Titarchuk L., ApJ, 434, 570, 1994.

[43] Titarchuk L., Mastichiadis A., Kylafis N., ApJ, 487, 834-846, 1997.

[44] Rea N., Zane S., Turolla R., Lyutikov M., Götz D., ApJ, 686, 1245-1260, 2008.

[45] Lyutikov M., Gavriil F.P., MNRAS, 368, 690, 2006.

[46] Rea N., Zane S., Lyutikov M., Turolla R., Ap&SS, 308, 61, 2007a.

[47] Rea N., Turolla R., Zane S., Tramacere A., Stella L., Israel G.L., Campana R., ApJ, 661, L65, 2007b.

[48] Basko M.M., Sunyaev R., A&A, 42, 311-321, 1975.

[49] Blanford R.D, Payne D.G., MNRAS, 194, 1041-1055, 1981.

[50] Blanford R.D, Payne D.G., MNRAS, 194, 1033-1039, 1981.

[51] Kompaneets A.S., Soviet Phys., JETP Letters, 4, 730. 1957.

[52] Farinelli R., Ceccobello C., Romano P., Titarchuk L., A&A, **538**, A67, 2012.

[53] Farinelli R., Titarchuk L., A&A, **525**, A102, 2011.

[54] Titarchuk L. Fiorito R., ApJ, **612**, 988, 2004.

[55] Farinelli R., Titarchuk L., Paizis A., Frontera F., ApJ, 680, 602-614, 2008.

[56] Ferrigno C., Becker P.A., Segreto A., Mineo T., Santangelo A., A&A, 498, 825-836, 2009.

[57] Lyubarskii Y.E., Sunyaev R.A., Soviet Astronomy Letter, 8, 330, 1982.

[58] Payne D.G., Blanford R.D., MNRAS, 196, 781-795, 1981.

[59] Press W.H., Teukolsky S.A., Vetterling W.T., Flannery B.P., *Numerical Recipes in C. The Art of Scientific Computing*, Cambridge: University Press, 2nd ed., 1992.

[60] Katz J.I., ApJ, **206**, 910, 1976.

[61] Becker P.A., MNRAS, **343**, 215-240, 2003.

[62] Becker P.A., ApJ, **498**, 790, 1998.

[63] Becker P.A., Wolff M.T., ApJ, **630**, 465, 2005.

[64] Colpi M., ApJ, **326**:223-234, 1988.

[65] Riffert H., ApJ, **327**:760-771, 1988.

[66] Sunyaev R., Titarchuk L., A&A, 86, 121-138, 1980.

[67] Titarchuk L., Lyubarskii Y., ApJ, 450, 876, 1995.

[68] Mastichiadis A., Kylafis N.D., ApJ, 384, 136-142, 1992.

[69] Shu F., *The Physics of Astrophysics I, Radiation*, Mill Valley (CA): University Science Books, 1991.

[70] Shu F., *The Physics of Astrophysics II, Gas Dynamics*, Mill Valley (CA): University Science Books, 1992.

[71] Shapiro S.L., Teukolsky S.A., *Black Holes, White Dwarfs, and Neutron Stars*, New York: John Wiley & Sons, 1983.

[72] Frank J., King A., Raine D., *Accretion Power in Astrophysics*, Cambridge: University Press, 3rd Edition.

[73] Peraiah A., *An Introduction to Radiative Transfer*, Cambridge: University Press, 2004.

[74] Titarchuk L., Zannias T., ApJ, 493, 863, 1998.

[75] Sloan I.H., Burn B.J., Datyner N., *J. Computational Physics*, **18**, 92-105, 1975.

[76] Sloan I.H., *J. Austral. Math.Soc.*, **19** (Series B), 422-431, 1976.

[77] Chatelin F., Lebbar R, *J. Austral. Math.Soc.*, **22** (Series B), 439-451, 1981.

[78] Atkinson K.E., *The Numerical Solution of Integral Equations of the Second Kind*, Cambridge University Press, 1997.

[79] Chen C.S., Goldberg M.A., *Discrete Projection Methods for Integral Equations*, Computational Mechanics Publications, 1996.

[80] Delves L.M., Mohamed J.L., *Computational Methods for Integral Equations*, Cambridge University Press, 1985.

[81] Laurent P., Titarchuk L., ApJ, 511, 289, 1999.

[82] Zannias T., Borozdin K., Revnivtsev M., Trudolyubov S., Shrader C.R.,& Titarchuk L., ApJ, 517, 367, 1999.

[83] Shrader C.R., Titarchuk L., ApJ 521, L21, 1999.

[84] Ribó M., Negueruela I., Blay P., et al., A&A, **449**,687, 2006.

[85] Fritz S., Kreykenbohm I., Wilms J., et al., A&A, **458**, 885, 2006.

[86] Laurent P., Paul J., Denis M., et al., A&A, **300**, 399, 1995.

[87] Krivonos R., Produit N., Kreykenbohm I., et al., Atel, 211, 2003.

[88] Sguera V., Barlow E.J., Bird A.J., et al., A&A, **444**, 221, 2005.

[89] Negueruela I., Smith D.M., Harrison T.E., Torrejón J. M., ApJ, **638**, 982, 2006.

[90] Smith D.M., Heindl W.A., Markwardt C.A., et al., ApJ, **638**, 974, 2006.

[91] in't Zand J.J.M., A&A, **441**, L1, 2005.

[92] Leyder J.-C., Walter R., Lazos M., Masetti N., Produit N., A&A, **465**, L35, 2007.

[93] Leahy D.A., A&A, **391**, 219, 2002.

[94] Blay P., et al., A&A, **489**, 669-676, 2008.

[95] Drave S.P., Clarck D.J., Bird A.J., McBride V.A., Scaringi S., Dean A.J., MNRAS, p. 1257, 2010.

[96] Sidoli L., Paizis A., Mereghetti S., A&A, **450**, L9, 2006.

[97] Walter R., Zurita Heras J., Bassani L., et al., A&A, **453**, 133, 2006.

[98] Bamba A., Yokogawa J., Ueno M., Koyama K., Yamauchi S., PASJ, **53**, 1179, 2001.

[99] Lutovinov A., Revnivstev M., Gilfanov M., et al., A&A, **444**, 821, 2005.

[100] Swank J.H., Smith D.M., Markwardt C.B., ATel, 999, I, 2007.

[101] Sguera V., Hill A.B., Bird A.J., et al., A&A, **467**, 249, 2007.

[102] White N.E., Swank J.H., Holt S.S., ApJ, **270**, 711, 1983.

[103] Masetti N., Dal Fiume D., Cusumano G., et al., A&A, **382**, 104, 2002.

[104] Blay P., Ribó M., Negueruela I., et al., A&A, **438**, 963, 2005.

[105] Finley J.P., Taylor M., Belloni T., ApJ, **429**, 356, 1994.

[106] Corbet R.H.D., Sokoloski J.L., Mukai K., et al., ApJ, **675**, 1424, 2008.

[107] Titarchuk L., Cui W., Wood K., ApJ, **576**, 49, 2002.

[108] Sidoli L., Romano P., Mereghetti S., Paizis A., Vercellone S., Mangano V., Götz D., A&A, **476**, 1307, 2007.

[109] Grebenev S.A., Sunyaev R.A., Astronomy Letters, **33**, 149, 2007.

[110] Bozzo E., Falanga M., Stella L., ApJ, **683**, 1031, 2008.

[111] Coburn W., Heindl W.A., Rotschild R.E., et al., ApJ, **580**, 394, 2002.

[112] Oskinova L.M., Hamann W.-R., Feldmeier A., A&A, **476**, 1331, 2007.

[113] Walter N.E., Kallman T.R., Swank J.H., ApJ, **269**, 264, 2007.

[114] Negueruela I., Torrejón J.M., Reig P., Ribó M., Smith D.M., AIPC, **1010**, 252, 2008.

[115] Ducci L., Sidoli L., Mereghetti S., Paizis A., Romano P., MNRAS, **398**, 2152, 2009.

[116] Smith D.M., Main D., Marshall F., et al., ApJ, **501**, L181, 1998.

[117] Rahoui F., Chaty S., Lagage P.-O., Pantin E., arXiv:0802.1770, 2008.

[118] Lutovinov A., Revnistev M., Molkov S., et al., A&A, **430**, 997, 2005.

[119] Romano P., et al., The Astronomer's Telegram, 1466, 2008a.

[120] Chenevez J., et al., The Astronomer's Telegram, 1471, 1, 2008.

[121] Wang Y.-M., Frank J., A&A, **93**, 255, 1981.

[122] Gehrels N., et al., ApJ, **611**, 1005, 2004.

[123] Sunyaev R.A., Grebenev S.A., Lutovinov A.A., Rodriguez J., Mereghetti S., Götz D., Courvoisier T., The Astronomer's Telegram, 190, 2003.

[124] Grebenev S.A., Lutovinov A.A., Sunyaev R.A., The Astronomer's Telegram, 192, 2003.

[125] Walter R., Zurita Heras J., A&A, **476**, 335.

[126] Grebenev S.A., Rodriguez J., Westergaard N.J., Sunyaev R.A., Oosterbroek T., The Astronomer's Telegram, 252, 204.

[127] Kuulkers E., Oneca D.R., Brandt S., et al., The Astronomer's Telegram, 1266, 2007.

[128] in't Zand J., Heise J., Ubertini P., Bazzano A., Markwardt C., in V. Shoenfelder, G. Lichti, & Winkler ed., 5th INTEGRAL Workshop on the INTEGRAL Universe Vol. 552 of ESA Special Publication, A BeppoSAX-WFC Viewpoint of New INTEGRAL Sources, Particularly IGR J17544-2619. p. 427, 2004.

[129] Krimm H.A., Barthelmy S.D., Barbier L., et al., The Astronomer's Telegram, 1265, 2007.

[130] Sidoli L., Romano P., Ducci L., et al., MNRAS, **397**, 1528, 2009a.

[131] Sidoli L., Romano P., Mangano V., et al., ApJ, **690**, 120, 2009b.

[132] Romano P., La Parola V., Vercellone S., at al., MNRAS, **410**, 1825, 2011c.

[133] Romano P., Mangano V., Cusumano G., et al., MNRAS, **412**, L30, 2011d.

[134] Romano P., Barthelmy S.D., Esposito P., et al., The Astronomer's Telegram, 3235, 2011a.

[135] Barthelmy S.D., Barbier L.M., Cummings J.R., et al., Space Science Reviews, **120**, 143, 2005.

[136] Burrows D.N., Hill J.E., Nousek J.A., et al., Space Science Reviews, **120**, 165, 2005.

[137] Romano P., Sidoli L., Cusumano G., et al., MNRAS, **399**, 2021, 2009.

[138] Sidoli L., Romano P., Mangano V., et al., ApJ, **687**, 1230.

[139] Krimm H.A., Barthelmy S.D., Cummings, J.R., et al., in AAS/High Energy Astrophysics Division, Vol. 10, AAS/High Energy Astrophysics Division, #07.01, 2008.

[140] Rampy R.A., Smith D.M., Negueruela I., ApJ, **707**, 243, 2009.

[141] Clark D.J., Hill A.B., Bird A.J., McBride V.A., Scaringi S., Dean A.J., MNRAS, **399**, L113, 2009.

[142] Pellizza L.J., Chaty S., Negueruela I., A&A, **455**, 653, 2006.

[143] Rahoui F., Chaty S., Lagage P.-O., Pantin E., A&A, **484**, 801, 2008.